ABSTRACT

Title of dissertation: POTENTIAL ENERGY SURFACES AND REACTION DYNAMICS STUDIES OF SMALL TRIATOMIC SYSTEMS: O + H_2, OH + H and OH + D

Sule Atahan, Doctor of Philosophy, 2006

Dissertation directed by: Professor Millard H. Alexander
Department of Chemistry and Biochemistry

This dissertation is focused on the interaction of open-shell atoms and molecules. We have studied the systems in the title by means of electronic structure and statistical reaction dynamics methods.

We present an *ab initio* study of the O(^3P) + H_2 system. In particular, we have calculated potential energy surfaces for the van der Waals region of the interaction and derived and calculated the spin-orbit coupling matrix in the diabatic representation.

The rest of the dissertation is comprised of statistical, coupled-states dynamics studies. Cross sections are calculated by the coupled-states (CS) statistical method including the full open-shell character of the systems. All electronic and spin-orbit couplings are included.

We report state-to-state and overall thermal rate constants for the isotope exchange

$$\mathrm{D}(^2S) + \mathrm{OH}(^2\Pi) \rightarrow \mathrm{OD}(^2\Pi) + \mathrm{H}(^2S)$$

for 0 K< T <500 K. We predict a reaction rate constant of 14.22×10^{-11} cm^3 molecule^{-1} s^{-1} at $T = 100$ K and 10.78×10^{-11} cm^3 molecule^{-1} s^{-1} at $T = 300$ K. At lower temperatures, ($T \simeq 50$ K), the value rises to $k(T) = 15 \times 10^{-11}$ cm^{3}molecule^{-1}s^{-1}. A negative temperature dependence in the rate constant is observed. The state-resolved cross sections and rate-constants predict a significant propensity toward formation of the OD $\Pi(A')$ Λ-doublet level and the ground spin-orbit manifold, F_1.

This dissertation is also concerned with the study of vibrational and rotational relaxation of OH($^2\Pi$) by collision with H atoms. Four potential energy surfaces (PESs) ($^{1,3}A'$ and $^{1,3}A''$) describe the interaction of OH($X^2\Pi$) with H atoms. Of these, three are repulsive, while one ($^1A'$) correlates with the deep H_2O well. Consequently, rotationally- and ro-vibrationally-inelastic scattering of OH in collisions with H can occur by scattering on the repulsive PESs, in a manner similar to the inelastic scattering of OH by noble gas atoms, or by collisions which enter the H_2O well and then re-emerge. We report state-to-state cross sections and thermal rate constants for the collisions. At 300 K, we predict large ($\approx 1 \times 10^{-10}$ cm^3 molecule^{-1} s^{-1}) vibrational relaxation rates out of both v=2 and v=1, comparable to earlier experimental observations.

This surprisingly fast relaxation results from capture into the H_2O complex. There also exists a significant propensity toward formation of OH in the $\Pi(A')$ Λ-doublet level. We also report state-resolved cross sections and rate constants for rotational excitation within the OH v=0 manifold. Collisional excitation from the F_1 to the F_2 spin-orbit manifold leads to an inverted Λ-doublet population.

POTENTIAL ENERGY SURFACES AND REACTION DYNAMICS STUDIES OF SMALL TRIATOMIC SYSTEMS: $O+H_2$, OH + H and OH + D

by

Sule Atahan

Dissertation submitted to the Faculty of the Graduate School of the
University of Maryland, College Park in partial fulfillment
of the requirements for the degree of
Doctor of Philosophy
2006

Advisory Commmittee:

Professor Millard H. Alexander, Chair/Advisor
Professor Paul J. Dagdigian
Professor Andrew Harris
Professor Janice Reutt-Robey
Professor John A. Tossel

TABLE OF CONTENTS

List of Tables v

List of Figures vi

1 Introduction 1

1.1 The Potential Energy Surfaces, (PESs) 4

1.2 Molecular Energy Transfer 8

1.2.1 Vibrational Energy Transfer 9

1.2.2 Rovibrational Energy Transfer 12

2 An *Ab initio* Investigation of the $O(^3P) + H_2(^1\Sigma_g^+)$ System 15

2.1 Introduction 15

2.1.1 Previous Work on the Potential Energy Surfaces of $O(^3P) + H_2$ 16

2.1.2 Spin-Orbit Coupling 18

2.2 The Energetics and the Orbital Occupancies in the $O(^3P) + H_2$ System 20

2.3 Weakly Bound $O(^3P)-H_2$ Complex 22

2.3.1 Coupled Cluster Calculations 23

2.3.2 MRCI Calculations for C_{2v} and $C_{\infty v}$ Geometries 27

2.4 Spin-Orbit Coupling 35

2.4.1 Diabatic Representation 35

2.4.2 Method 39

2.4.3 Computational Details 40

2.5 Results 42

2.6 Summary 46

3 Introduction to Scattering Dynamics in the Presence of Long-lived Reaction Complexes 47

3.1 Introduction 47

3.2 Coupled-Channel Statistical Theory 49

3.2.1 *Ab Initio* Potential Energy Surfaces (PESs) 52

3.2.2 Hamiltonian and Basis 55

4 Cross Sections and Thermal Rate Constants for the Isotope Exchange Reaction: $D(^2S) + OH(^2\Pi) \rightarrow OD(^2\Pi) + H(^2S)$ 62

4.1 Introduction 62

4.2 Theory and Computational Methods 65

4.2.1 Coordinate Shift 66

4.2.2 Hamiltonian and Basis 67

4.2.3 Scattering Calculations 69

4.3 Results and Discussion 72

4.3.1 Cross Sections 72

4.3.2 Product State Populations 78

4.3.3 Rate Constants 82

4.4 Summary 85

5 Coupled-States Statistical Investigation of Vibrational and Rotational Relaxation of $OH(^2\Pi)$ by Collisions with Atomic Hydrogen 89

5.1 Introduction 89

5.2 Theory and Computational Methods 96

5.2.1 Hamiltonian and Basis 97

5.2.2 Scattering Calculations 100

5.3 Results and Discussion 103

5.3.1 Comparison of Multi-PES and Single-PES Calculations 103

5.3.2 Direct as compared to Complex-Mediated relaxation 104

5.3.3 Initial state selected relaxation cross sections 109

5.3.4 Final State Populations 113

5.3.5 Vibrational Relaxation Rate Constants 115

5.3.6 Rotational Excitation and Λ-doublet Inversion 118

5.4 Summary 124

6 Conclusions 127

A $O+H_2$ Entrance Channel Data 134

A.1 RCCSD(T) Data 134

A.2 Spin-Orbit Coupling Data 136

B The Theory of the Free OH/OD Diatomic Molecule 137

LIST OF TABLES

2.1 Van der Waals well depth and position of $O(^3P)-H_2$ complex in various earlier work and present RCCSD(T) calculations with aug-cc-pVQZ basis with additional midbond functions. 27

2.2 Van der Waals well depth (cm^{-1}) of the $O(^3P)-H_2$ complex obtained by MRCI+Q and RCCSD(T) methods for various states and geometries. 31

2.3 Effect of active space and the size of the basis set on the spin-orbit constant (cm^{-1}) for $O(^3P)$ 41

2.4 Spin-orbit term A (cm^{-1}) as a function of Jacobi angle θ^o and R for a fixed value of $r = 1.402$ a.u. 42

4.1 Summary of reported rate constants for D+OH reaction. 64

4.2 Values of the parameters used in the D+OH calculations. 72

5.1 Summary of calculated and measured rate constants for the vibrational relaxation of $OH(v = 1, 2)$. 92

5.2 Values of the parameters used in the OH+H calculations 102

A.1 RCCSD(T) interaction energies for the $O(^3P)-H_2$ system as a function of the Jacobi coordinate R ($\theta = 0^o$ and $r = 1.402$ a.u.). 134

A.2 RCCSD(T) interaction energies for the $O(^3P)-H_2$ system as a function of the Jacobi coordinate R ($\theta = 90^o$ and $r = 1.402$ a.u.). 135

A.3 Spin-orbit coupling terms A and B as a function of the Jacobi coordinate R for $\theta = 0^o$ and $r = 1.402$ a.u. 136

A.4 Spin-orbit coupling terms A and B as a function of the Jacobi coordinate r for $\theta = 0.0^o$ and $r = 3.0$ a.u. 137

B.1 Pertinent spectroscopic constants (cm^{-1}) for OH and OD. 146

LIST OF FIGURES

1.1 Illustration of Jacobi coordinates. 5
1.2 Collision between an atom and a collinear diatomic molecule. 10
1.3 Collision between an atom and a rotating diatomic molecule. 12

2.1 Schematic plot of the energy diagram of the $O(^3P,^1D)+H_2$ reaction for the collinear arrangement. 19
2.2 Schematic correlation diagram for the $O-p$ orbitals in collinear geometry. The degeneracy of the $^3\Pi$ state will be lifted in bent geometries. (Note that only one lobe of the each p orbital is drawn for clarity.) . 21
2.3 Van der Waals well depth for various PESs in (a) $C_{\infty v}$ and (b) C_{2v} geometries calculated by the RCCSD(T) method as a function of the size of the aug-cc-pVnZ basis. The basis also includes midbond functions as explained in the text. The H_2 bond distance is fixed at $r = 1.402$ a.u. 25
2.4 PESs in (a) $C_{\infty v}$ and (b) C_{2v} geometries calculated with RCCSD(T) method with an aug-cc-pVQZ basis with additional midbond functions for fixed values of $\theta = 0^\circ, 90^\circ$ and $r = 1.402$ a.u. 26
2.5 The comparison of the PESs in (a) $C_{\infty v}$ and (b) C_{2v} geometries calculated with RCCSD(T) method with an aug-cc-pVQZ basis with additional midbond functions for fixed values of $\theta = 0^\circ, 90^\circ$ and $r = 1.402$ a.u. (straight lines) with the MRCI+Q results extrapolated to the CBS limit (dashed-lines) 30
2.6 (R, r)-dependence of interaction energies in $^3\Pi$ (a) and in $^3\Sigma$ (b) symmetries. Note that the interaction energy, $V(R, r, \theta)$, does not include the diatomic H_2 potential. ($\theta = 0^o$, Energies in cm^{-1}) 33
2.7 (R, r)-dependence of energies in $^3B_1$ (a) and in $^3B_2$ (b) symmetries. ($\theta = 90^o$, Energies in cm^{-1}) 34
2.8 (R, r)-dependence of energies in $^3A_2$ symmetry. ($\theta = 90^o$, Energies in cm^{-1}) 35

2.9 Spin-orbit coupling terms in the entrance channel of the O+H_2 reaction. 43
2.10 Spin-orbit coupling terms in the entrance channel of the O+H_2 reaction as a function of Jacobi coordinates R and r. The unfilled and filled circles indicate the data points for terms A and B, respectively. 45

3.1 Illustration of a complex-forming reaction described by the statistical model [104]. The complex region (shaded) is delimited by a capture radius, R_c. The capture probabilities for both the reactant and products are obtained by solving coupled scattering equations outside of this capture radius. 51
3.2 Schematic illustration of the OH + H potential energy surfaces. . . . 53
3.3 Contour plots (cm^{-1}) of the OH-H PESs as a function of Jacobi coordinates R and θ for a fixed OH distance of 1.8324 a.u. 54
3.4 Positions of the lower spin-rotation levels of OH($X^2\Pi$). For clarity, the magnitude of the Λ-doublet splitting has been greatly exaggerated. 56

4.1 Schematic illustration of the reaction path for D(^2S) + OH($^2\Pi$) $\rightarrow$ $HDO^{\dagger}$ $\rightarrow$ OD($^2\Pi$) + H(^2S). The zero of energy corresponds to D+OH ($r = r_e$) and is identical for the OD+H arrangement. The vibrational zero-point energies of the diatomic fragment in each arrangement are also indicated. 63
4.2 The effect on the H+OD Jacobi coordinates of the shift in the center-of-mass due to isotope exchange. 66
4.3 Positions of the lower spin-rotation levels of OD($X^2\Pi$). 69
4.4 Total cross section as a function of the collision energy for D+OH($j = 3/2, F_1$) $\rightarrow$ OD+H. 73
4.5 Initial state-specific integral cross-sections for reactions of the OH reactant in various rotational levels of the (a) $j = 3/2 - 17/2$ in the F_1 and (b) $j = 1/2 - 15/2$ in the F_2 spin-orbit manifolds. Only the lowest and the highest rotational state of OH are labeled for clarity. 75

4.6 Total inelastic scattering cross section for OH($F_2, j = 1/2$) +D on the two repulsive triplet potential energy surfaces, $^3A'$ and $^3A''$. The inelastic scattering calculations were carried out for each potential energy surface separately. The resulting cross sections were then added. 76

4.7 Comparison of rotationally averaged D+OH → OD+H cross sections [Eq. (4.13)] from the present statistical-close-coupled calculations with the predictions of the QCT calculations of Ref. [115]. . . . 77

4.8 Cross sections for production of the energetically accessible OD rotational fine structure levels in the reaction D + OH ($j = 3/2, F_1$) → OD (j', F_i, ϵ) + H at a collision energy of 6.7 K. 79

4.9 OD rotational populations for each Λ-doublet separately in both the F_1 (upper panels) and F_2 (lower panels) spin-orbit manifolds for the reaction D+OH(j, F_1)→OD(j', F_i', ϵ')+H for initial rotational levels $j = 3/2 - 9/2$ at a collision energy of 6.7 K. 81

4.10 The temperature dependence of the rate constant for D + OH ($j = 3/2 - 17/2$, F_1)→ OD+H. The rate constants decrease for an increasing degree of rotational excitation of the OH reactant. 83

4.11 The temperature dependence of the rate constant for OH ($j = 1/2 - 15/2, F_2$) + D→ OD+H. 84

4.12 Thermally averaged rate constant for the isotope exchange reaction D+OH → OD+H (solid curve). The experimental fit indicated by the dashed curve is taken from Ref. [114] [see Eq. (4.20)]. The extended error bars designate the precision of this empirical fit. The open circles and open squares represent data obtained using H_2O or HNO_3, respectively, as the OH precursor. The "X" designates the experimental rate constant from Ref. [116]. The filled data points represent the earlier theoretical predictions, circles from Ref. [114] and squares from Ref. [115]. 86

5.1 Schematic diagram of the lowest two rotational levels in the lower F_1 ($^2\Pi_{3/2}$) spin-orbit manifold of OH. The levels are labeled with the total angular momentum exclusive of the nuclear spin, j, the e/f symmetry (Λ-doublet) labels (Refs. [154] and [108]), the total angular momentum including the nuclear spin, F, and the parity π. This figure is adapted from Fig. 1 of Ref. [155]. The Λ-doublet and hyperfine splittings are greatly exaggerated for clarity. The four OH maser transitions at 1612, 1665, 1667 and 1720 MHz are shown by the dashed vertical lines. 93

5.2 Schematic illustration of the OH + H′ ↔ OH′+H potential energy surfaces. The O(^1D)+H_2 arrangement (not shown) lies 1.89 eV higher than the OH+H asymptotes. 95

5.3 Positions of the lower spin-rotation levels of OH($X^2\Pi$). For clarity, the magnitude of the Λ-doublet splitting has been greatly exaggerated in the figure. 100

5.4 Comparison of the relaxation total cross sections with multi and single PESs for $v = 1$ level. The cross sections from the single and multi PES are compared according to the Eq.(5.17) and Eq.(5.18) 105

5.5 Comparison of the relaxation total cross sections with multi and single PESs for $v = 2$ level (panel a: $v = 2 \rightarrow 0$ and panel b: $v = 2 \rightarrow 1$). The cross sections from the single and multi PES are compared according to the Eq.(5.17) and Eq.(5.18) 106

5.6 Direct and complex-mediated contributions to the initially-state-selected total vibrational relaxation cross section for OH($v = 1, F_1, j = 3/2$) + H → OH($v = 0$) + H vibrational relaxation. The inset panel is a semilog plot to demonstrate the negligibly small size of the cross section for direct relaxation. 107

5.7 The relative percentage contribution of direct scattering to the vibrational relaxation cross sections as a function of collision energy for the lowest rotational levels of OH (panel *a*: $j = 3/2$, F_1 and panel *b*: $j = 1/2$, F_2.) 108

5.8 Initial rotational and spin-orbit resolved cross sections for OH ($v = 1, F_1/F_2, j$) + H $\rightarrow$ OH ($v = 0$) + H. Cross sections are calculated as described in Eq. 5.16. 110

5.9 Initial state selected relaxation total cross sections for OH($v, F_1, j = 3/2$) + H $\rightarrow$ OH(v')+H, for $v = 2 \rightarrow 1$, $2 \rightarrow 0$, and $1 \rightarrow 0$. 111

5.10 Comparison of the state-to-state cross sections for OH($v, F_1, j = 3/2$) + H $\rightarrow$ OH(v', F_1, j')+H for a collision energy of 580.3 cm^{-1}. 112

5.11 State-to-state OH($v, F_1, j = 3/2$)+H$\rightarrow$OH($v', F_i', j', \varepsilon'$)+H cross sections at a collision energy of 12 cm^{-1}. As in Fig. 5.10 the open cirles, filled squares, and open squares designate, respectively $v = 1 \rightarrow 0$, $v = 2 \rightarrow 0$ and $v = 2 \rightarrow 1$ processes. 113

5.12 State-to-state OH($v, F_1, j = 3/2$)+H$\rightarrow$OH($v', F_i', j', \varepsilon'$)+H cross sections at a collision energy of 1520.3 cm^{-1}. As in Fig. 5.10 the open cirles, filled squares, and open squares designate, respectively $v = 1 \rightarrow 0$, $v = 2 \rightarrow 0$ and $v = 2 \rightarrow 1$ processes. 114

5.13 Comparison of thermally averaged vibrational removal rate constants for OH($v = 1, 2$)+H. The experimental $v = 1$ room temperature value is from Reference [55]. The filled circle and filled square designate rate constants derived from experiments in which H_2O was excited, respectively, to the $|13>$ or $|12>$ vibrational level before photolysis. 116

5.14 State-to-state thermal rate constant for the transition between the two Λ-doublet levels of the ground rotational level (j=3/2, F_1). . . . 119

5.15 State-to-state direct, complex-mediated and total rate constants for the OH($j = 3/2, F_1, \varepsilon$)+H$\rightarrow$OH($j' = 5/2, F_1, \varepsilon'$) transition within the $v = 0$ manifold. The heavy solid curves depict the results of Shapiro and Kaplan (Ref. [161]). 121

5.16 Initial e/f-averaged rate constants for transitions out of the OH($v = 0, F_1, j = 3/2$) level into both Λ-doublet levels for $j' = 5/2, F_1$, $j' = 1/2, F_2$ and $j' = 3/2, F_2$. 123

B.1 Relationships between the molecule-fixed (xyz) and space-fixed (XYZ) axis systems. 138

B.2 Positions of the lower spin-rotation levels of OH($X^2\Pi$). For clarity, the magnitude of the Λ-doublet splitting has been greatly exaggerated in the figure. 144

B.3 Coupling coefficients a_j and b_j as a function of total angular quantum number j. 145

Chapter 1

Introduction

Chemical reactions occur everywhere. However, most of them are very complex involving the interactions of hundreds of particles. Gas phase reactions are relatively isolated. Consequently, one can exclude the interactions with the environment to a good approximation to focus exclusively on the interactions between just two reactants.

The study of chemical reaction dynamics is concerned with obtaining a detailed picture of the chemical and physical changes which occur during a reaction at the most fundamental level. Independent of all practical importance, the *purist* wants to discover what really happens to the atoms in regions of close approach. In this regard, molecular reaction dynamics lies at the heart of chemistry [1]. For the *pragmatist*, phenomena such as chemical lasers or combustion can be truly understood only with the knowledge of how reactivity depends on the degree of excitation of the reactants. Interstellar chemistry, also, cannot be explained by equilibrium arguments, since at very low densities thermal equilibrium is rarely obtained.

The only purely exact way to predict the dynamical behavior of atoms and electrons in chemistry is to solve the Schrödinger equation for the system in question. This is achieved in a two step process, invoking the Born-Oppenheimer Approximation (BOA). In a first step, one determines the electronic wave function to obtain the

interaction energies for a fixed nuclear geometry. Subsequently, one solves the scattering equations for nuclear motion over a single Potential Energy Surface (PES). For most systems the BOA gives satisfactory results. However, when the BOA fails, it is necessary to go beyond approximation of a single PES approach to include multiple PESs and couplings among them.

In this thesis we focus on several small triatomic systems, namely, $O(^3P)$ + H_2, $OH(^2\Pi)$ + $D(^2S)$ and $OH(^2\Pi)$ + $H(^2S)$. In these systems the BOA would be inadequate, since these interactions in principle involves several PESs which are degenerate asymptotically. This is typical of interactions involving open-shell atom and molecules, in which there is more than one way to distribute the electrons among the available molecular orbitals.

The interaction of atomic oxygen in the ground state with atomic hydrogen has been studied extensively [2–6, 6–30]. However, except for a few studies [2, 25, 31–33], in most cases the spin-orbit interaction was neglected. Although the magnitudes of spin-orbit coupling in light atoms are small, it has recently been shown that these couplings can play a significant role in the dynamics [33]. The work presented in Chapter 2 is concerned with an accurate description of the van der Waals region of the three PESs for $O(^3P)$ + H_2 in the entrance channel and the calculation of the spin-orbit terms which couple these surfaces.

The second and a more sizable part of the thesis (Chapters 3-5) involves the application of statistical capture methods for two reactions: OH + D $\rightarrow$ OD + H and $OH(v, j)$ + H $\rightarrow$ $OH(v', j')$ + H. We are interested in the OH + D reaction because of its interstellar importance [34] as well as because of a discrepancy between

the reported rate constants for this reaction.(See Table 4.1) The study of vibrational relaxation of OH in collisions with H is more of a purist interest. We choose the OH+H system as a prototype to explore vibrational relaxation dynamics in complex forming reactions, which have not been extensively studied in prior theoretical work. The collisions of OH with atomic hydrogen are also investigated as a possible pumping mechanism for the OH maser [35–38].

Two papers reporting the statistical, coupled-states studies presented in this thesis have already appeared (or will appear) in print:

- S. Atahan, M. H. Alexander and E. J. Rackham. Cross sections and thermal rate constants for the isotope exchange reaction: $D(^2S) + OH(^2\Pi) \rightarrow OD(^2\Pi) + H(^2S)$. *J. Chem. Phys.*, **123**, art. no. 204306 (2005).

- S. Atahan and M. H. Alexander. Coupled-States Statistical Investigation of Vibrational and Rotational Relaxation of $OH(^2\Pi)$ by Collisions with Atomic Hydrogen. *J. Phys. Chem. A*, (2006), (*in press*).

In addition, we completed *ab initio* calculations on the SiAr van der Waals complex (not presented in this thesis) which were published earlier:

- C. Tao, A. Teslja, P. J. Dagdigian, S. Atahan and M. H. Alexander. Laser spectroscopic study of SiAr van der Waals complexes , J. Chem. Phys., **116**, 9239 (2002) .

In the rest of the Introduction, we introduce the concept of a Potential Energy Surface (PES) as well as the basic underpinnings of collisional molecular energy

transfer. This thesis is a computational study of PESs and dynamics of small triatomic systems. We utilize the best available methods in both electronic structure theory and time-independent scattering dynamics. The details of the theory is explained to give enough background for the reader to follow the results presented.

1.1 The Potential Energy Surfaces, (PESs)

PESs are multivariable scalar functions that describe the change in the interaction energy of a system as a function of the coordinates of the nuclei. This definition is the result of the Born-Oppenheimer Approximation [39], (BOA), in which one assumes that the electronic motion is decoupled from the nuclear motion so that one can solve the electronic part of the hamiltonian independently on a grid of nuclear coordinates.

The idea of the separation of the motion of the nuclei and of the electrons is suggested by molecular spectroscopy. Molecular spectral lines can be separately assigned to electronic, vibrational or rotational transitions. This implies that to first-order the electronic and nuclear motion is separable [39].

The exact nonrelativistic Hamiltonian for an N-nuclei and n-electron system (in atomic units [40]) is

$$\begin{aligned} \mathbf{H} &= \mathbf{T_n} + \mathbf{T_{el}} + \mathbf{V_{ee}} + \mathbf{V_{nn}} + \mathbf{V_{en}} && (1.1) \\ &= -\sum_{i}^{N} \frac{1}{2M_i} \nabla^2_{\mathbf{x_i}} - \sum_{j}^{n} \frac{1}{2} \nabla^2_{\mathbf{x_j}} + \sum_{i<i'}^{n} \frac{1}{x_{ii'}} + \sum_{j<j'}^{m} \frac{Z_j Z_{j'}}{x_{jj'}} - \sum_{i,j}^{m,n} \frac{Z_j}{x_{ij}}, && (1.2) \end{aligned}$$

where the M_i are the masses of the nuclei and x_{ij} are the interparticle distances. The coordinates $\mathbf{x_i}$ and $\mathbf{x_j}$ are defined with respect to the laboratory-fixed Carte-

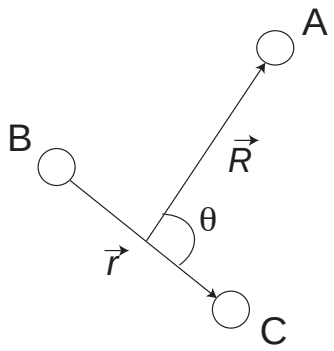

Figure 1.1: Illustration of Jacobi coordinates.

sian coordinate system for the nuclei and the electrons respectively. It is always advantageous to transfer to a Center-of-Mass (CM) coordinate system in which we separate out the overall translational motion of the system. With respect to the CM, the system is described by $3N-3$ nuclear coordinates.

In this thesis, we use Jacobi coordinates which are defined as follows: Let A, B and C be atoms of interest, and $\vec{x_i}$ be the column vectors of their coordinates relative to an origin fixed in the laboratory frame. The Jacobi coordinates then are

$$\vec{R} = \vec{x}_A - \frac{m_B\vec{x}_B + m_C\vec{x}_C}{m_B + m_C} \tag{1.3}$$

$$\vec{r} = \vec{x}_C - \vec{x}_B. \tag{1.4}$$

One of the three possible Jacobi coordinates sets are illustrated in the Fig. 1.1. The angle θ is defined as

$$\theta = \cos^{-1}(\vec{R}\cdot\vec{r}). \tag{1.5}$$

In Jacobi coordinates (after the motion of the CM is removed) the Hamiltonian

is

$$\mathbf{H} = \frac{1}{2\mu_R}\nabla^2_{\mathbf{R}} + \frac{1}{2\mu_r}\nabla^2_{\mathbf{r}} + \mathbf{H}_{el}(\vec{q};\vec{R},\vec{r}). \tag{1.6}$$

Here, $\vec{q}$ designates, collectively, the coordinates of the all electrons; μ_R and μ_r are the reduced masses for the A+BC arrangement and BC, respectively.

$$\mu_R = \frac{m_A(m_B+m_C)}{m_A+m_B+m_C}, \tag{1.7}$$

$$\mu_r = \frac{m_B m_C}{m_B+m_C}. \tag{1.8}$$

We neglect the mass-polarization [41] term which appears as a result of the coordinate transformation.

By assuming [39] that we can fix the nuclei in space and solve the Schrödinger Equation for $\mathbf{H}_{el}$ independently, we obtain a set of solutions for $\mathbf{H}_{el}$ as

$$\mathbf{H}_{el}(\vec{q};\vec{R},\vec{r})\ \phi^k_{el}(\vec{q};\vec{R},\vec{r}) = E^k_{el}\ \phi^k_{el}(\vec{q};\vec{R},\vec{r}). \tag{1.9}$$

We perform *ab initio* calculations to obtain the electronic wave functions and eigenvalues. All *ab initio* calculations in this thesis are performed with the MOLPRO [42] suite of programs. The electronic wave functions, $\phi^k_{el}(\vec{q};\vec{R},\vec{r})$, will form a complete set of orthogonal functions, in which we can expand the total wave function as

$$\Psi(\vec{q},\vec{R},\vec{r}) = \sum_k^{\infty} C_k(\vec{R},\vec{r})\ \phi^k_{el}(\vec{q};\vec{R},\vec{r}). \tag{1.10}$$

By substituting the wave function into the full Schrödinger equation, multiplying by $\phi^*_m(\vec{q};\vec{R},\vec{r})$ on the left and integrating over the electronic coordinates we obtain a set of coupled equations as follows:

$$\sum_k \left\langle \phi^m_{el} \left| \frac{1}{2\mu_R}\nabla^2_{\mathbf{R}} + \frac{1}{2\mu_r}\nabla^2_{\mathbf{r}} \right| C_k(\vec{R},\vec{r})\phi^k_{el} \right\rangle + E^m_{el}C_m(\vec{R},\vec{r}) = E_{tot}C_m(\vec{R},\vec{r}). \tag{1.11}$$

Up to this point we have not made any approximations other then neglecting the mass polarization term. Now, if we neglect all the couplings of the electronic wave functions due to the kinetic energy operator, we obtain a Schrödinger equation for the motion of the nuclei within the BOA approximation, namely

$$\left[\frac{1}{2\mu_R}\nabla^2_{\mathbf{R}} + \frac{1}{2\mu_r}\nabla^2_{\mathbf{r}} + E^m_{el}\right] C_m(\vec{R},\vec{r}) = E_{tot} C_m(\vec{R},\vec{r}). \tag{1.12}$$

The physical meaning of the BOA is that the electronic wave function will change and adapt to the motion of the nuclei instantaneously so that the system does not go through transitions between different electronic states. The success of the BOA is due to the fact that most chemical reactions are adiabatic [43, 44]. The approximation is valid only if the coupling energies due to the kinetic energy operator are small compared to the energy gaps between different energy states. In situations in which the energy gap between PESs is small, as can occur at crossings or avoided crossings, it is crucial to go beyond the BOA to understand the behavior of the system.

In dynamics calculations, when multiple PESs are involved, the matrix of the kinetic energy is not, in principle, diagonal and the coupling terms can be hard to compute [45]. Therefore, it is disadvantageous to use adiabatic PESs in the dynamics calculations. If the nonadiabatic effects are important, one would like to use a representation in which the nuclear couplings are minimal. In this basis the functions will be little affected by the changes in positions of the nuclei. This is called a diabatic representation. The spin-orbit coupling terms, in the next chapter, are reported in a diabatic representation.

1.2 Molecular Energy Transfer

For any system to reach thermal equilibrium, it is necessary to have means of energy transfer among the particles constituting the system. Energy transfer occurs either through molecular collisions or radiation. Since for most molecules in their ground electronic states radiative lifetimes are relatively long, transfer through collisions is of fundamental interest. In collisions, molecules can change their velocity, vibrational and/or rotational levels, and sometimes their electronic states. The efficiency of these various types of energy transfer reveals subtle details about the nature of the chemical interaction among molecules. The types of transfer in inelastic collisions are referred [46] to as Translation-Vibration ($T-V$), Vibration-Vibration ($V-V$), Vibration-Rotation ($V-R$) transfer, and so forth.

Chapters 3–5 of this thesis are concerned with rovibrational energy transfer in complex forming reactions. Here we will try to sketch the basic principles of this process. For the sake of simplicity, we will decouple rovibrational energy transfer into the vibrational and the rotational components and start with a simple model. However, the reader should keep in mind that nature works in complicated ways coupling all kinds of motion. Further, in principle, the motion of electrons and light atoms is accurately described only by quantum mechanics. Thus, simple arguments based on classical mechanics are only approximate.

1.2.1 Vibrational Energy Transfer

Vibrational energy transfer is important in many chemical phenomena, such as combustion processes, atmospheric events and vibrational mode selective experiments. Vibrational relaxation is the dissipation of internal energy stored in vibrational modes (in addition to the zero point energy) by means of molecular collisions or through emission of radiation. Our study is concerned only with collisional relaxation. In this section we present a general overview. This section follows closely the introduction to this topic by Lambert [47]. The interested reader can find more detail in Lambert's book [47] and elsewhere [46, 48].

Let us assume a ball and spring model consisting of a diatomic molecule AB and an atom C, illustrated in Fig. 1.2. The vibration of AB is described by a simple harmonic oscillator with a frequency, ν. We simplify further by assuming only a collinear collision between AB and C. Collinear encounters are likely to make the largest contribution to vibrational energy transfer.

Naturally, the first and foremost requirement to study atomic and molecular collisions is the availability of a PES representing the geometry dependence of the interaction. Since the collision of AB with C is restricted to be collinear, the interaction potential, $V(r, d)$, is a function of the distance r and the displacement, d of atom B from equilibrium. As atom C moves toward AB, there are two forces acting on atom B, the force exerted by the spring and the change in $V(r, d)$. We are interested in the probability of transfer of the translational energy of atom C to the vibration of AB, namely $T - V$ transfer. According to the Adiabatic The-

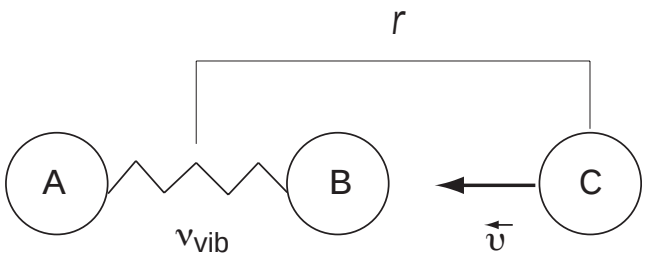

Figure 1.2: Collision between an atom and a collinear diatomic molecule.

ory of Ehrenfest [49], slow changes in the system will leave the discrete (quantized) variables of a quantum system unchanged. If the change of the force exerted by C is small during a time $1/\nu$, the vibrational period of AB, the system will behave adiabatically without a significant transfer of energy. On the other hand, if the force changes dramatically during a time $1/\nu$, then efficient transfer of energy -vibrational excitation/relaxation- occurs.

In an adiabatic limit, the vibrational energy transfer characteristics of the system can be estimated by the following argument: The rate of change in the force during the duration of a collision is proportional to the velocity of atom C. We define the collision duration as r_{int}/v, where r_{int} is the range of the collision. If

$$\frac{1}{\nu} \gg \frac{r_{int}}{v}, \tag{1.13}$$

then vibrational energy transfer will be facile. For a system at thermal equilibrium with an average speed of $v = (8kT/\pi m)^{1/2}$, higher temperatures, smaller masses and lower vibrational frequencies will favor efficient transfer.

The *Landau-Teller* (LT) formulation of vibrational energy transfer based on the adiabatic principle has been often applied to explain vibrational relaxation es-

pecially for non-polar molecules. The authors applied time-dependent perturbation theory to obtain a probability for vibrational relaxation. Their treatment neglected the long-range attractive part of the potential under the assumption that the interaction potential will be dominated by a simple exponentially repulsive term. For $v = 1 \rightarrow v = 0$ relaxation involving non-polar molecules, most experimental rate constants follow, roughly, the prediction of the LT theory:

$$log\ k_{v=1\rightarrow 0} = A - BT^{1/3}. \tag{1.14}$$

Where attractive forces are important in the interaction, as in hydrogen bonded systems or where complex formation can occur, the relaxation rate constants are found to deviate from the $T^{-1/3}$ temperature dependence predicted by Eq. (1.14). The deviations are strongest at low temperature. Relatively weak, attractive dipole-dipole interactions become more important at low collision energies. As the translational energy increases, the repulsive part of the potential predominates so that LT theory better applies.

An early, popular quantum mechanical model for vibrational relaxation is due to Schwartz, Slawsky and Herzfeld (SSH) [50] in 1952. They slightly modified the exponentially repulsive potential model from LT theory and lowered the asymptote of the interaction potential to correspond to the Lennard-Jones minimum for the particular system of interest. That way, they introduced attractive forces into the system while keeping the exponential behavior that allowed the analytical solution exploited by Landau and Teller. This SSH theory successfully predicts the qualitative form of the deviation in the $T^{-1/3}$ plots for strongly polar molecules.

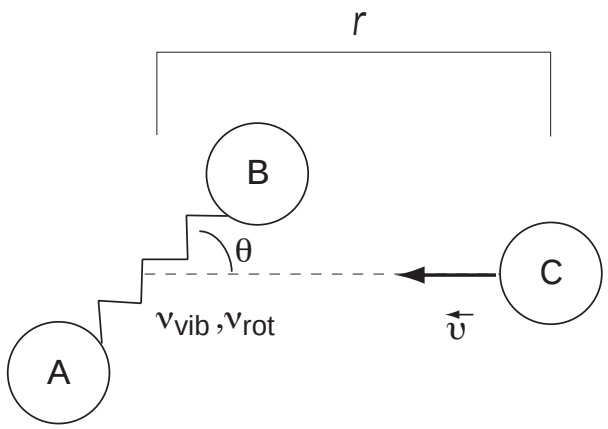

Figure 1.3: Collision between an atom and a rotating diatomic molecule.

However, the quantitative predictions are poor especially at low temperatures for polar molecules. Low temperatures and strong polarity require a more accurate treatment of how the attractive part of the potential effects the dynamics. Shin [48] introduced a more realistic Morse potential [51] with angular dependent terms [52], but which still allowed an analytical solution. The predictions based on his results gave somewhat better agreement with experiment [47].

1.2.2 Rovibrational Energy Transfer

A prediction of the efficiency of rovibrational energy transfer requires an accurate description of the angular dependence of the interaction potential. A simple picture of non-collinear atom-diatom collisions is shown in Fig. 1.3. A formulation, based on the adiabatic theory of Eq. (1.13) would still hold for rotational energy transfer, since there is an external force acting on a periodic motion. For diatomic molecules, rotational frequencies, ν_{rot}, are much smaller then vibrational frequen-

cies, ν_{vib}. Therefore, provided that the interaction times are still short, rotational energy transfer should be more efficient.

The effect of high temperature in rotational and vibrational transfer is different. As discussed earlier, the higher the translational energy the more efficient will be the $T - V$ transfer. In the case of $T - R$ transfer, it is the other way around. Rotational energy spacings increase quadratically, in contrast to vibrational energy spacings, where the spacings slightly decrease because of anharmonicity. As a result, at higher temperatures, where higher rotational levels are predominantly occupied, the rotational period will be small and it will compete with the effect of the increasing velocity of approach. Equation (1.13) is less likely to be satisfied, and thus the efficiency of $T - R$ transfer drops for high temperatures in contrast to $T - V$ transfer.

Smith pointed out [53] that whenever the collisions that lead to relaxation involve the formation of a transient collision complex, experimental observation indicates that vibrational relaxation is highly facilitated. Such systems usually involve radical-radical interactions, where complex formation corresponds to establishing a chemical bond. Vibrational relaxation rates for systems like OH+O, OH+H, O+O_2 are found to be larger than for comparable collisions with closed shell atomic partners [47, 53, 54]. For these systems, there is another, reactive pathway involving atom exchange which will result in vibrational relaxation.

The adiabatic theory would certainly not apply for the case of complex forming collisions since it requires that the collisions should be relatively fast and weak enough to be treated perturbatively. Long-lived reaction complexes with long colli-

sion times and with scrambling of motion where atoms might be exchanged and new bond formation might take place cannot be treated adiabatically. The SSH theory and its later adaptations based on the perturbation theory are doomed to failure in such cases.

The OH+H system studied in this dissertation involve the formation of a transient water complex during which vibrational relaxation is very fast [55]. Relaxation is especially efficient at low temperatures, where more of the collisions enter the complex. Once a collision complex is formed, the vibrational motion of the diatomic molecule is strongly coupled with the other degrees of freedom. The statistical method we use can allow for the formation of a complex and exchange of atoms as well as nonadiabatic effects. It is a hybrid of statistical ideas and quantum mechanical time-independent scattering theory. Thus we believe, unlike previous approaches, it will allow to investigate the nature of rovibrational relaxation pathways which proceeds by means of transient collision complexes.

The study of vibrational relaxation of OH in collisions with H atoms is the topic of Chapter 5. As introduced in the previous paragraph, the deceptively simple encounter of a hydrogen atom with OH involves formation of a collision complex. Also, the presence of multiple PESs complicates the theoretical investigation. In this prototypical system, we apply statistical, coupled-states scattering theory to investigate the nature of the vibrational and rotational relaxation processes and assess the role of the complex formation.

Chapter 2

An *Ab initio* Investigation of the $O(^3P) + H_2(^1\Sigma_g^+)$ System

2.1 Introduction

The reaction of ground-state oxygen atoms with molecular hydrogen is one of a few triatomic reactions which has been studied intensively by theoreticians. This reaction is particularly important in combustion chemistry. Oxidation of hydrogen in the early stages of the combustion of hydrocarbons contributes to the later stages of hydrocarbon oxidation [5]. In shocked interstellar clouds, the reaction is responsible for altering the oxygen chemistry [56]. The reaction is also of some importance to atmospheric chemistry [57]. In principle, the reaction provides a good test of our ability to model the dynamics in a fully a *priori* manner. It is a system which has only ten electrons so that *ab inito* PESs can be determined with high accuracy. A proper description of the $O+H_2$ reaction must include multiple PESs and spin-orbit coupling. The understanding of the role of these subtleties will provide guidelines for the understanding of more complex reactions.

Many aspects of the title reaction have been studied in the last 50 years; and yet still draw considerable attention as better algorithms and computational power become available. Thanks to the extensive work of scientists in the last several decades, there have appeared many studies of the PESs [2, 6, 14–21], in particular the van der Waals region [16, 21–23, 31], of the kinetics [2–13], isotope

exchange [58–61], state selective dynamics [62], intersytem crossing and nonadiabatic effects [24, 25], all these based on quasi classical trajectory [14, 63], and quantum mechanical calculations [26–30].

2.1.1 Previous Work on the Potential Energy Surfaces of $O(^3P)$ + H_2

There has been a considerable amount of work on the PESs for the $O(^3P)$+H_2 system. The first PES was a LEPS function generated in 1967 by Westenberg and deHaas [2]. It was followed by a second LEPS surface by Johnson and Winter [14]. These LEPS surfaces were obtained by adjusting only one (Sato parameter) parameter to the experimental findings and did not quite agree. (Both report a barrier height around 12 kcal/mol) The work of Gangi and Bader [64] was the first *ab initio* calculation done on the system. This gave a barrier height of 35 kcal/mol. The valence bond-diatomics-in-molecules (DIM) PES of Whitlock *et al.* [65] and quasi-classical trajectory calculations based on this gave better agreement with the experimental rates. Howard, McLean and Lester [15] determined cuts in the PESs using *ab initio* methods.

The first detailed *ab inito* calculation of the reaction was done by Walch *et al.* [66]. They calculated the barrier heights and transition state geometries analyzing in detail the affect of basis set, the choice of the orbitals and of the reference configurations. Subsequently, Walch, Wagner, Schatz, Bowman and coworkers published many analysis of the reaction in a series of papers [6–8, 17, 59, 60]. They

made a detailed comparison of theoretical rate constants obtained for the PESs available at the time of the study [7, 17]. They also performed reaction dynamics studies [8, 9, 59, 60] Although the comparisons of the rate constants estimated based on the various PESs mentioned above agreed with experiment, the location of the saddle point, the height of the barrier and the exothermicity of these surfaces remained in question [8].

A recent paper by Rogers *et al.* [20] presented chemically accurate (accuracy within *ca.* 0.3 kcal/mol) *ab initio* PESs for the lowest $^3A'$ and $^3A''$ states of $O(^3P)+H_2 \rightarrow OH(^2\Pi) + H(^2S)$. Quantum reactive scattering [26, 30] and quasiclassical calculations [27] based on these surfaces agreed with the crossed molecular beam excitation functions reasonably well except fo low energy collisions. Rogers *et al.* did not include the spin-orbit Hamiltonian in the calculations. Their justification was based on the fact that the spin-orbit splitting of the ^3P state of the oxygen atom (the splitting of $^3P_1$ and $^3P_0$ is *ca.* 0.2 kcal/mol) is within the estimated accuracy of the surfaces.

More recently, Brandão and coworkers rebuilt the $^3A''$ surface to obtain a better long-range description [21], since the global fits of Rogers *et al.* [20] failed to describe the van der Waals region accurately. Brandão and coworkers used the *ab initio* data avaliable [20] to generate a surface using a double many-body expansion formalism. Their findings on the van der Waals minimum and shape did not agree with the previous calculations satisfactorily, and they concluded that more studies were needed.

2.1.2 Spin-Orbit Coupling

Only a few experimental studies have been performed to look at the effect of spin-orbit coupling in the $O(^3P) + H_2$ reaction. In a molecular beam non-reactive scattering study, Aquilanti *et al.* [31] studied the spin-orbit dependence of the PES for the long-range region. Together with adiabatic potential energy curves they also obtained nonadiabatic couplings between these adiabatic states. Another important experimental study of the reaction was performed by Westenberg and deHaas [2]. They studied the isotope effect by ESR, substituting D_2 for H_2, and were able to compare the rate constants for O atoms in the two lower spin-orbit states, both of which correlate with the OH product molecule in their electronic ground state (see Figure. 2.1). However, because of the inadequacy of the technique used, they could detect no difference in the reaction rate for the lowest two spin-orbit states.

There have been important theoretical advances in the effect of the spin-orbit couplings on the reaction cross sections for the title problem. Schatz and coworkers [25, 32] studied intersystem crossing effects in the $O(^3P,^1D) + H_2 \rightarrow OH(^2\Pi) +$ H reaction. (The crossing of the insertion, $O(^1D)$ + H, and abstraction, $O(^3P)$ + H, pathways are schematically illustrated in Fig. 2.1.) They treated the various spin-orbit coupling constants by complete active space self-consistent field (CASSCF) methods. They found that the spin-orbit couplings increased the triplet O + H_2 cross sections and product rotational excitation. A recent quantum wave-packet study by Chu *et al.* [33] indicated that the spin-orbit couplings among the triplet states of different symmetry is more important then the singlet-triplet coupling.

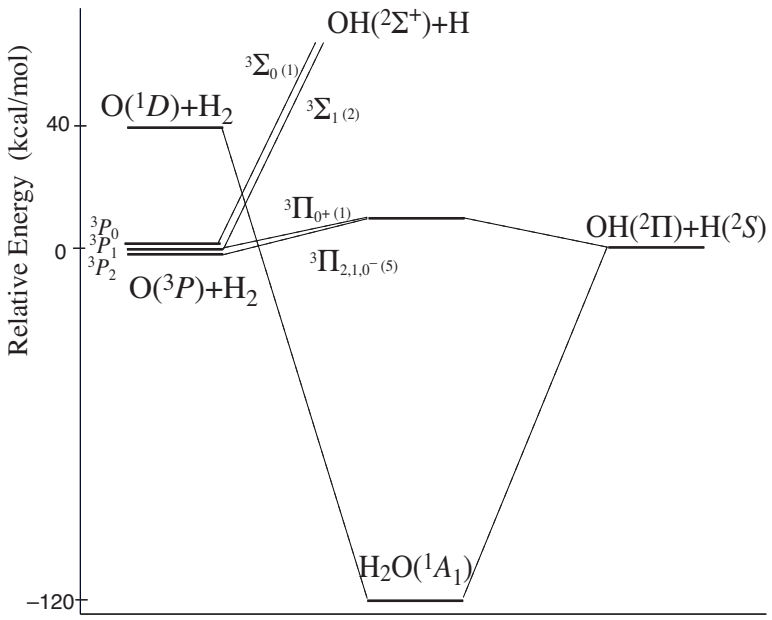

Figure 2.1: Schematic plot of the energy diagram of the $O(^3P,^1D)+H_2$ reaction for the collinear arrangement.

For this much studied system, in this Chapter we present our *ab initio* findings on the van der Waals valley to assess the accuracy of the available surfaces and fits. An accurate description of the van der Waals region is especially important in cold collisions [67]. In addition, for possible future studies on the nonadiabatic effects, similar to work of Alexander and coworkers on the $F+H_2$ reaction [68], we investigated the full geometry dependence of the spin-orbit coupling terms. In the following sections, we discuss the energetics of the system, the study of the van der Waals valley by coupled-cluster [CCSD(T)] and multi-reference configuration interaction (MRCI) methods, and the spin-orbit coupling terms for the system. The chapter ends with a brief conclusion.

2.2 The Energetics and the Orbital Occupancies in the O(^{3}P) + H_2 System

The O(^3P)+H_2 reaction proceeds through an abstraction mechanism to yield OH($^2\Pi$) and H(^2S). The orbital occupancies of the oxygen and the molecular hydrogen are $1s^2 2s^2 2p^4$ and $1\sigma^2$, respectively. In the reaction, one electron leaves H_2 bonding orbital to form a new bond with one of the unpaired electrons of the oxygen atom. In collinear geometry, the orbital occupancies of the mixed atomic/molecular and full molecular orbital description are as follows:

$^3\Pi$

$$1s^2 2s^2 1\sigma_g^2 2p_z^1 2p_x^1 2p_y^2 = 1\sigma^2 2\sigma^2 3\sigma^2 4\sigma^1 1\pi^3 \quad (2.1)$$

$$1s^2 2s^2 1\sigma_g^2 2p_z^1 2p_x^2 2p_y^1 = 1\sigma^2 2\sigma^2 3\sigma^2 4\sigma^1 1\pi^3 \quad (2.2)$$

$^3\Sigma^-$

$$1s^2 2s^2 1\sigma_g^2 2p_z^2 2p_x^1 2p_y^1 = 1\sigma^2 2\sigma^2 3\sigma^2 4\sigma^2 1\pi^2 \quad (2.3)$$

Here, 1σ, 2σ and 1π denote the $1s$, $2s$ and $2p_\pi$-like atomic oxygen orbitals, which are mostly inactive in the reaction. The 3σ and 4σ orbitals represent the bonding and antibonding interaction of O($2p_z$) with the 1σ orbital of the H_2 molecule. Asymptotically, 3σ corresponds to the H_2 ground state and 4σ corresponds to the $2p_z$ orbital of the oxygen. As the H_2 approaches the oxygen atom collinearly, the degeneracy of the ^3P state is lifted, and gives rise to $^3\Sigma$ and $^3\Pi$ states. This is illustrated in Fig. 2.2. Throughout the chapter, the z-axis is assumed to lie along the H_2 bond axis and the y-axis, perpendicular to the molecular plane. The $^3\Sigma$ state is

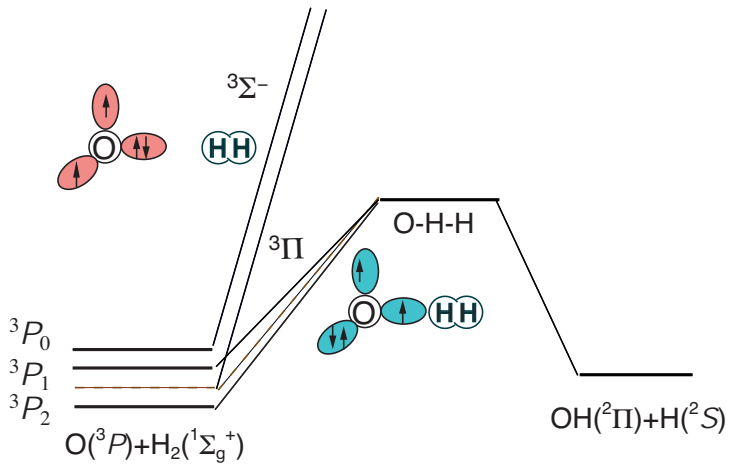

Figure 2.2: Schematic correlation diagram for the O$-p$ orbitals in collinear geometry. The degeneracy of the $^3\Pi$ state will be lifted in bent geometries. (Note that only one lobe of the each p orbital is drawn for clarity.)

very repulsive because the doubly occupied p_z orbital has no room to accommodate an electron from the 1σ orbital of the H_2. Thus, only the $^3\Pi$ state correlates directly with the electronic ground state of the products OH($^2\Pi$) + H(^2S) [66].

In bent geometry, because of the different interactions between the nonbonding p-electrons, the $^3\Pi$ state will further split into two states classified in terms of their reflection symmetries as $^3A'$ and $^3A''$. In a perpendicular arrangement, the electronic states are labeled by the $^3B_1$, $^3B_2$ and $^3A_2$ irreducible representations.

The spin-orbit Hamiltonian couples together all three states. Asymptotically, at large O(^{3}P)$-H_2$ distances, the nine-fold degeneracy of the ^3P state of the oxygen atom splits into three states: $^3P_2$ (5), $^3P_1$ (3), $^3P_0$ (1). (The degeneracy of the each state is given in parentheses). In collinear geometry ($C_{\infty v}$ point group), all five components of the $^3P_2$ and one component of the $^3P_1$ state correlate with the $^3\Pi$ state.

(Figure 2.2) The other states correlate with the $^3\Sigma^-$ state. Specifically, (shown in Fig. 2.1) the $^3P_2$ state correlates with $^3\Pi_{\pm 2}$, $^3\Pi_{\pm 1}$, $^3\Pi_{-0}$, the $^3P_1$ state correlates with $^3\Pi_{+0}$, $^3\Sigma^-_{\pm 1}$ and $^3P_0$ state correlates with $^3\Sigma^-_0$. Since only the $^3\Pi$ states are reactive, and the ^3P_j states correlate differently, we certainly expect different reactivities for the three spin-orbit states. Consequently, if there is no nonadiabatic coupling we would expect the relative reactivity to be $5:1:0$ for $^3P_2$, $^3P_1$ and $^3P_0$, respectively.

2.3 Weakly Bound $O(^3P)-H_2$ Complex

A weakly-bound complex is defined by the existence of a well in the long-range part of the PES which is much less deep than a well of a typical chemical bond. The strength of these van der Waals interactions are determined by electrostatic, induction and dispersion contributions [69]. The electrostatic energy is the interaction energy of the permanent charge distributions of the species (such as dipole-dipole, charge-dipole, ...etc.), whereas the induction energy represent the interaction energy between a multipole induced by the permanent charge distributions of the neighbouring species, such as charge-induced dipole, or dipole-induced dipole. The third contribution, dispersion is the interaction due to the correlation between two instantaneous dipole associated with the movement of the electrons.

Van der Waals complexes are especially important in low energy collisions, where the orientation of the molecules may affect the outcome of the reaction substantially [70]. Therefore, it is important to have a good description of the long-range part of the potential energy surface. In this section, we investigate the van der Waals

valley of the $O(^3P)-H_2$ complex.

2.3.1 Coupled Cluster Calculations

Coupled cluster [CCSD(T)] methods [71, 72], which are size extensive, are widely used in the calculations for long-range van der Waals potentials. The advantage with respect to CI calculations, truncated to include only single and double excitations (CISD), is the recovery of more electron correlation energy by inclusion of triple excitations perturbatively. The disadvantage, however, is that current CCSD(T) methods are single reference methods, *i.e.* applicable to electronic states that can be described by a single reference configuration state function.

We performed *ab initio* calculations for the $O(^3P)-H_2$ van der Waals region in $C_{\infty v}$ and in C_{2v} geometries. The CCSD(T) method is known to recover a large fraction of the electron correlation contribution to the van der Waals interaction [73]. In particular, we employed a RCCSD(T) (Restricted-Coupled-Cluster) method based on a RHF (Restricted-Hartree-Fock) wave function. In those calculations, the t_1 diagnostic was always observed to be less than 0.02.

In order to correct for the Basis Set Superposition Error (BSSE) we added Counterpoise Corrections (CP) [74]. In this technique the interaction energy is calculated as

$$V(R, r, \theta) = E_{O-H_2}(R, r, \theta) - E_{H_2}(R, r, \theta) - E_O(R, r, \theta), \tag{2.4}$$

where the energies of the fragments are calculated in the supermolecular basis.

Another challenge in electronic structure calculations is posed by the degree of

saturation of the orbital basis sets used. Fortunately, by systematically increasing the size of the basis set, it is possible to extrapolate to the Complete Basis Set (CBS) limit [19]. Another method to reach the CBS limit is to add midbond basis functions to the basis instead of increasing the number of nuclear-centered functions [75]. In order to check the behavior of the augmented bases with midbond functions, we have performed restricted coupled-cluster [RCCSD(T)] calculations with the augmented correlation-consistent polarized valence-(double/triple/quadruple)-zeta (aug-cc-pVnZ, n = D, T and Q) basis function sets of Dunning *et al.* [76, 77] with addition of a set of midbond functions of Tao and Pan [75]. Following these methods, we used midbond $3s$ and $3p$ functions with exponents $(0.9, 0.3, 0.1)$; $2d$ and $2f$ functions with exponents $(0.6, 0.2)$; and a single g function with exponent (0.3).

Figure 2.3 plots the van der Waals well depths as a function of the augmented basis set size in $C_{\infty v}$ and C_{2v} geometries. The double-zeta [aug-cc-pVDZ ($n = 2$)] energies are artificially lower than the bigger bases. The $n = 3$ and $n = 4$ results look quite similar, and our test calculation with an $n = 5$ basis for $\theta = 0^\circ$ [Fig. 2.3, panel (a)] also confirms that the aug-cc-pVQZ ($n = 4$) basis with addition of midbond functions is quite accurate and maintains the basis set saturation.

Figure 2.4 shows the van der Waals region of the potential energy surfaces in the $C_{\infty v}$ and C_{2v} geometries calculated by RCCSD(T) method. Table 2.1 summarizes the Van der Waals well depth in various basis sets for the PESs in C_{2v} and $C_{\infty v}$ geometries and compares them to earlier reported results. Our calculations confirm the earlier MRCI results of Alexander for both the well depth and the minimum

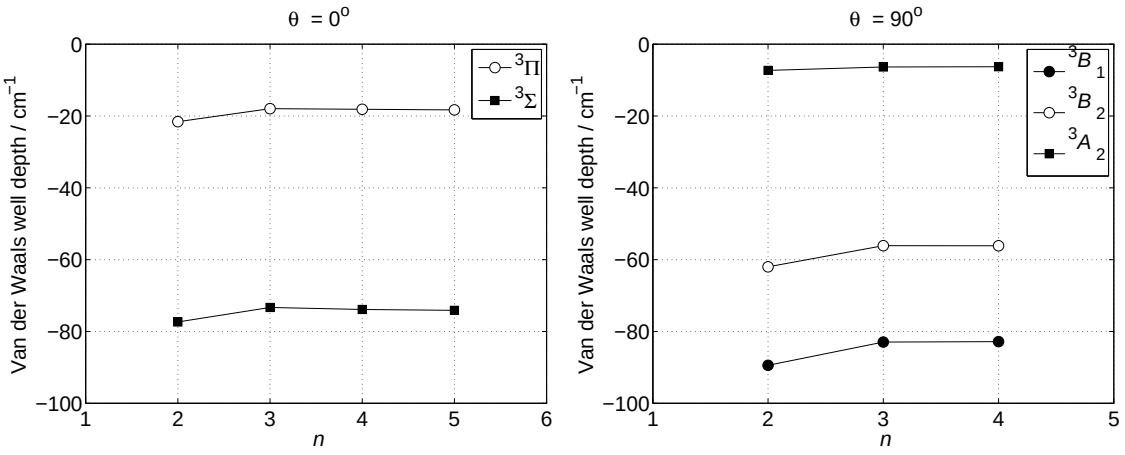

(a) $C_{\infty v}$ (b) C_{2v}

Figure 2.3: Van der Waals well depth for various PESs in (a) $C_{\infty v}$ and (b) C_{2v} geometries calculated by the RCCSD(T) method as a function of the size of the aug-cc-pVnZ basis. The basis also includes midbond functions as explained in the text. The H_2 bond distance is fixed at $r = 1.402$ a.u.

geometry. In this detailed study of the Van der Waals region, Alexander could not reproduce the results of Li, Apkarian and Harding (LAH) [22] and suggested that the authors had over estimated the van der Waals well depth of the system. Recently, Brandão and coworkers refitted the earlier calculations of Rogers *et al.* [20] and estimated much larger well depths than what had been reported on the system up to date as shown in Table 2.1. Thus, we believe that the fitting method Brandão and coworkers applied greatly exagerates the van der Waals well depths and fails to estimate the shape of the minimum on the surfaces.

Having a good approximation to the van der Waals region of the PESs, now, we wish to investigate the van der Waals region by the MRCI method.

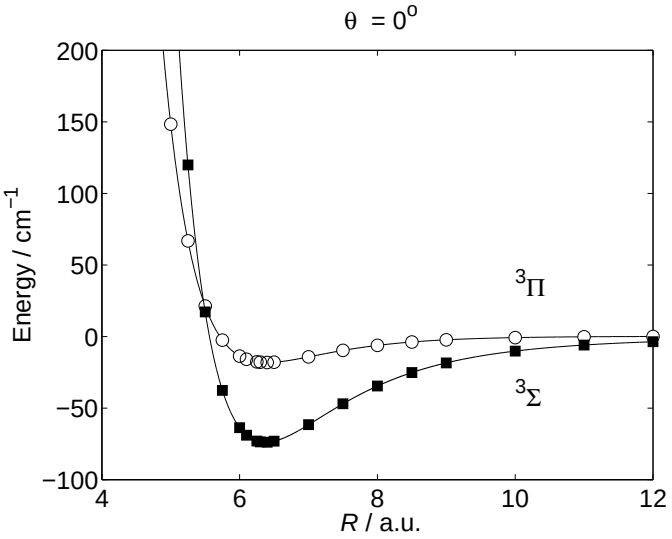

(a) $C_{\infty v}$

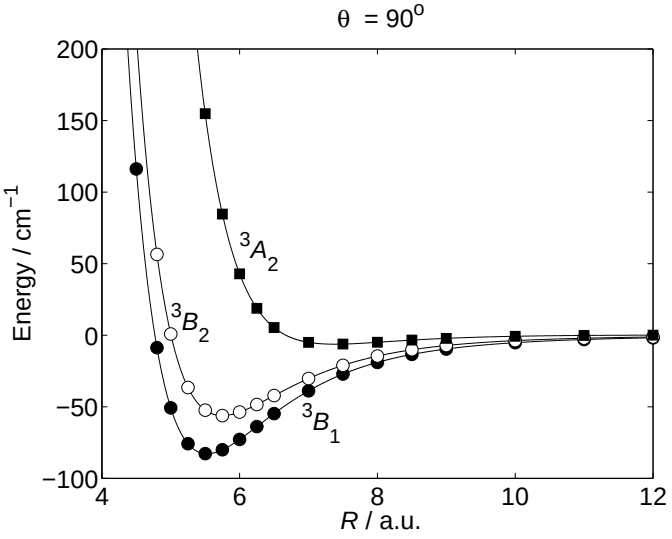

(b) C_{2v}

Figure 2.4: PESs in (a) $C_{\infty v}$ and (b) C_{2v} geometries calculated with RCCSD(T) method with an aug-cc-pVQZ basis with additional midbond functions for fixed values of $\theta = 0°, 90°$ and $r = 1.402$ a.u.

Table 2.1: Van der Waals well depth and position of $O(^3P)-H_2$ complex in various earlier work and present RCCSD(T) calculations with aug-cc-pVQZ basis with additional midbond functions.

		$C_{\infty v}$	C_{2v}
Alexander [23] (MRCI)	Energy	−74.4	−76.9
	R	6.34	5.55
Alexander [23] (CCSD(T))	Energy	−72.0	−78.9
	R	6.39	5.56
Atahan (CCSD(T))	Energy	−73.9	−82.8
	R	6.37	5.53
Brandão [21] BMS1	Energy	−175.6	−92.2
	R	6.2	6.3
Brandão [21] BMS2	Energy	−124.9	−70.2
	R	6.4	6.4
Jaquet [16] (CEPA)	Energy	−87.8	−72.4
	R	6.2	6.2
Li [22](MRCI)	Energy	−109.7	−96.6
	R	6.0	5.5

2.3.2 MRCI Calculations for C_{2v} and $C_{\infty v}$ Geometries

In this section, we present PESs for the $O+H_2$ reaction in the entrance region calculated by IC-MRCI (internally contracted multireference configuration interaction) method. MRCI methods in general are used in calculation of global PESs where the bond breakage and formation are inevitable and electron correlation is also very important. Full CI methods are very expensive to apply. Therefore, CI expansion truncated to include single and double excitations [MRCI(SD)] is widely

employed in PES calculations.

The basic sources of error in those methods are the errors due to basis set limitations, the use of the incomplete configuration expansion (truncation of the CI expansion) and the size consistency errors. The basis sets used in this work are the augmented correlation consistent basis sets of Dunning. (see Section 2.3.1) The interaction energy is calculated according to Eq. (2.4) and then extrapolated to the Complete Basis Set (CBS) limit according to [19]

$$E_n = E_\infty + B\mathrm{e}^{-(n-1)} + C\mathrm{e}^{-(n-1)^2} \tag{2.5}$$

where n is the cardinal number of the basis sets ($n = 2, 3, 4, 5$ for DZ, TZ, QZ and 5Z sets, respectively) and E_n is the corresponding electronic energy. The energy at the CBS limit, E_∞, which corresponds to the limit $n \to \infty$, is obtained by solving a set of linear equations. In our calculations, the largest basis we used is the aug-cc-pVQZ basis where $n = 4$.

In MRCI methods, the reference SCF wave function contains more than one configuration. The reference space wave function is chosen to describe all possible dissociation pathways, which requires an expansion over more than one configuration. In the MCSCF method both the coefficients in this expansion and the orbitals are optimized. After the multiconfiguration wave function is obtained, a CI expansion (SD) is written based on this MCSCF wave function and this time only the CI coefficients are optimized variationally (MRCI). The active space we have used in our system consists of $2s2p_x2p_y2p_z$ orbitals of oxygen and $1\sigma 1\sigma^*$ orbitals of H_2 molecule.

Some of the errors due to neglecting the higher-order excitations in the CI expansion can be approximately recovered by the Davidson correction [78, 79], which is denoted as MRCI+Q. The Davidson correction recovers some of the electron correlation as well as reducing the size consistency errors that are typical of truncated CI methods, but unfortunately not completely. In order to correct the surfaces for those errors, we have calculated the size consistency errors in the various geometries as follows:

$$\Delta E_{SC} = E_{\mathrm{O-H_2}}(\infty) - E_{\mathrm{H_2}} - E_{\mathrm{O}}. \tag{2.6}$$

ΔE_{SC} is the correction for the residual size consistency in the calculations.

Another difficulty we encountered in the calculations was the instability caused by the mixing of the 1σ and 2σ orbitals. A MCSCF wave function is invariant with respect to the transformations of 1σ and 2σ orbitals, but typical MRCI calculations are not since only the 2σ orbital is correlated. In order to overcome this difficulty, we carried out a two step MCSCF calculation as suggested earlier by Stark and Werner [80]. In the first MCSCF step, we kept the 1σ and 2σ orbitals doubly occupied so that these orbitals could be uniquely defined as eigenfunctions of an effective fock operator. In the subsequent MCSCF calculation, we kept the 1σ orbital from the previous calculation frozen while the 2σ orbital was treated as active. The orbitals from this two-step calculation are then used in the subsequent MRCI calculations where the 1σ orbital is not correlated. All MRCI calculations were done in this manner.

In Fig. 2.5, we compare the van der Waals region of the interaction energy,

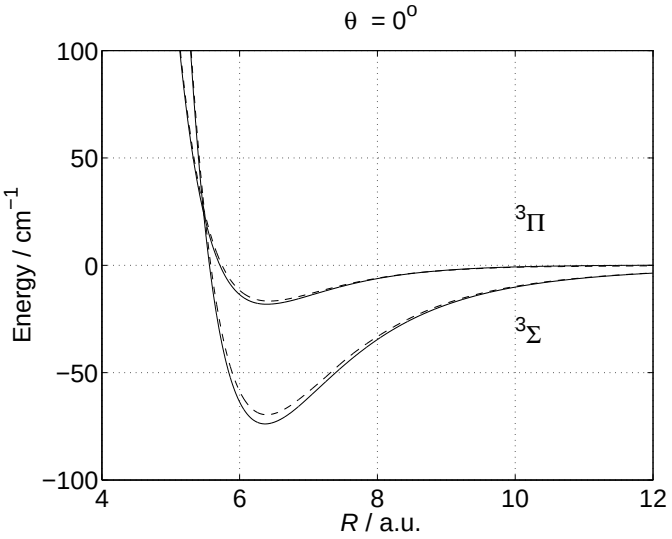

(a) $C_{\infty v}$

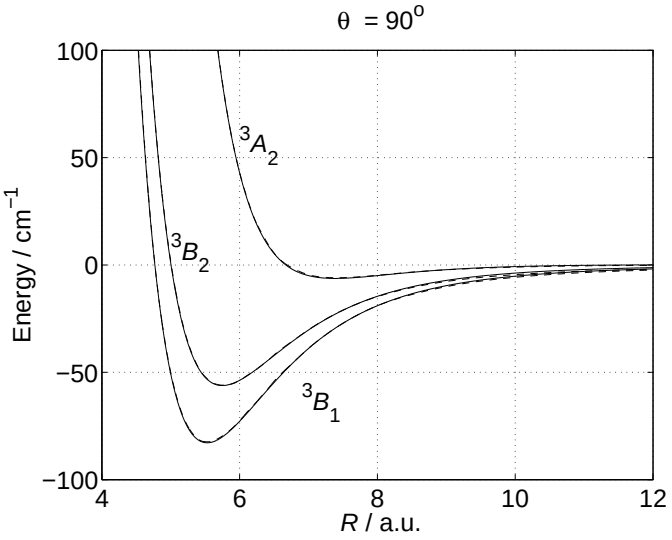

(b) C_{2v}

Figure 2.5: The comparison of the PESs in (a) $C_{\infty v}$ and (b) C_{2v} geometries calculated with RCCSD(T) method with an aug-cc-pVQZ basis with additional midbond functions for fixed values of $\theta = 0°, 90°$ and $r = 1.402$ a.u. (straight lines) with the MRCI+Q results extrapolated to the CBS limit (dashed-lines)

Table 2.2: Van der Waals well depth (cm^{-1}) of the $O(^3P)-H_2$ complex obtained by MRCI+Q and RCCSD(T) methods for various states and geometries.

Method	$C_{\infty v}$		C_{2v}		
	$^3\Sigma$	$^3\Pi$	$^3A_2$	$^3B_2$	$^3B_1$
MRCI+Q(CBS)	−69.6	−16.7	−5.9	−56.0	−82.4
RCCSD(T)(avqz+bf)	−73.9	−18.1	−6.3	−56.2	−82.8

$V(R, r, \theta)$ [See Eq. (2.4)], calculated with IC-MRCI+Q and RCCSD(T) methods. RCCSD(T) and MRCI+Q results in the CBS limit are quite close in collinear geometry and almost identical in perpendicular (C_{2v}) geometry. Table 2.2 lists the values of the van der Waals well depth of various surfaces in C_{2v} and $C_{\infty v}$ geometries. Based on the close proximity in the well depths, we conclude that MRCI+Q calculation at the CBS limit with the active space described earlier would be adequate to recover enough correlation energy for the entrance channel of $O+H_2$ reaction to describe the van der Waals interaction correctly.

We performed MRCI calculations on a grid defined by the Jacobi coordinates, R =20, 18, 16, 14, 13, 12, 11, 10, 9, 8.5, 8, 7.5, 7.25, 7, 6.75, 6.5, 6.4, 6.3, 6.25, 6.1, 6, 5.75, 5.6, 5.55, 5.5, 5.45, 5.35, 5.25, 5, 4.5, 4.25, 4, 3.75, 3.5, 3.0 and r =1.05, 1.2, 1.3, 1.402, 1.5, 1.722, 1.888, 2.3, and $\theta = 0^o$ and $\theta = 90^o$.

In Figures 2.6-2.8, we plot the (R, r)-dependent contours of the van der Waals region of the entrance channel PESs. We see that the $^3\Sigma$ and $^3B_1$ surfaces have the deepest van der Waals well, especially as a function of the H_2 stretch. This is due to the strong quadrupole-quadrupole interaction. A larger induction interaction occurs for those electronic states where the doubly occupied p orbital is aligned collinearly in

$^3\Sigma$ and perpendicularly in $^3B_1$ symmetries. The $^3B_2$ surface shows a similar pattern with a shallower interaction region. The $^3\Pi$ surface extends into the reaction region as R gets smaller and r is stretched. The reaction path is defined by the behavior of this surface. However, the barrier height and the saddle point geometry cannot be determined by the $V(R, r, \theta)$ shown in this figure. The saddle point geometry, reported by Rogers [20] and coworkers is at $R = 2.3$ a.u. and $r = 1.7$ a.u., out of the range spanned by R and r in this figure. Moreover, since this interaction energy, described by Eq. 2.4, does not include the diatomic H_2 potential, it is not sufficient to determine the saddle point geometry and the barrier height.

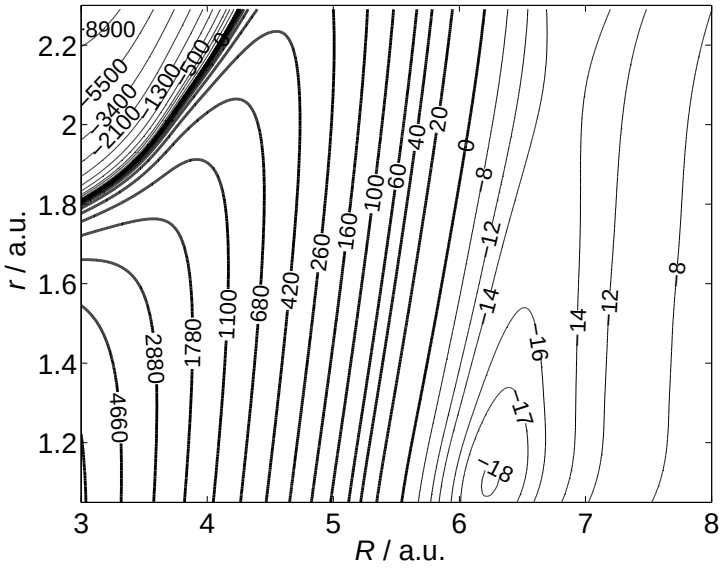

(a) $^3\Pi$

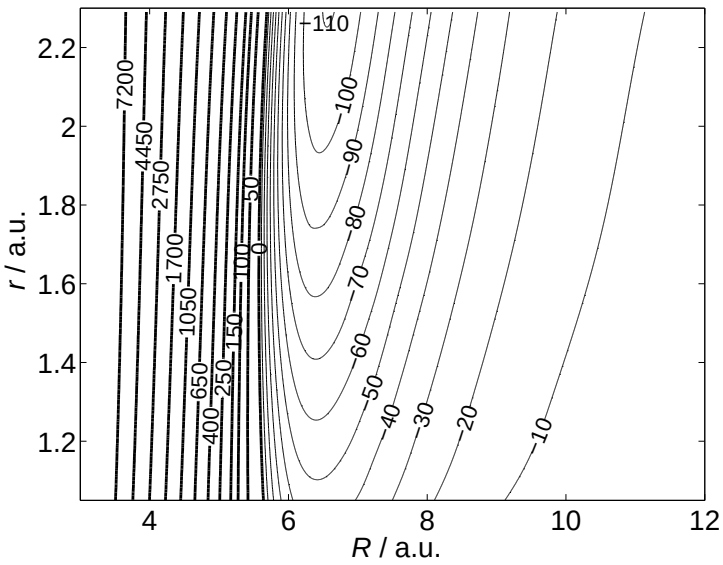

(b) $^3\Sigma$

Figure 2.6: (R, r)-dependence of interaction energies in $^3\Pi$ (a) and in $^3\Sigma$ (b) symmetries. Note that the interaction energy, $V(R, r, \theta)$, does not include the diatomic H_2 potential. ($\theta = 0^o$, Energies in cm^{-1})

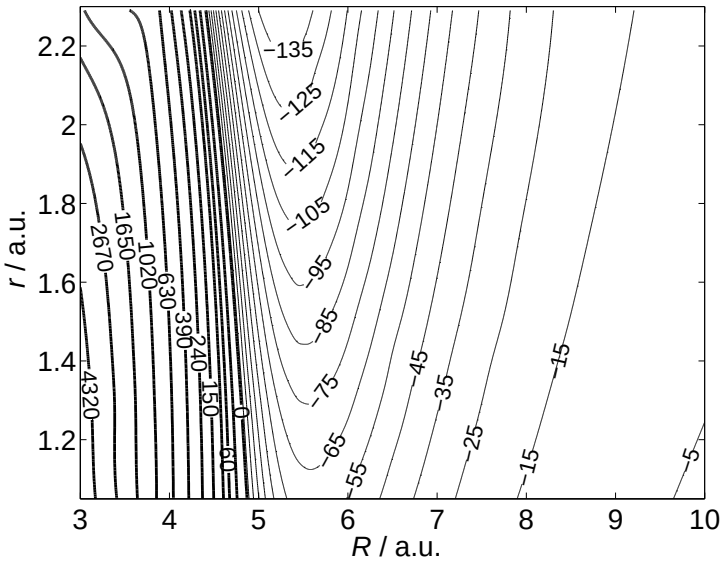

(a) $^3B_1$

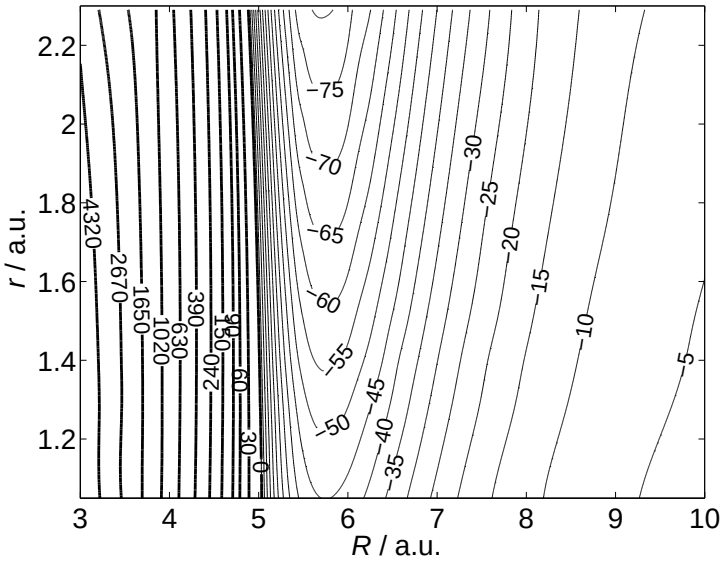

(b) $^3B_2$

Figure 2.7: (R, r)-dependence of energies in $^3B_1$ (a) and in $^3B_2$ (b) symmetries. ($\theta = 90^o$, Energies in cm^{-1})

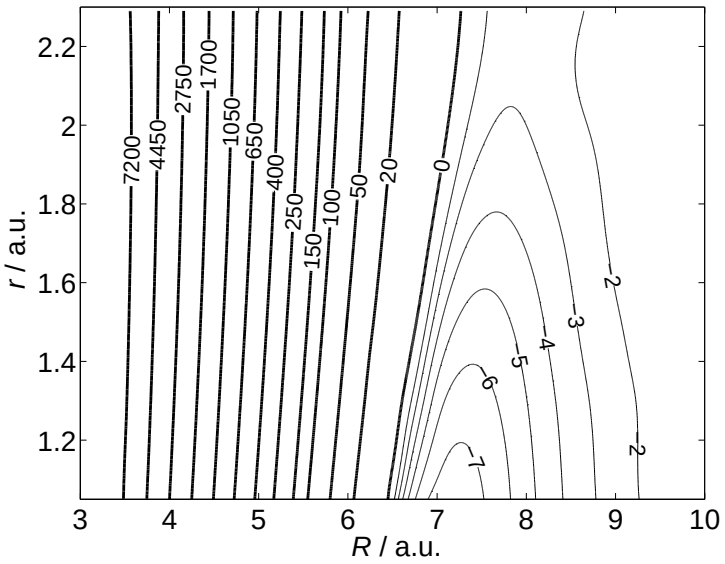

Figure 2.8: (R, r)-dependence of energies in ${}^3A_2$ symmetry. ($\theta = 90^o$, Energies in cm^{-1})

2.4 Spin-Orbit Coupling

In this section, we present a study of the spin-orbit coupling in the $\mathrm{O}({}^3P) + \mathrm{H}_2$ system. As discussed earlier, we determine the matrix of the spin-orbit Hamiltonian in a diabatic basis. The following subsection summarizes the diabatic representation we used.

2.4.1 Diabatic Representation

The diabatic representation we used [68] is formed by nine states, which are characterized by the projections of the electronic angular momentum $\lambda(-1, 0, 1)$ and of the spin angular momentum $\sigma(-1, 0, 1)$ along the vector R. Therefore, the basis functions are labeled as $|\lambda\sigma\rangle$. The matrix elements for the electronic Hamiltonian

are defined as follows:

$$\langle \lambda' \sigma' | H_{el} | \lambda \sigma \rangle = V_{\lambda' \lambda}(R, r, \theta) \delta_{\sigma' \sigma} \tag{2.7}$$

The $V_{\lambda' \lambda}$ terms represent the interaction due to the electronic Hamiltonian independent of spin. Since $V_{\lambda' \lambda} = V_{-\lambda' -\lambda}$ [81], there are four independent $V_{\lambda' \lambda}$ terms (or diabatic PESs). Because the electronic Hamiltonian is independent of spin, the electrostatic interaction matrix blocks into three 3×3 matrices corresponding to each spin projection quantum number. This 3×3 matrix is (in the so-called definite-m basis):

$$H_{el} = \left(\begin{array}{c|ccc} \lambda & 1 & 0 & -1 \\ \hline 1 & V_{\Pi} & V_1 & V_2 \\ 0 & V_1 & V_{\Sigma} & -V_1 \\ -1 & V_2 & -V_1 & V_{\Pi} \end{array} \right) \tag{2.8}$$

In the Cartesian basis, the equivalent form for 3×3 Hamiltonian matrix is defined by:

$$H_{el} = \left(\begin{array}{c|ccc} \lambda^{\sigma} & \Pi_y^1 & \Pi_x^1 & \Sigma^1 \\ \hline \Pi_y^1 & V_{yy} & 0 & V_{yz} \\ \Pi_x^1 & 0 & V_{xx} & 0 \\ \Sigma^1 & V_{yz} & 0 & V_{zz} \end{array} \right) \tag{2.9}$$

The relation between the interaction potential terms appear in the definite-m, and in the Cartesian basis are $V_{\Sigma} = V_{zz}$, $V_{\Pi} = (V_{yy} + V_{xx})/2$, $V_2 = (V_{xx} - V_{yy})/2$, and $V_1 = V_{xz}/\sqrt{(2)}$.

The Cartesian diabatic basis can be transformed into the adiabatic basis by

the following transformation:

$$\begin{bmatrix} 1A'' \\ 2A'' \\ 1A' \end{bmatrix} = \begin{bmatrix} \cos\gamma & \sin\gamma & 0 \\ -\sin\gamma & \cos\gamma & 0 \\ 0 & 0 & 1 \end{bmatrix} \begin{bmatrix} \Pi_y \\ \Sigma \\ \Pi_x \end{bmatrix} \tag{2.10}$$

where γ is a function of (R, r, θ). The singly-degenerate adiabatic and the diabatic states of A' reflection symmetry are identical. For collinear geometry, the diabatic and adiabatic states are the same. In order to perform this transformation, there are various approximate diabatization schemes. The mixing angle can be obtained from diagonalization of some property matrix [82] or from the analysis of configuration interaction vectors, [83]. In our investigation of the angular dependence of the spin-orbit terms we employed the former method.

The spin-orbit matrix is fully determined by two distinct matrix elements which are defined as follows:

$$A(R, r, \theta) \equiv \langle \Pi_x | H_{so} | \Sigma \rangle , \tag{2.11}$$

$$B(R, r, \theta) \equiv i \langle \Pi_x | H_{so} | \Pi_y \rangle . \tag{2.12}$$

where

$$\lim_{R\to\infty} B = \lim_{R\to\infty} A. \tag{2.13}$$

Based on these definitions of the spin-orbit matrix elements, the spin-orbit Hamil-

tonian in the Cartesian basis is:

$$H_{so} = \frac{1}{\sqrt{2}} \left| \begin{array}{c||cccccccccc} (\Lambda^{\sigma}) & \Pi_y^1 & \Pi_x^1 & \Sigma^1 & \Pi_y^0 & \Pi_x^0 & \Sigma^0 & \Pi_y^{-1} & \Pi_x^{-1} & \Sigma^{-1} \\ \hline\hline \Pi_y^1 & 0 & B\sqrt{2} & 0 & 0 & 0 & -A & 0 & 0 & 0 \\ \Pi_x^1 & -B\sqrt{2} & 0 & 0 & 0 & 0 & iA & 0 & 0 & 0 \\ \Sigma^1 & 0 & 0 & 0 & A & -iA & 0 & 0 & 0 & 0 \\ \Pi_y^0 & 0 & 0 & A & 0 & 0 & 0 & 0 & 0 & -A \\ \Pi_x^0 & 0 & 0 & iA & 0 & 0 & 0 & 0 & 0 & iA \\ \Sigma^0 & -A & -iA & 0 & 0 & 0 & 0 & A & -iA & 0 \\ \Pi_y^{-1} & 0 & 0 & 0 & 0 & 0 & A & 0 & -B\sqrt{2} & 0 \\ \Pi_x^{-1} & 0 & 0 & 0 & 0 & 0 & iA & B\sqrt{2} & 0 & 0 \\ \Sigma_y^{-1} & 0 & 0 & 0 & -A & -iA & 0 & 0 & 0 & 0 \end{array} \right| ; \tag{2.14}$$

and in the signed-λ basis is as follows:

$$H_{so} = \left|\begin{array}{c||ccccccccc} (\lambda,\sigma) & 1,1 & 1,0 & 1,-1 & 0,1 & 0,0 & 0,-1 & -1,1 & -1,0 & -1,-1 \\ \hline\hline 1,1 & -B & 0 & 0 & 0 & 0 & 0 & 0 & 0 & 0 \\ 1,0 & 0 & 0 & 0 & A & 0 & 0 & 0 & 0 & 0 \\ 1,-1 & 0 & 0 & B & 0 & A & 0 & 0 & 0 & 0 \\ 0,1 & 0 & A & 0 & 0 & 0 & 0 & 0 & 0 & 0 \\ 0,0 & 0 & 0 & A & 0 & 0 & 0 & A & 0 & 0 \\ 0,-1 & 0 & 0 & 0 & 0 & 0 & 0 & 0 & A & 0 \\ -1,1 & 0 & 0 & 0 & 0 & A & 0 & B & 0 & 0 \\ -1,0 & 0 & 0 & 0 & 0 & 0 & A & 0 & 0 & 0 \\ -1,-1 & 0 & 0 & 0 & 0 & 0 & 0 & 0 & 0 & -B \end{array}\right| . \tag{2.15}$$

In this study, we have calculated the spin-orbit terms A and B for the entrance channel of the reaction by *ab initio* methods. In the following subsections, the method of calculation, computational details and results are presented.

2.4.2 Method

Solution of the Dirac (relativistic) equation is the most rigorous way of calculating the spin-orbit couplings. However, solving the four-component Dirac equation is a formidable task. Instead, one can solve the spin part of the Breit-Pauli operator [84] and introduce the spin-orbit coupling as a perturbation to the electronic Hamiltonian. This is the approach we followed in this thesis. It is important to use a good approximation method because we calculate the couplings for the whole

surface.

The Breit-Pauli Hamiltonian in atomic units is [85]:

$$\mathbf{H}_{so} = \sum_{\alpha} \left[\sum_{i} \hat{h}_{\alpha}(i) \cdot \hat{s}_{\alpha}(i) + \sum_{i \neq j} \hat{g}_{\alpha}(i,j) \cdot \hat{s}_{\alpha}(i) \right], \tag{2.16}$$

where the one-electron (*spin-same-orbit*) spin-orbit operator, $\hat{h}_{\alpha}(i)$, is constructed by a sum over all the nuclei

$$\hat{h}_{\alpha}(i) = \frac{1}{2c^2} \sum_{A} \frac{Z_A (\vec{r}_{iA} \times \vec{p}(i))_{\alpha}}{r_{iA}^3}, \tag{2.17}$$

and two-electron (*spin-other-orbit*) spin-orbit operator, $\hat{g}_{\alpha}(i,j)$, is defined as

$$\hat{g}_{\alpha}(i,j) = -\frac{1}{2c^2} \left[2 \frac{(\vec{r}_{ij} \times \vec{p}(j))_{\alpha}}{r_{ij}^3} + \frac{(\vec{r}_{ji} \times \vec{p}(i))_{\alpha}}{r_{ij}^3} \right]. \tag{2.18}$$

i and j are the labels for the electrons and $\alpha = x, y, z$.

The spin-orbit operator is evaluated in the electronic basis formed by the nonrelativistic contracted CI wave functions in a first-order perturbation theory approach, as implemented in the MOLPRO package [42]. Current implementation allows the evaluation of the full Breit-Pauli operator for the internal configurations, whereas the contributions of the external configurations are calculated by a one-electron mean-field Fock operator. (causing errors no larger than 1 cm^{-1}).

2.4.3 Computational Details

In order to investigate the basis set and active space dependence of the spin-orbit coupling terms, first we have performed a set of calculations for the oxygen atom. Table 2.3 lists the results of the calculations and the experimental spin-orbit coupling constant. Because of technical limitations in MOLPRO, the maximum

Table 2.3: Effect of active space and the size of the basis set on the spin-orbit constant (cm^{-1}) for O(^3P)

Basis	MRCI ($2s2p$)	MRCI ($1s2s2p$)	Exp.
cc-pVTZ(f)	-74.84	-75.20	–
cc-pVQZ(f)	-75.98	-76.46	–
cc-pV5Z (f)	-76.68	-77.26	–
–	–	–	-77.40

angular momentum functions included were restricted to $l_{max} = 3$ (f functions). The absence of g functions is not in general a source of error for the second row elements [86]. MOLPRO requires the use of uncontracted basis functions in spin-orbit coupling calculations. The experimental value in the table corresponds only to the spin-orbit coupling constant of the oxygen atom. Other effects such as spin-spin coupling and spin-orbit coupling involving higher electronic states are excluded [85, 87]. We see from the table that correlation of the inner shell as well as a bigger basis improve the results. Because of the uncontracted basis functions and two electron terms spin-orbit calculations are computationally expensive. Therefore, based on this investigation, we used cc-pV5Z(f) basis and correlated all the electrons except the 1σ orbital. (For further information about the details of the calculation of the spin-orbit matrix elements and the dependency of the matrix elements on the correlation methods and basis sets, consult Ref. [85]).

We also investigated the behavior of the spin-orbit elements as a function of the Jacobi angle, θ. Table 2.4 shows the angular dependence of spin-orbit term A. We calculated the spin-orbit matrix in the adiabatic basis. It is possible to obtain

Table 2.4: Spin-orbit term A (cm^{-1}) as a function of Jacobi angle θ^o and R for a fixed value of $r = 1.402$ a.u.

θ	R/a.u.		
	10	7	3
0	−76.08	−76.04	−67.32
18	−76.04	−76.02	−69.04
36	−76.04	−76.04	−72.09
54	−76.05	−76.04	−73.48
72	−76.04	−76.04	−73.25
90	−76.13	−76.11	−73.23

the diabatic mixing angle from the spin-orbit coupling matrix itself [88]. Then by a unitary transformation, we acquired the angular dependence of the matrix elements in the diabatic basis. The angular dependence is the strongest when the species are close ($R \sim 3$ a. u.). However, at those geometries the electronic surfaces are farther apart and the coupling tends to be less important. The angular dependence of the term B is similar. As shown in the table and as concluded in the earlier work [68, 80], the angular dependence found to be overall quite weak, therefore we have concluded that the including only R and r as the geometry parameters would be enough in the spin-orbit calculations.

2.5 Results

Figure 2.9 shows the splined surfaces for the spin-orbit coupling coefficients, A and B, in the entrance channel of the reaction O+H_2 as a function of Jacobi coordinates R and r. As clearly seen in the figure, in the Van der Waals region A

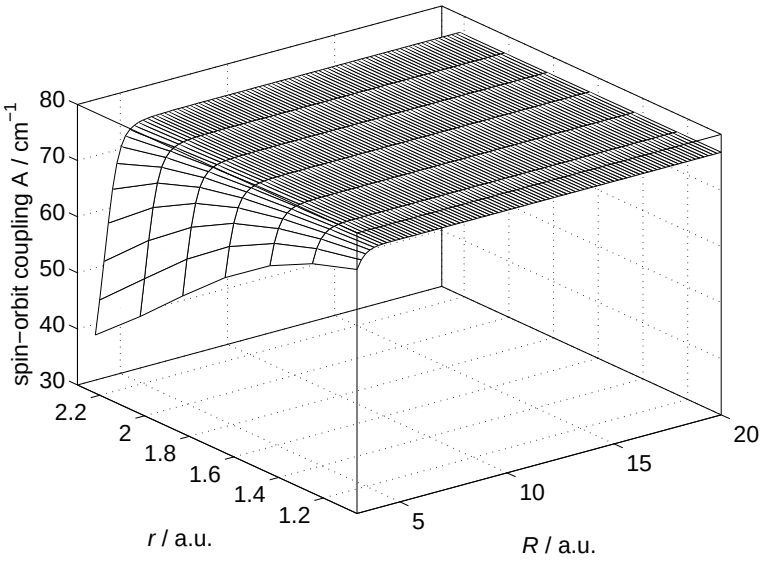

(a) Spin-orbit coupling term $\mathrm{A}(R,r)=\langle \Pi_x |\, H_{so}\, | \Sigma \rangle$.

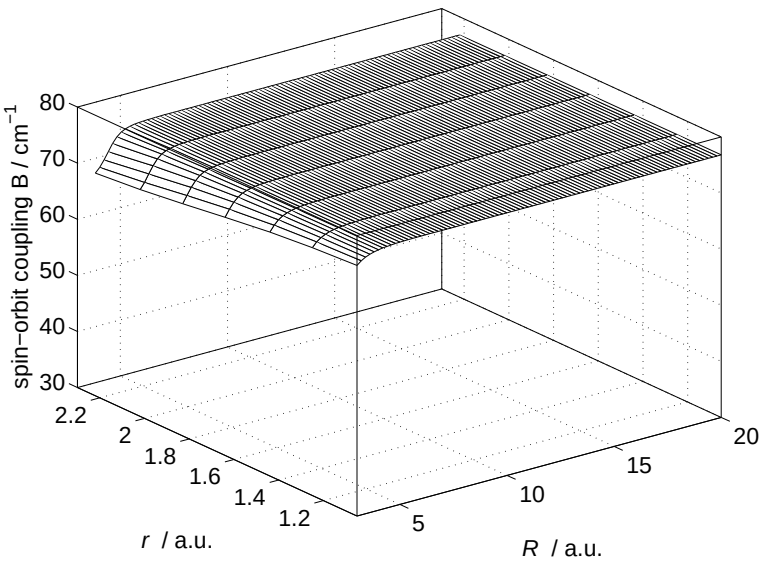

(b) Spin-orbit coupling term $\mathrm{B}(R,r)=i\,\langle \Pi_x |\, H_{so}\, | \Pi_y \rangle$.

Figure 2.9: Spin-orbit coupling terms in the entrance channel of the O+H_2 reaction.

and B are independent of geometry. In the range of large R, they both converge to the spin-orbit coupling constant of the oxygen atom. For $R < 5$, changes starts to take place. Both A and B decreases as R gets smaller. The coupling term A drops significantly in this region (close to barrier) where OH bond starts to form.

For the O+H_2 reaction, the barrier geometry is reported to be collinear ($\theta = 0$) and at the coordinates $R_b = 2.30$ a.u., $r_b = 1.71$ a.u. [20], where the subscript "b" denotes the position of the barrier. Our calculation at this geometry revealed that the spin-orbit coupling term B is still nearly independent of R, ($B(R_b, r_b) = 69.6$ cm^{-1}), while A has droped dramatically, ($A(R_b, r_b) = 26.7$ cm^{-1}). Thus, inclusion of the spin-orbit term in the Hamiltonian will change the barrier height (approximately 40 cm^{-1}). However, since the barrier is reported to be quite high for the title reaction (approximately 13.2 kcal/mol = 4620 cm^{-1}, [19, 20]), the effect of the spin-orbit coupling is insignificant (approximately 1.5 %). Figure 2.10 shows a cross section of the spin-orbit surfaces along the coordinates R (a) and r (b) indicating the *ab initio* data points. The corresponding data points are listed in Appendix A.2.

Maiti and Schatz [32] obtained spin-orbit coupling terms for the reaction when they looked at the intersystem crossings for the $O(^3P,^1D)$ + H_2 system. They predicted the reagents fine structure splittings as $\Delta E(^3P_1 - ^3P_2)$ and $\Delta E(^3P_0 - ^3P_2)$ of 70 cm^{-1} and 148.6 cm^{-1} respectively. This would correspond to a coupling value in the range of 35 to 50 cm^{-1} which is much less accurate then our results.

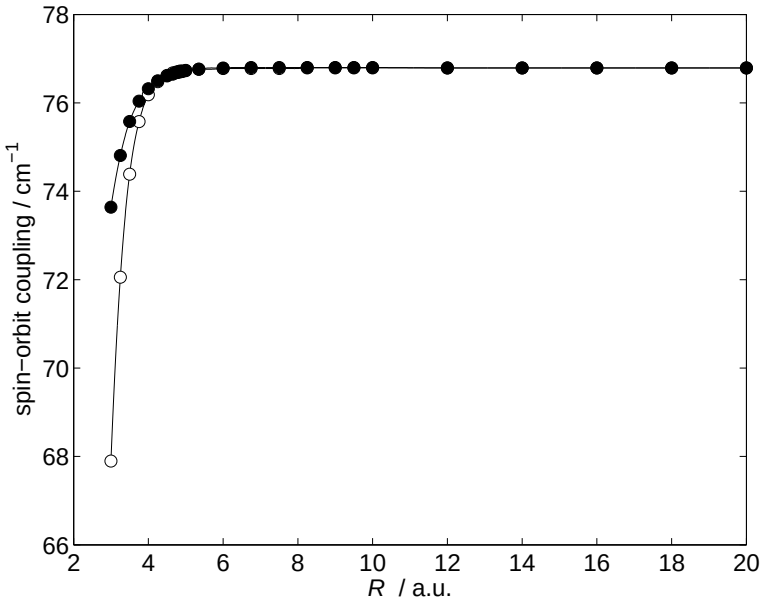

(a) $r = 1.402$ a.u. and $\theta = 0$

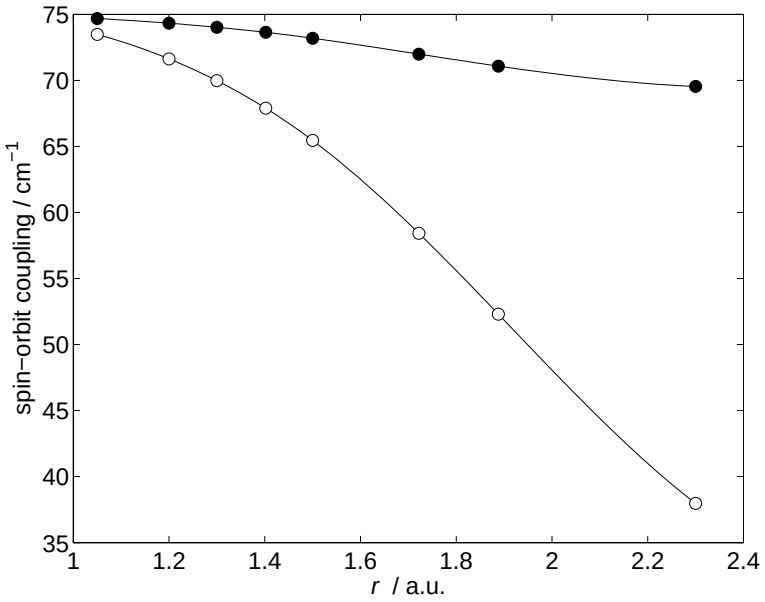

(b) $R = 3.0$ a.u. and $\theta = 0$

Figure 2.10: Spin-orbit coupling terms in the entrance channel of the O+H_2 reaction as a function of Jacobi coordinates R and r. The unfilled and filled circles indicate the data points for terms A and B, respectively.

2.6 Summary

In this chapter, we reported PESs for the $O(^3P)-H_2$ system determined by RCCSD(T) and MRCI calculations as well as the spin-orbit coupling terms calculated by the *ab initio* implementation of the Breit-Pauli Hamiltonian.

We assessed the accuracy of the MRCI+Q results extrapolated to the CBS limit in comparison to RCCSD(T) calculation with an aug-cc-pVQZ basis with additional bond functions. The results showed very good agreement. Based on these results we predict the van der Waals minimum to be in perpendicular geometry, and located at a closer distance than a secondary well in collinear geometry. Our calculation corroborates the earlier results of Alexander [23], however, disagrees with earlier report of Li [22] as well as with recently refitted surfaces of Brandão and coworkers [21]. Our RCCSD(T) calculations with an aug-cc-pVQZ basis including a set of bond functions are expected to recover as much of dispersion energy, which is responsible for the van der Waals minima, as calculations with much larger purely nuclear-centered orbital bases. Therefore, we have confidence in the geometries and well depths predicted.

Spin-orbit coupling terms for the $O(^3P)-H_2$ system are reported. We found the angular dependence of the coupling terms negligible. The geometry dependence in the van der Waals region is very weak. However, a high accuracy description of the barrier requires the calculation of spin-orbit coupling terms.

Chapter 3

Introduction to Scattering Dynamics in the Presence of Long-lived Reaction Complexes

3.1 Introduction

Radical-radical reactions typically have one or more deep wells in the PES which facilitate complex formation and slow decomposition into products. In an exact quantum mechanical treatment, because all states in this well which are energetically accessible must be included, the solution of a large number of coupled equations is inevitable. If quantum mechanical effects are negligible, we can treat the system purely classically. The third approach, which is the method applied in this thesis, is a statistical approach.

The development and the application of statistical theories to chemical reaction dynamics in 1960s coincides with the time that the computers were first applied to reaction dynamics. Although more than 40 years has elapsed, the exact quantum treatment of the dynamics of complex forming reactions is still a demanding task. In search of better statistical methods, recent years have seen the development of time independent [89, 90] and time dependent [91, 92] formulations of complex forming reactions, which are free of many approximations which were used in the past. Although exact quantum mechanical calculations are possible, [93] it is com-

putationally expensive to determine state-to-state cross sections over a large grid of energies. This information is necessary to calculate thermal rate constants, which are vital for the modeling of realistic chemical problems. Thus, the development of more accurate statistical models is a promising advance in scattering dynamics.

Rackham and coworkers successfully unified [89, 90, 94] a venerable statistical model, developed first by Pechukas and Light, [95] with the close-coupled capture theory of Clary and Henshaw [96]. This chapter of the thesis is dedicated to the introduction of this formalism, which has been recently applied to insertion reactions such as $O(^1D)$ + H_2 and $C(^1D)$ + H_2 with accuracy comparable to exact quantum mechanical calculations.

In comparison with exact quantum scattering calculations on the $O(^1D)$+$H_2 \rightarrow$ OH+H reaction, [93] in which a single PES was used, the close-coupled, statistical model, [89, 90] in both the full close-coupled and the computationally simpler, coupled-states (CS) approximation [97, 98], yielded excellent agreement for both integral and differential state-resolved cross sections. Alexander, Rackham and Manolopoulos (ARM) [94] have extended the close-coupled, statistical model to include the electronic degrees of freedom (orbital and spin angular momenta) of the OH and H fragments. This necessitates inclusion of the four PESs ($^{1,3}A'$ and $^{1,3}A$") which correlate with $OH(X^2\Pi)$+$H(^2S)$.

The topics of the following two chapters, the isotope exchange reaction of D+OH→OD+H and the vibrational dynamics of collisions of OH with atomic hydrogen both involve complex formation ($H_2O^\dagger$ and $HOD^\dagger$) and thus can be treated *semi-statistically*, in which capture probabilities from each channel into the com-

plex region are calculated separately by regular time-independent scattering theory methods, and then connected according to statistical considerations.

3.2 Coupled-Channel Statistical Theory

The exact quantum mechanical treatment of insertion reactions involving deep wells is complicated by the necessity of using large basis sets to describe all the bound and quasi-bound states accessed in these wells [93]. The statistical model assumes [99] that the complex spends enough time in the well to scramble all direct connection between reactants and products and that reactive scattering occurs only through complex formation. Hence, if one can get the capture probabilities from each channel accurately, then it is possible to connect those channels by probabilistic ideas without a significant loss of accuracy.

In the close-coupled statistical model, all coupling within the various arrangement channels is included, but separately for each arrangement, to determine exact capture probabilities. Total angular momentum, J, and the total energy, E, are the conserved quantities in the reaction. The capture probabilities are then combined, following the statistical prescription, [95, 100] to yield the state-to-state probability for reaction from state n to product state n'

$$P^J_{nn'}(E) = \frac{P^J_n(E)P^J_{n'}(E)}{\sum\limits_{n''} P^J_{n''}(E)}. \tag{3.1}$$

For simplicity we use the single index n to designate the complete set of quantum numbers, i. e. $\{v, j, F_i, \epsilon, \sigma_h\}$. P_n and $P_{n'}$ are the respective capture probabilities in the reactant and product arrangement for a total energy, E and total angular

momentum, J, and the sum in the denominator runs over both arrangements. The state-to-state probability $P^J_{n'n}(E)$, is the product of the capture probability from the reactant state n ($P^J_n(E)$), with the fraction of complexes that decay into the product channel n'. The capture from a particular channel is the same as the decay into it by detailed balance; so the fraction of complexes that decay into the channel n' is $P^J_{n'}(E)/\sum_{n''} P^J_{n''}(E)$. Hence, the state-to-state reaction probability in Eq. 3.1 is obtained.

Rackham, Manolopoulos and co-workers used a time-independent formalism to determine the capture probabilities. In the time-independent inelastic scattering theory [101–103], the time-independent Schrödinger equation

$$\mathbf{H}\Psi = E\Psi \tag{3.2}$$

is solved by expanding the total wave function in a set of basis functions representative of the triatomic system with subsequent matching of the propagated solution to an asymptotic form. The S-matrix contains all transition amplitudes between all initial, $|n\rangle$, and final, $|n'\rangle$, states. Unlike conventional inelastic scattering theory, the S-matrix, although symmetric, is, no longer unitary [89]. The initial condition for the propagation is a WKB approximation to a purely incoming wave function at a point well inside the complex region, as illustrated in Fig. 3.1. This capture boundary condition acts like a sink, thus the S-matrix is not unitary. The size of the complex, which is set by the capture radius, R_c, is the key parameter. This is reduced until the calculated cross sections converge. The capture probability from

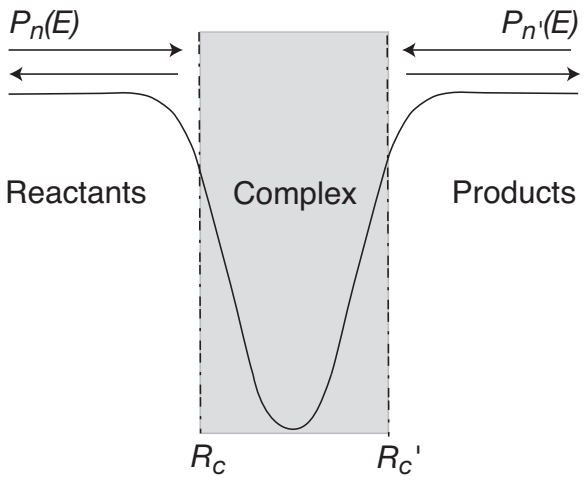

Figure 3.1: Illustration of a complex-forming reaction described by the statistical model [104]. The complex region (shaded) is delimited by a capture radius, R_c. The capture probabilities for both the reactant and products are obtained by solving coupled scattering equations outside of this capture radius.

any initial state n is readily obtained by

$$P_n^{J,capture}(E) = 1 - \sum_{n'} \left| S_{nn'}^J(E) \right|^2 . \tag{3.3}$$

In every collision, there is also the possibility of direct scattering because of the existence of repulsive regions on the PESs. So inelastic transitions can occur even without penetration into the complex. For these processes, the transition probabilities are given, as in conventional inelastic scattering theory by the square of a S-matrix element. We define the direct scattering probability for the $n \rightarrow n'$ transition as

$$P_{nn'}^{J,direct}(E) = \left| S_{nn'}^J(E) \right|^2 . \tag{3.4}$$

In comparison, exact quantum scattering calculations on the $O(^1D)$+H_2 $\rightarrow$

OH+H reaction, [93] in which a single ground state PES was used, the close-coupled, statistical model, in both the full close-coupled (CC) and the computationally simpler, coupled-states (CS) approximation, [89, 90] yielded excellent agreement for both integral and differential state-resolved cross sections. In the CS approximation, apart from the total energy and the total angular momentum, the projection of the total angular momentum along $\vec{R}$, K, is conserved. The coupling matrix is block diagonalized for different projections of the total angular momentum. This substantially decreases the computational workload. For this reason, we adopt the the CS approximation in our calculations, since we are interested in thermal rate constants, which require summing over a large set of energies. In the rest of the chapter, we present the PESs, Hamiltonian and Basis, frame of references, propagation methods, and calculation of S-matrix and implementation to obtain the cross sections for which some brief introduction has been given above.

3.2.1 *Ab Initio* Potential Energy Surfaces (PESs)

The interaction of H and OH($^2\Pi$) is governed by four PESs, as shown schematically in Fig. 3.2. The doublet H and OH fragments can be spin paired to yield states of singlet or triplet multiplicity. The orbital degeneracy of the OH fragment gives rise to states of Π symmetry in linear geometry, or A' and A'' reflection symmetry in non-linear geometry. The $^1A'$ state corresponds to the ground state of the H_2O molecule, and the corresponding PES has a deep well. The three other states, $^1A''$, $^3A'$ and $^3A''$, do not allow covalent bonding between the H and OH. Hence,

the corresponding PESs are repulsive. Because all four PESs coalesce to the same asymptotic limit, it is necessary to include all four PESs.

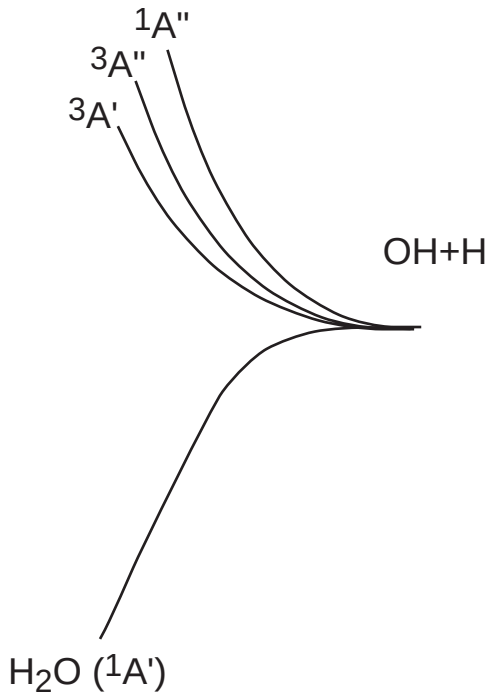

Figure 3.2: Schematic illustration of the OH + H potential energy surfaces.

Due to its importance in the combustion processes, interaction potentials for the reaction of $O(^1D,^3P)$ + H_2 to yield $OH(^2\Pi)$ is well studied. Global fits to the interaction potentials of $^{1,3}A'$ and of $^{1,3}A''$ states are already available [20, 88]. However, global fits often fall short in describing the long range interaction, which is essential in the statistical capture calculations. Therefore, as reported by Alexander *et al.* [94] the PESs for the $OH(^2\Pi)$+H channel were redone by internally-contracted, multi-reference, configuration-interaction calculations [105, 106] using Dunning's *avqz* atomic orbital basis sets [76]. The potential energies were determined [94] on a grid of points in Jacobi coordinates appropriate to the OH+H system, namely

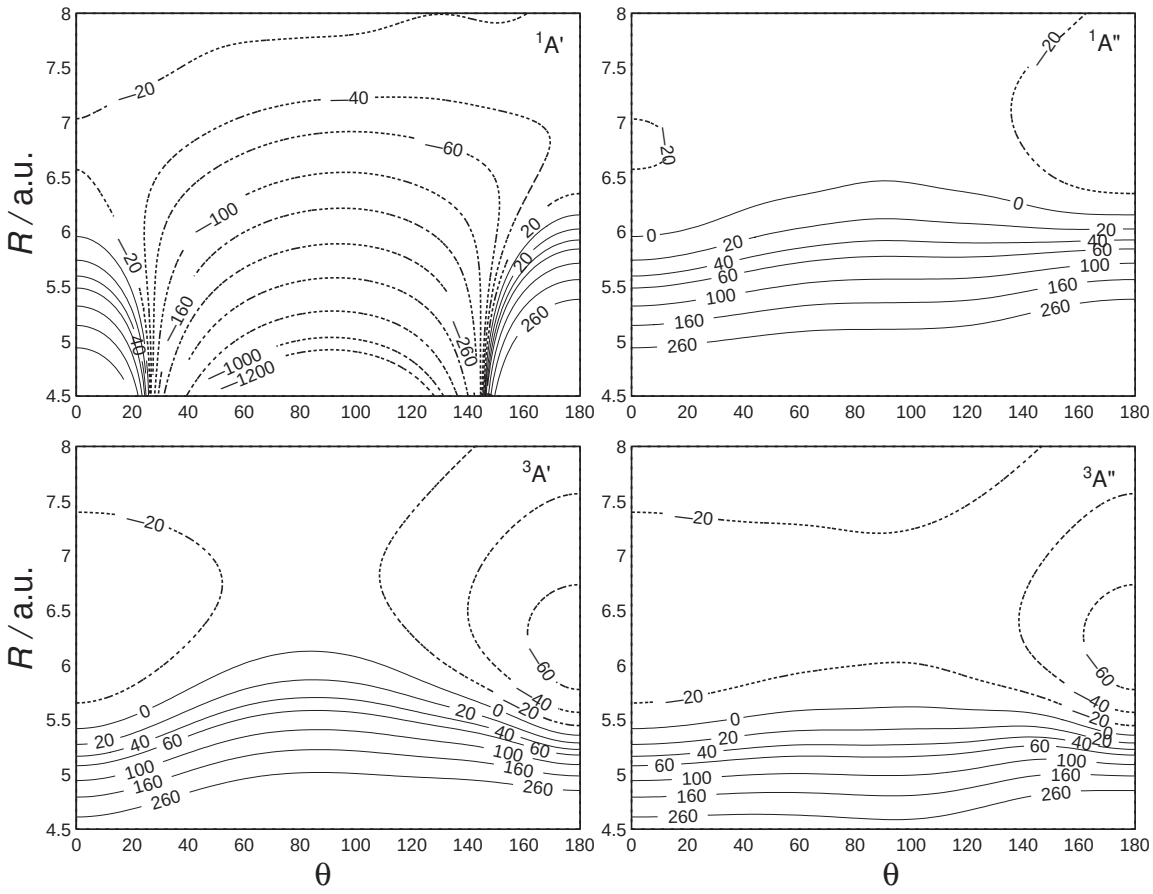

Figure 3.3: Contour plots (cm^{-1}) of the OH-H PESs as a function of Jacobi coordinates R and θ for a fixed OH distance of 1.8324 a.u.

R, the distance between the H atom and the center-of-mass of the OH molecule; r, the OH bond distance; and θ, the angle between $\vec{R}$ and $\vec{r}$. These *ab initio* points were then fitted to an appropriate functional form. The average rms deviation for the fit to all four surfaces was 1.2 cm^{-1}. The scattering calculations in this thesis are done on the ARM surfaces which govern both OH + H and OH + D collisions.

Surfaces, except $^1A'$, are all repulsive as indicated earlier, however a van der Waals minimum exists in the colinear arrangement on the repulsive surfaces.

3.2.2 Hamiltonian and Basis

The quantum mechanical description of triatomic collisions involving open-shell molecules is similar to that of closed-shell molecules, in that the total wave-function is expanded in a set of products of functions describing the internal motion of the diatomic moiety. The expansion coefficients are function of the Jacobi separation vector. (The Jacobi coordinates for a triatomic system are defined earlier in Eq. 1.3-1.5.) In the case of an open-shell molecule, the Hamiltonian for the internal motion includes both the usual vibrational and rotational motion as well as spin-orbit and Λ-doubling terms [107]. The present study is based on the framework laid by Alexander and coworkers [94].

To set the framework, let us assume an OH($^2\Pi$) + H encounter. Then the Hamiltonian is

$$\mathbf{V}_{\mathrm{OH+H}}(\vec{R},\vec{r},\vec{q}) = \mathbf{T}_n(\vec{R}) + \mathbf{V}_{el}(\vec{q};\vec{R},\vec{r}) + \mathbf{H}_{mol,\mathrm{OH}}(\vec{q};\vec{r}), \tag{3.5}$$

Here $\vec{R}$ and $\vec{r}$ are the Jacobi coordinates for a particular arrangement, and $\vec{q}$ repre-

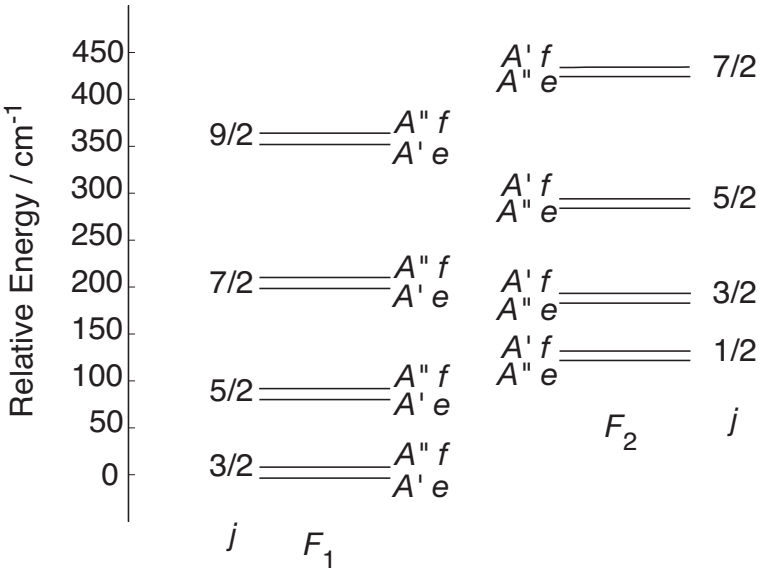

Figure 3.4: Positions of the lower spin-rotation levels of OH($X^2\Pi$). For clarity, the magnitude of the Λ-doublet splitting has been greatly exaggerated.

sents the electronic coordinates. The first term $\mathbf{T}_n$ represents the kinetic energy of the relative atom-diatom motion:

$$\mathbf{T}_n = -\frac{\hbar^2}{2\mu R^2}\frac{\partial}{\partial R}R^2\frac{\partial}{\partial R} + \frac{\mathbf{L}^2}{2\mu R^2}. \tag{3.6}$$

The second term in Eq. (3.5), $\mathbf{V}_{el}$, is the Hamiltonian for the electronic interaction,

$$\mathbf{V}_{el} = V(\vec{R}, \vec{r}; \vec{q}), \tag{3.7}$$

and the third term in Eq. (3.5), $\mathbf{H}_{mol}$, is the molecular hamiltonian for the diatom. The *ab initio* determination of $\mathbf{V}_{el}$ leads to four PESs introduced earlier in section 3.2.1. The theory of the *free* OH/OD diatom is explained in detail in Appendix B.

As illustrated schematically in Fig. 3.4, there exist two rotational ladders, F_1 and F_2, separated by the spin-orbit splitting. In addition, for each value of the OH

rotational angular momentum, there exist two Λ-doublet levels, separated by only a fraction of a wavenumber. In the high-J limit, the two Λ-doublet levels can be distinguished by the reflection symmetry of the spatial component of the electronic wavefunction in the plane of rotation of the diatomic [108, 109]. In the lower (F_1) spin-orbit manifold, the levels of nominal A' reflection symmetry are conventionally labelled e and the levels of nominal A'' reflection symmetry, f. This e/f labelling is reversed in the upper (F_2) spin-orbit manifold. Note that the A' Λ-doublet levels are lower in energy in the F_1 spin-orbit manifold, but higher in energy in the F_2 spin-orbit manifold. This situation is reversed in the F_2 spin-orbit manifold for levels with $j \geq 9/2$. Thus, except for the F_2 levels with $1/2 \leq j \leq 7/2$, the lower of the two Λ-doublet levels always corresponds to nominal A' reflection symmetry.

Now we have the appropriate basis for the diatom and H_{mol} in this basis, we can proceed to the solution of the triatomic scattering process. The overall wavefunction for the OH-H system is expanded in the basis

$$\begin{aligned} \Phi_n^J(\hat{R}, \vec{r}) &= \langle \hat{R}, \vec{r} | JMKvjk\lambda\sigma\sigma_h \rangle \\ &= \frac{1}{r} \hat{D}_{MK}^{J*}(\phi, \theta, 0) \hat{d}_{k\omega}^{j}(\gamma) \chi_{vj}(r) |\lambda\sigma\rangle |\sigma_h\rangle. \end{aligned} \tag{3.8}$$

Here, J is the total angular momentum with projection K along OH-H vector $\vec{R}$ and M along the space-frame z-axis. The quantum number j designates the rotational angular momentum of OH diatom, with projection k along $\vec{R}$ and with projection w along $\vec{r}$. $\hat{D}_{MK}^{J*}(\Omega) = ([2j+1]/8\pi^2)^{1/2} D_{MK}^{J*}(\Omega)$ is the normalized Wigner rotation matrix element, where Ω designate the three Euler angles that relate the space-fixed and body-fixed axis frames. χ is the OH vibrational wavefunction. The ket $|\lambda\sigma\rangle$

designates the electronic wavefunction of the OH molecule, where λ and σ are the projections of the electronic orbital and spin angular momenta along $\vec{r}$ and $\omega = \lambda + \sigma$. The second ket $|\sigma_h\rangle$ designates the electronic wavefunction of the H atom, where σ_h is the projection of the H-atom spin along $\vec{R}$. The total projection of the total angular momenta J along $\vec{R}$ is $K = k + \sigma_h$.

Although, this basis is a better choice for the propagation of the radial coefficients, the ideal choice of the asymptotic form of the wave function would be the one in which H_{mol} is diagonal, which is

$$\begin{aligned} \Phi^J_m(\hat{R}, \vec{r}) &= \langle \hat{R}, \vec{r} | JMKvjkF_i\epsilon\sigma_h \rangle \\ &= \frac{1}{r}\hat{D}^{J*}_{MK}(\phi, \theta, 0)\hat{d}^j_{k\omega}(\gamma)\chi_{vj}(r)F_i\epsilon\rangle|\sigma_h\rangle. \end{aligned} \tag{3.9}$$

Therefore, the coupled equations are solved in basis (3.8) and then the solution is transformed into basis (3.9) at the end of the propagation.

At each value of R, the total wave function is expanded as

$$\Psi^J_n(\vec{R}, \vec{r}) = \frac{1}{R}\sum_m \Phi^J_m(\hat{R}, \vec{r})\Psi^J_{mn}(R). \tag{3.10}$$

Applying the total Hamiltonian operator given in Eq. (3.5), multiplying with $\Phi^{J*}_{n'}(\hat{R}, \vec{r})$ on the left and integrating over all angles and $\vec{r}$, we obtain the following coupled equations to be solved:

$$\left[\frac{d^2}{dR^2} - \frac{J(J+1) + j(j+1) + \frac{3}{4} - 2K^2 + 2k\sigma_h}{R^2} + \frac{2\mu}{\hbar^2}(E - E_{n'})\right]\Psi^J_{n'n}(R) = \frac{2\mu}{\hbar^2}\sum_m V^{Jk}_{n'm}\Psi^J_{mn}(R) \tag{3.11}$$

where L^2_{op} is replaced with $J(J+1) + j(j+1) + \frac{3}{4} - 2K^2 + 2k\sigma_h$ and the off diagonal coupling between different values of k are assumed to be zero according to the

coupled states (CS) approximation [97, 98]. This significantly reduces the size of the coupled channels. Here n is a channel label for $|JMKvjk\lambda\sigma\sigma_h>$.

This set of coupled equations can be written in matrix form as

$$\frac{d^2}{dR^2}\Psi(R) = W(R)\Psi(R), \tag{3.12}$$

The log-derivative [102, 110] propagation employed in the matrix Riccati form:

$$Y'(R) = W(R) - Y(R)^2, \tag{3.13}$$

where $Y(R) = \Psi'(R)\Psi(R)^{-1}$

The main difference between the regular close-coupled scattering calculations and the present capture calculations are the capture boundary conditions. Capture boundary condition unlike the usual inelastic scattering calculations allow for a nonvanishing incoming wave for each adiabatic state which is not energetically closed at the capture radius R_c [89, 90]. R_c is chosen to be well within the complex forming region. The best choice of initial condition is an Airy function boundary condition [104]. The log-derivative matrix, Y, is propagated outward and the S-matrix is extracted using the standard formula:

$$S^J(E) = \left[Y(R_a)O(R_a) - O'(R_a)\right]^{-1}\left[Y(R_a)I(R_a) - I'(R_a)\right], \tag{3.14}$$

where O and I are the following incoming and outgoing Riccati-Hankel functions:

$$I_{vjl}(R) = k_{vj}^{-1/2}\hat{h}_l^-(k_{vj}R) \tag{3.15}$$

$$O_{vjl}(R) = k_{vj}^{-1/2}\hat{h}_l^+(k_{vj}R). \tag{3.16}$$

The S-matrix, although symmetric, is, however, no longer unitary since the capture boundary condition acts like a sink.

As discussed earlier, [89, 90] the computationally more efficient coupled-states approximation [97, 98] can be used, wherein both the total angular momentum J and its projection K along $\vec{R}$ are conserved. At a given value of the total energy E and the quantum numbers J and K, the probability of capture for an OH+D collision in which the initial state of diatomic moiety and the spin state of the atom is described by n is

$$P_n^{JK}(E) = 1 - \sum_{n'} \left| S_{nn'}^{JK}(E) \right|^2 . \tag{3.17}$$

Here the sum is over all energetically accessible states. In reality the single index n designates the set of quantum numbers $\{v, j, k, F_i, \varepsilon, \sigma_h\}$. If we insert, explicitly, all the relevant quantum numbers, in analogy to 3.1, the probability of a $n \rightarrow n'$ capture transition becomes:

$$P^{J,capture}_{vjF_i\varepsilon\sigma_h \rightarrow v'j'F_i'\varepsilon'\sigma_h'}(E) = \sum_{KK'} \frac{P^{JK}_{vjF_i\varepsilon\sigma_h}(E) P^{JK'}_{v'j'F_i'\varepsilon'\sigma_h'}(E)}{\sum\limits_{K''v''j''F_i''\varepsilon''\sigma_h''} P^{JK''}_{v''j''F_i''\varepsilon''\sigma_h''}(E)}. \tag{3.18}$$

Within the coupled-states approximation the projection K of the total angular momentum along in the Jacobi vector of relative motion is conserved within each arrangement, and is thus a good quantum number. However, presumably, this is scrambled within the complex, so that there appear $K \rightarrow K'$ contributions in Eq. (3.18).

The transition probability for an inelastic $n \rightarrow n'$ transition, due to coupling before capture is given by

$$P^{JK,direct}_{vjF_i\varepsilon\sigma_h \rightarrow v'j'F_i'\varepsilon'\sigma_h'} = \left| S^{JK}_{vjF_i\varepsilon\sigma_h \rightarrow v'j'F_i'\varepsilon'\sigma_h'}(E) \right|^2 . \tag{3.19}$$

Since only the initial arrangement is responsible for the direct contribution, K is conserved in the inelastic scattering contribution.

Once the state-to-state capture probabilities are known, the integral cross sections are readily obtained. Our investigation of OH+D and OH+H collisions based on the statistical capture theory is presented in the following two chapters.

Chapter 4

Cross Sections and Thermal Rate Constants for the Isotope Exchange Reaction: $D(^2S) + OH(^2\Pi) \rightarrow OD(^2\Pi) + H(^2S)$

4.1 Introduction

The isotope exchange reaction of OH with deuterium atoms is a major source of OD in interstellar clouds [34]. The relative OH/OD abundance in the interstellar medium (ISM) depends on chemical fractionation mechanisms (in particular isotopic fractionation) and can be utilized to uncover the importance of various chemical processes occuring in the ISM [111]. Accurate rate constants for proton/deuteron exchange are a crucial requirement for the modeling of the chemistry in the ISM.

With no activation barrier, the title reaction is one of the few neutral-neutral reactions which will occur efficiently at interstellar temperatures, which typically range from 10 K to 100 K. Because of the difference in zero-point energies, [112] this reaction is exothermic by 717 K (499 cm^{-1}). The barrierless [113] reaction proceeds on the potential energy surface of the electronic ground state of the water molecule ($^1A_1$) as shown schematically in Fig. 4.1. The title reaction involves the interconversion of the two exit channels of the barrierless $O(^1D)$+H_2 insertion reaction.

There have been only a few theoretical and experimental determinations of

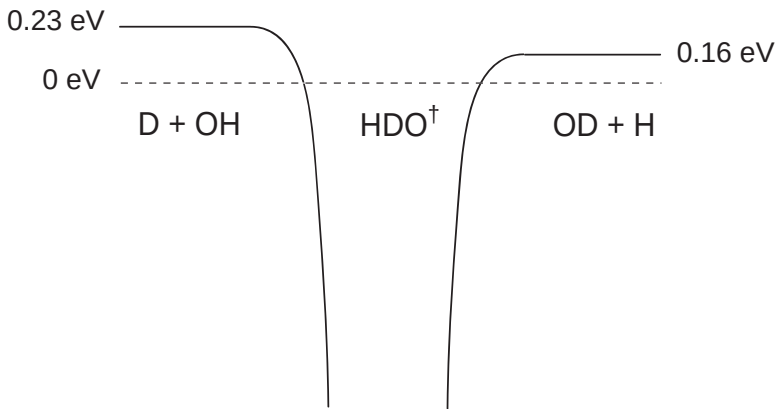

Figure 4.1: Schematic illustration of the reaction path for $D(^2S)$ + $OH(^2\Pi)$ → $HDO^\dagger$ → $OD(^2\Pi)$ + $H(^2S)$. The zero of energy corresponds to D+OH ($r = r_e$) and is identical for the OD+H arrangement. The vibrational zero-point energies of the diatomic fragment in each arrangement are also indicated.

cross sections and rate constants for the title reaction. Table 4.1 summarizes these. The degree of disagreement seen here was a stimulus for the present investigation.

Kaufman and co-workers reported the first experimental determination of the rate coefficient of the title reaction [116]. A more recent measurement by Howard and Smith [114] yielded a considerably smaller value. The latter authors also reported a negative temperature dependence of the rate constant, which they attributed to the increase in the probability of complex formation with decreasing temperature. Howard and Smith also report rate predictions based on a simple early version of the Statistical Adiabatic Channel Model (SACM) of Quack and Troe [117, 118] and an empirical crude potential energy surface. The SACM estimates of the rate constant fell between the measurements of Howard and Smith and those of Margitan at $T =$ 300 K (See Table 4.1).

Table 4.1: Summary of reported rate constants for D+OH reaction.

	$k_{v\to v'}$ / 10^{-11} cm^3 molecule^{-1} s^{-1}	
T / K	Theory	Experiment
50	15.31[a]	-
100	14.22[a]	-
300	10.78[a]	5.19 ± 0.31[b]
	9.4[c]	13 ± 3[d]
	10[e]	
500	9.65[a]	3.74 ± 0.20[b]
	10.4[c]	
	8[e]	

[a]This work.

[b]Theoretical; Reference [114].

[c]Experimental; Reference [115]. The statistical uncertainty in these quasiclassical trajetory calculations was estimated at ±20 %, which overshadows the small predicted temperature dependence.

[d]Experimental; Reference [116].

[e]Experimental; Reference [114]; theoretical estimates based on the adiabatic channel model of Quack and Troe (Refs. [117, 118]).

Dunne and Murrell [115] reported quasiclassical trajectory (QCT) determinations of the rate constant based on a parameterized potential energy surface for the electronic ground state of water. Their calculated rate constants are roughly twice as large as those of Howard and Smith [114] and, hence, at 300 K agree better with the earlier measurement of Kaufman and co-workers [116]. Day and Truhlar have reported [119] a quantum determination of thermal rate constants for the title reaction, but restricted solely to zero total angular momentum.

Recently, we have shown [94] how the statistical-close-coupled method of

Manolopoulos and co-workers [89, 90] can be successfully extended to treat the $O(^1D)+H_2 \rightarrow OH(X^2\Pi) + H$ reaction, with inclusion of all electronic degrees of freedom. A straightforward modification of this method will allow us to carry out a similar quantum-statistical treatment of the title reaction.

In Sec. 4.2 below we review briefly the relevant details of the statistical method, the Hamiltonian, the potential energy surfaces used, and the ensuing calculations. In Sec. 4.3, we present the calculated cross sections and thermal rate constants. In particular, we predict significant, non-statistical distributions of the product OD molecules among the energetically-accessible spin-orbit (fine-structure) and Λ-doublet levels. The temperature dependence of the rate coefficients is also discussed.

4.2 Theory and Computational Methods

The Coupled-channel statistical model and the relevant PESs are introduced earlier in Chapter 3. Here we apply the close-coupled, statistical method to the title reaction, with the modification that both the initial and final arrangements in Eq. (5.3) correspond to the two hydroxyl isomers (D+OH and OD+H). Because the $OH+H \rightarrow O(^1D)+H_2$ reaction in endoergic by 1.7 eV, the O+HD arrangement is not accessible at thermal energies. Similar to the work of ARM, [94] we report here CS capture calculations of cross sections and rate constants for the title reaction. Since full details of the statistical capture theory [89, 90] and the extension to nonadiabatic dynamics [94] have recently been published, we will present here only the most relevant methodological details.

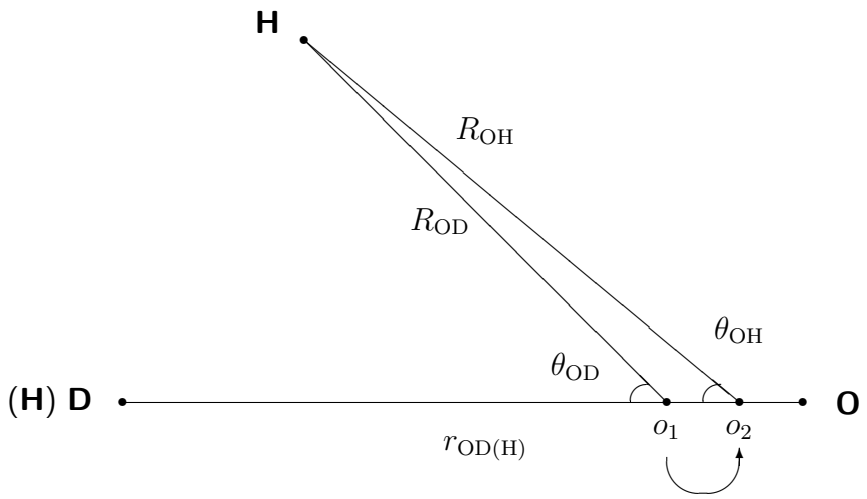

Figure 4.2: The effect on the H+OD Jacobi coordinates of the shift in the center-of-mass due to isotope exchange.

4.2.1 Coordinate Shift

For the close-coupled capture calculations, the wavefunction is expanded in Jacobi coordinates for each arrangement. For the OH+D arrangement, the Jacobi coordinates are identical to those for OH+H, so that the original fitted potential energy surfaces can be used. However, as illustrated in Fig. 4.2, for the OD+H arrangement, the shift of the position of the center-of-mass of the OD molecule engenders a slight change in the coordinates. By simple trigonometry one can show that in terms of the OD+H Jacobi coordinates, the OH+H Jacobi coordinates, in terms of which the potential energy surfaces are defined, are given by:

$$|o_2 - o_1| = r_{\mathrm{OD}} \, \frac{m_{\mathrm{O}}(m_{\mathrm{D}} - m_{\mathrm{H}})}{m_{\mathrm{OH}}} \tag{4.1}$$

$$R_{\mathrm{OH}}^2 = |o_2 - o_1|^2 + R_{\mathrm{OD}}^2 - 2R_{\mathrm{OD}}|o_2 - o_1| \cos(\pi - \theta_{\mathrm{OD}}) \tag{4.2}$$

$$\theta_{\mathrm{OH}} = \cos^{-1}\left(\frac{|o_2 - o_1|^2 + R_{\mathrm{OH}}^2 - R_{\mathrm{OD}}^2}{2R_{\mathrm{OH}}|o_2 - o_1|}\right), \qquad 0 < \theta_{\mathrm{OH}} < \pi \tag{4.3}$$

4.2.2 Hamiltonian and Basis

The quantum mechanical description of triatomic collisions involving open-shell molecules is similar to that of closed-shell molecules, in that the total wavefunction is expanded in a set of products of functions describing the internal motion of the diatomic moiety. The expansion coefficients are function of the Jacobi separation vector. In the case of an open-shell molecule, the Hamiltonian for the internal motion includes both the usual vibrational and rotational motion as well as spin-orbit and Λ-doubling terms [107]. The present study is based on the framework laid by Alexander and coworkers [94].

The capture probabilities for the OH+D and OD+H arrangements are determined in separate scattering calculations. In both arrangements the Hamiltonian is

$$\mathbf{H}_{\mathrm{OH(D)+D(H)}}(\vec{R},\vec{r},\vec{q}) = \mathbf{T}_n(\vec{R}) + \mathbf{V}_{el}(\vec{q};\vec{R},\vec{r}) + \mathbf{H}_{mol,\mathrm{OH(OD)}}(\vec{q};\vec{r}), \tag{4.4}$$

Here $\vec{R}$ and $\vec{r}$ are the Jacobi coordinates for a particular arrangement, and $\vec{q}$ represents the electronic coordinates. The first term $\mathbf{T}_n$ represents the kinetic energy of the relative atom-diatom motion:

$$\mathbf{T}_n = -\frac{\hbar^2}{2\mu R^2}\frac{\partial}{\partial R}R^2\frac{\partial}{\partial R} + \frac{L_{op}^2}{2\mu R^2}. \tag{4.5}$$

The second term in Eq. (4.4), $\mathbf{H}_{el}$, is the Hamiltonian for the electronic interaction,

$$\mathbf{H}_{el} = V(\vec{q};\vec{R},\vec{r}), \tag{4.6}$$

and the third term in Eq. (4.4), $\mathbf{H}_{mol}$, is the OH (OD) molecular hamiltonian.

The overall wavefunction for the OH–D (OD–H) system is expanded in the

basis

$$\langle \hat{R}, \vec{r} | JMKvjk\lambda\sigma\sigma_h \rangle = \frac{1}{r} \hat{D}^{J*}_{MK}(\phi, \theta, 0) \hat{d}^{j}_{k\omega}(\gamma) \chi_{vj}(r) | \lambda\sigma \rangle | \sigma_h \rangle. \tag{4.7}$$

Here $\hat{D}$ designates a normalized Wigner rotation matrix element, where α and β designate the space-frame orientation of $\vec{R}$, and χ is the OH vibrational wavefunction. The ket $|\lambda\sigma\rangle$ designates the electronic wavefunction of the OH (OD) molecule, where λ and σ are the projections of the electronic orbital and spin angular momenta along $\vec{r}$ and $\omega = \lambda + \sigma$. The second ket $|\sigma_h\rangle$ designates the electronic wavefunction of the H (D) atom, where σ_h is the projection of the H(D)-atom spin along $\vec{R}$.

The determination of the matrix elements of $\mathbf{H}_{el}$ and $\mathbf{H}_{mol}$ in the basis defined by Eq. (4.7) is presented in detail in Ref. [94]. The matrix elements of $\mathbf{H}_{el}$ are the four OHH potential energy surfaces, discussed above. The vibration-rotation-fine-structure levels of the free OH (OD) radical are obtained by diagonalizing $\mathbf{H}_{mol}$ in a parity-adapted, Hund's case (a) basis and the matrix elements are given in Eq. (B.33) of Appendix B. The pertinent spectroscopic constants can be found in the Table B.1

As illustrated schematically in Fig. 4.3, there exist two rotational ladders, F_1 and F_2, separated by the spin-orbit splitting. In addition, for each value of the OH (OD) rotational angular momentum, there exist two Λ-doublet levels, separated by only a fraction of a wavenumber. In the high-J limit, the two Λ-doublet levels can be distinguished by the reflection symmetry of the spatial component of the electronic wavefunction in the plane of rotation of the diatomic [108, 109]. In the lower (F_1) spin-orbit manifold, the levels of nominal A' reflection symmetry are conventionally

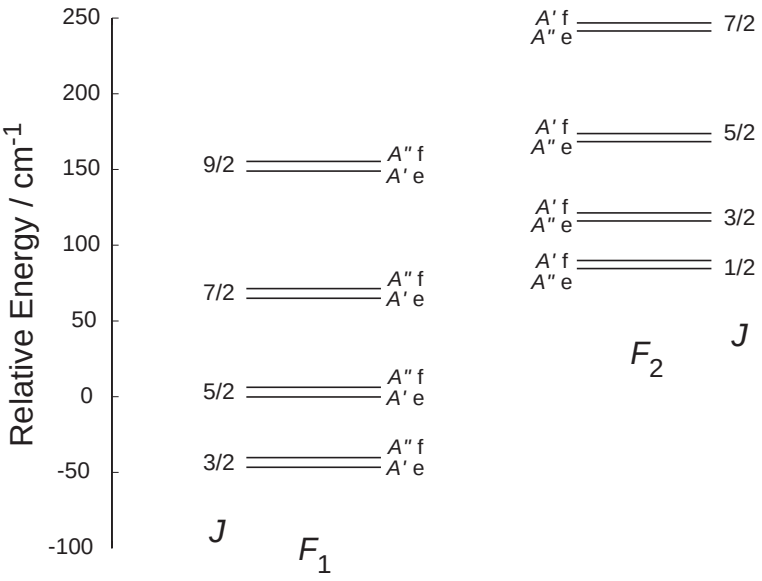

Figure 4.3: Positions of the lower spin-rotation levels of OD($X^2\Pi$).

labelled e and the levels of nominal A'' reflection symmetry, f. This e/f labelling is reversed in the upper (F_2) spin-orbit manifold. Note that the A' Λ-doublet levels are lower in energy in the F_1 spin-orbit manifold, but higher in energy in the F_2 spin-orbit manifold. This situation is reversed in the F_2 spin-orbit manifold for levels with $j \geq 9/2$. Thus, except for the F_2 levels with $1/2 \leq j \leq 7/2$, the lower of the two Λ-doublet levels always corresponds to nominal A' reflection symmetry.

4.2.3 Scattering Calculations

The wave function is expanded in the basis of Eq. (4.7). Premultiplication by individual members of the basis, integration over all the electronic and nuclear coordinates except R and evaluation of the resulting matrix elements gives rise to the set of close-coupled equations familiar in inelastic scattering. These equations are

solved subject to modified boundary conditions which allow for a nonvanishing incoming wave for each adiabatic state which is not energetically closed at the capture radius R_c [89, 90]. The resulting S-matrix is obtained by outward propagation, similar to that in conventional inelastic scattering [101–103]. The S-matrix, although symmetric, is, however, no longer unitary, since the capture boundary condition acts like a sink.

As discussed earlier, [89, 90] the computationally more efficient coupled-states approximation can be used, wherein, along with the total angular momentum J, the projection K of $\vec{J}$ along $\vec{R}$ is assumed conserved. At a given value of the total energy E and the quantum numbers J and K, the probability of capture for an OH+D (OD+H) collision in which the diatomic moiety is in initial state n is

$$P_n^{JK}(E) = 1 - \sum_{n'} \left| S_{nn'}^{JK}(E) \right|^2 . \tag{4.8}$$

Here the sum is over all energetically accessible states in either OH+D or OD+H arrangements. For simplicity we use the single index n to designate the complete set of quantum numbers $\{v, j, k, F_i, \epsilon, \sigma_h\}$.

By microscopic reversibility the probability of decomposition of the complex to yield OH+D products in state n is equal to the probability that state n will be captured into the well. Thus, within the statistical model[95, 100] the state-to-state D+OH→OD+H transition probabilities for a particular value of the total angular momentum J are given by [in analogy with Eq. (1)]

$$P^J_{vjF_i\epsilon\sigma_h \to v'j'F_i'\epsilon'\sigma_h'}(E) = \sum_{KK'} \frac{P^{JK}_{vjF_i\epsilon\sigma_h}(E) P^{JK'}_{v'j'F_i'\epsilon'\sigma_h'}(E)}{\sum\limits_{K''v''j''F_i''\epsilon''\sigma_h''} P^{JK''}_{v''j''F_i''\epsilon''\sigma_h''}(E)}, \tag{4.9}$$

where the sum in the denominator runs over all energetically accessible states in both the D+OH and OD+H arrangements. Although within the coupled-states approximation the projection K of the total angular momentum is conserved within each arrangement, it is not a good quantum number for the overall reaction, so that there appear $K \rightarrow K'$ contributions in Eq. (4.9).

The corresponding integral state-to-state cross sections are calculated from the reaction probabilities as

$$\sigma_{vjF_i\epsilon\sigma_h \rightarrow v'j'F_i'\epsilon'\sigma_h'}(E) = \frac{\pi\hbar^2}{2\mu(E - E_{vjF_i\epsilon})} \frac{1}{2j+1} \sum_J (2J+1) P^J_{vjF_i\epsilon\sigma_h \rightarrow v'j'F_i'\epsilon'\sigma_h'}(E), \tag{4.10}$$

where μ is the collision reduced mass. Scattering calculations were carried out at nearly 300 values of the total energy ranging from 0.2248 eV to 0.7412 eV [as discussed previously, the zero of energy is taken to be D+OH($r = r_e$)]. In all the calculations presented here, except where specifically mentioned, we refer to cross sections involving the vibrational ground state of both OH and OD; consequently, we will hereafter suppress the initial and final vibrational quantum numbers.

The parameters which control the accuracy of the computed statistical-model cross sections are the capture radius, R_c, and the size of the channel basis. The latter is controlled by two parameters E_{max} and j_{max}, so that all OH or OD channels with $j > j_{max}$ or with internal energies $\varepsilon_{vjF_i\epsilon} > E_{max}$ are excluded. The three parameters R_c, E_{max}, and j_{max} were adjusted to ensure the convergence of the capture probabilities P_c to within 0.5%; the adopted values are listed in Table 4.2. In particular, j_{max} was adjusted so that, at the highest value of the total energy,

Table 4.2: Values of the parameters used in the D+OH calculations.

Arrangements	R_c/a.u.	j_{max}	E_{max}/eV[a]
OH+D	3.5	20	0.9
OD+H	3.0	25	0.9

[a]The zero of energy corresponds to OH ($r = r_e$)+D and is the same in both arrangements.

all open rotational levels as well as the lowest four energetically closed levels were included in the channel basis.

4.3 Results and Discussion

4.3.1 Cross Sections

At interstellar temperatures, the two Λ-doublets of the lowest rotational-fine-structure level of OH ($j = 3/2$, F_1) are the most populated and hence will make the most important contribution to the reaction cross section (at T=50K, 86% of the OH population is in these levels). We shall assume that the initial Λ-doublet levels, which differ in energy by a mere fraction of a wavenumber, are equally populated. In this case the integral cross sections for reaction to yield a particular j', F_i' OD final state are obtained from Eq. (5.14) by summing over the two final-state Λ-doublet levels and H-atom spin-projection states, and averaging over the comparable initial states, to obtain:

$$\sigma_{jF_1 \to j'F_i'} = \frac{1}{4} \sum_{\epsilon\epsilon'\sigma_h\sigma_h'} \sigma_{jF_1\epsilon\sigma_h \to j'F_i'\epsilon'\sigma_h'}. \tag{4.11}$$

In this expression , the sum on the right hand side extends over energetically accessible vibrational levels of OD. To determine the initial-state-selected cross section for reaction to yield all OD final states, we further sum over all final states, namely

$$\sigma_{jF_1} = \sum_{j'F_i'} \sigma_{jF_1 \to j'F_i'}. \tag{4.12}$$

Of course, entirely similar statistical model calculations could be carried out to simulate an environment in which the initial Λ-doublet levels were not equally populated. Figure 4.4 illustrates the dependence on collision energy of the over-

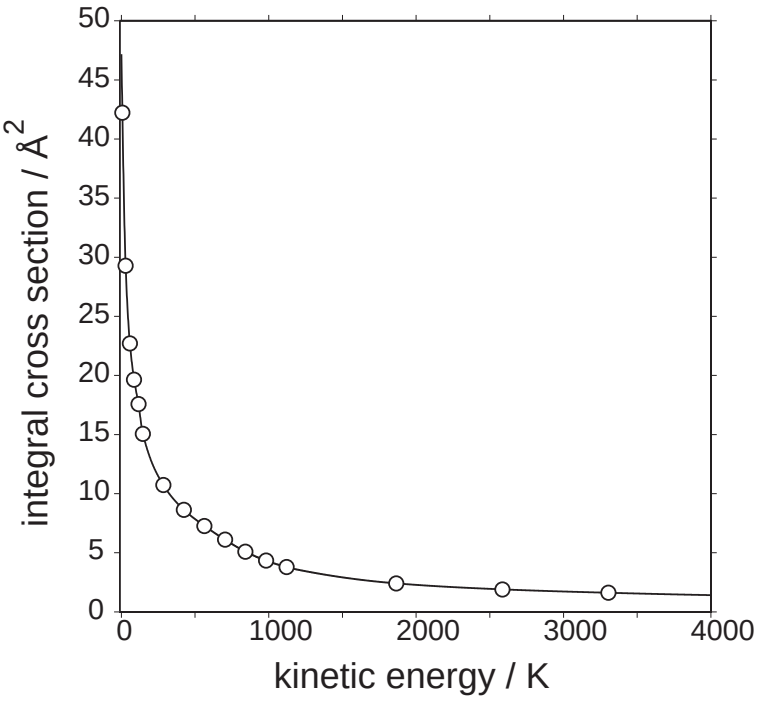

Figure 4.4: Total cross section as a function of the collision energy for D+OH($j = 3/2, F_1$) → OD+H.

all D+OH($j = 3/2, F_1$) →OD+H cross section. As Clary has seen in computational studies of the O+OH reaction, [120] which has a barrierless attractive potential for a

large range of O+OH orientations, our computed cross sections for the title reaction increase as the collision energy decreases. This behavior is expected in general for reactions without an energy barrier [121]. The plot shown in Fig. 4.4 was obtained by a spline fit to the calculated cross sections at particular collision energies. The lowest value of the collision energy in our calculations was 7 K. Consequently, one should not extrapolate the plotted cross sections (or rate constants) to ultracold conditions.

Figure 4.5 plots the initial-state-resolved D+OH→OD+H cross-sections for the thermally accessible OH rotational levels. The cross sections decrease as the rotational quantum number of the diatom increases. The $^1A'$ OH–H potential energy surface is, in fact, strongly attractive only in bent geometries, but quite repulsive for both collinear geometries [94]. Consequently, as the initial OH rotational quantum number increases, the rotational motion averages out the OH–H potential, so that the incoming collision partners "see" less of the collision complex. Hence, the magnitude of the cross sections as well as the low-energy enhancement decreases with increasing j.

In Fig. 4.5 (b), cross sections for OH (F_1) in $j = 1/2$ and $j = 5/2$ reveals an oscillation as a function of increasing kinetic energy which is not observed for the other state selected cross sections. To investigate this behavior, we have performed less expensive purely inelastic scattering calculations for each of the repulsive triplet surfaces ($^3A'$ and $^3A''$). The total relaxation cross section out of $j = 1/2, F_2$ is presented in Fig. 4.6 on a much finer grid of energies. At $E_{col} \approx 80$ K, we observe structure in the cross sections. This behavior can be attributed to the interaction

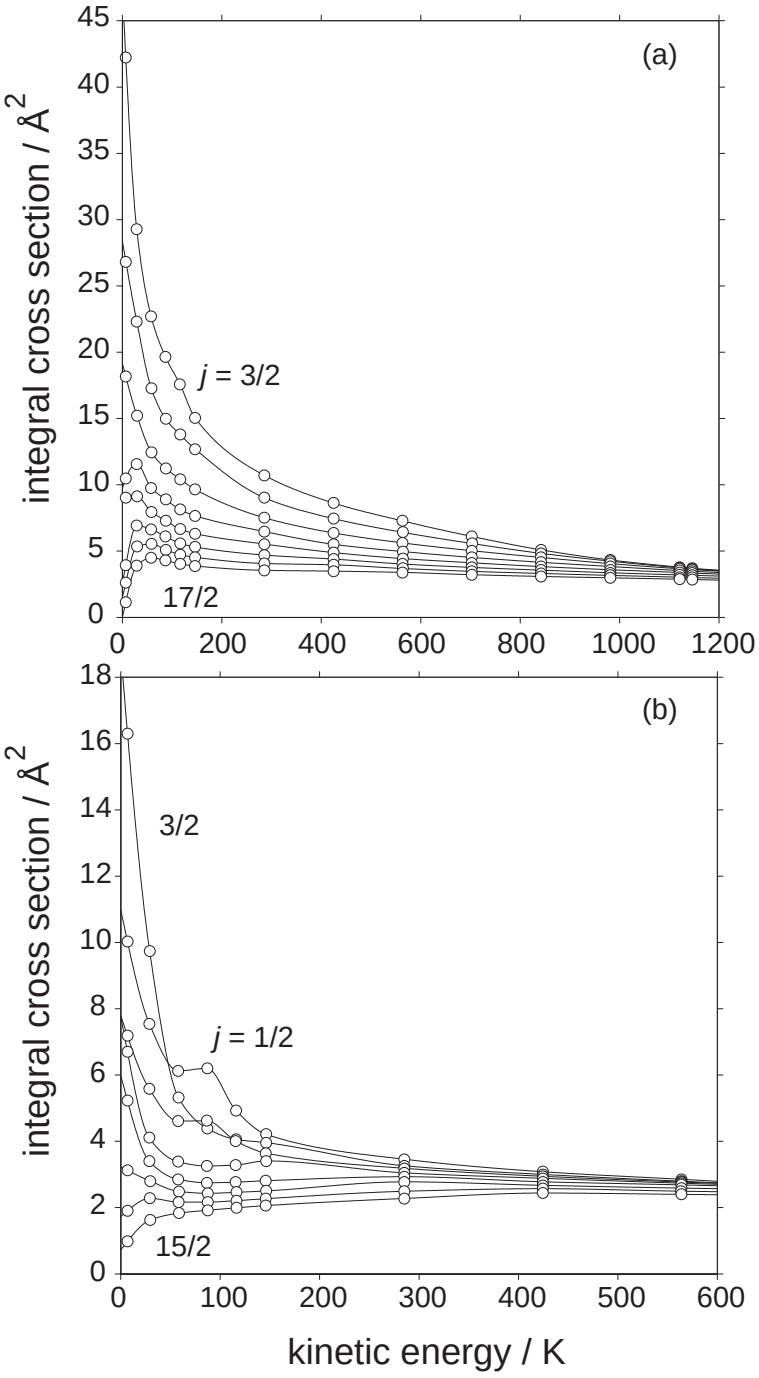

Figure 4.5: Initial state-specific integral cross-sections for reactions of the OH reactant in various rotational levels of the (a) $j = 3/2 - 17/2$ in the F_1 and (b) $j = 1/2 - 15/2$ in the F_2 spin-orbit manifolds. Only the lowest and the highest rotational state of OH are labeled for clarity.

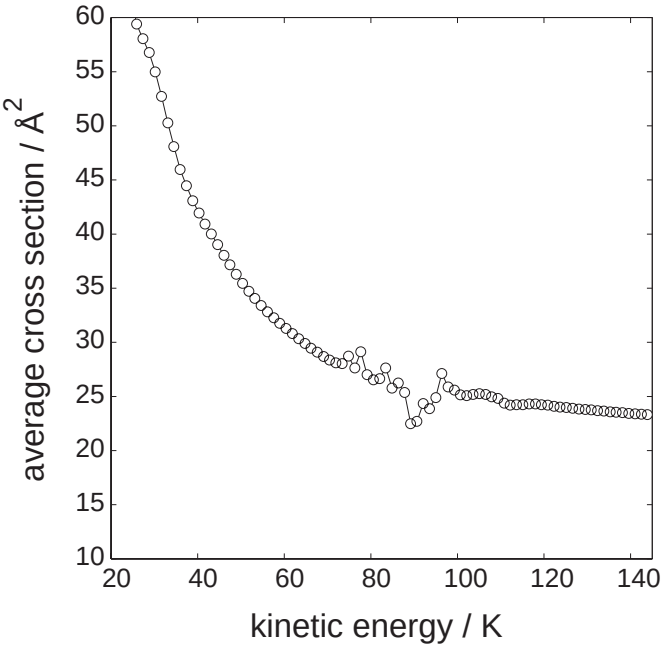

Figure 4.6: Total inelastic scattering cross section for OH($F_2, j = 1/2$) +D on the two repulsive triplet potential energy surfaces, $^3A'$ and $^3A''$. The inelastic scattering calculations were carried out for each potential energy surface separately. The resulting cross sections were then added.

with a Feshbach resonance corresponding to the OH($j = 7/2, F_1$)–D state, which becomes energetically allowed only for $E_{col} \geq 108$K with respect to the OH($j = 1/2, F_2$) state. A similar interaction with a Feshbach resonance corresponding to the OH($j = 9/2, F_1$)–D state is responsible for the structure in the OH($j = 5/2, F_2$)+D cross sections seen in Fig. 4.5 (b).

Murrell *et al.* used QCT calculations, based on an earlier OHH potential energy surface, [122] to determine D+OH→ OD+H cross sections, averaged over a 300 K thermal distribution of OH rotational levels, for several collision energies

ranging from 0.0055 eV to 3.29 eV (64–38,000 K). In Fig. 4.7, we compare their

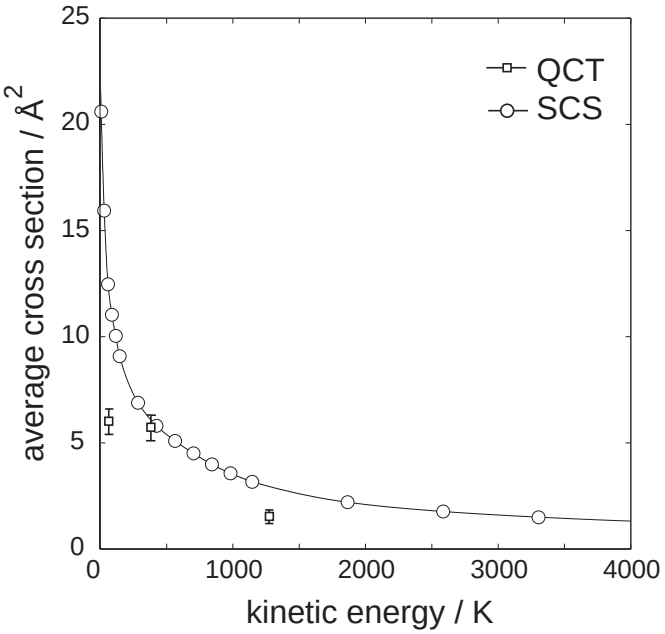

Figure 4.7: Comparison of rotationally averaged D+OH → OD+H cross sections [Eq. (4.13)] from the present statistical-close-coupled calculations with the predictions of the QCT calculations of Ref. [115].

results to our rotationally-averaged cross sections, [123] which we define as

$$\langle \sigma(E_{col}) \rangle = \frac{\sum_{jF_i} (2j+1) \sigma_{jF_i}(E_{col}) \exp(-\epsilon_{jF_i}/kT)}{\sum_{jF_i} (2j+1) \exp(-\epsilon_{jF_i}/kT)}. \tag{4.13}$$

The QCT cross sections are comparable in magnitude, but fail to exhibit the substantial enhancement at low collision energy. It is not clear whether this disagreement reflects shortcomings of the QCT method, differences in the potential energy surfaces used, or the fact that only one potential energy surface was used in the QCT calculation.

4.3.2 Product State Populations

For reactions which are statistical (without any dynamical constraints), the product state distributions will be proportional to both the degeneracy of the product rotational, vibrational and electronic state, and the density of states associated with the recoil translational energy of the products [121]. This density of states is

$$\rho(E_{tr}) = \frac{\mu^{3/2}}{2^{1/2}\pi^2\hbar^3} {E_{tr}}^{-1/2}. \tag{4.14}$$

Thus the probability that reaction at a total energy E will produce state v', j', F_i', ϵ' is

$$\rho(v', j', F_i', \epsilon'; E) = \frac{(2j+1)\mu^{3/2}}{2^{1/2}\pi^2\hbar^3} \left[E - E_{v',j',F_i',\epsilon'}\right]^{-1/2}. \tag{4.15}$$

Consequently, one would anticipate that in a purely statistical limit the cross sections for the title reaction would be given by the "prior" distribution

$$\sigma_{vjF_i\epsilon\rightarrow v'j'F_i'\epsilon'} \propto (2j'+1)\left(E - E_{v'j'F_i'\epsilon'}\right)^{-1/2}. \tag{4.16}$$

Figure 4.8 shows the final-state-resolved cross sections for formation of OD at a collision energy of 6.7 K (4.7 cm^{-1}). We observe in both cases that the distributions, particularly those for formation of OD in the A' Λ-doublet level, [108] display a dependence on j' which corresponds closely to the "prior" distribution of Eq. (4.16).

Because the spin-orbit splitting in OD (139 cm^{-1}, Table 2) is a substantial fraction of the exoergicity of the title reaction (498.6 cm^{-1}), the cross sections for production of rotational levels in the lower (F_1) OD spin-orbit manifold are almost twice as large as those for production of rotational levels in the upper spin-orbit manifold. We observe, however, that this nearly 2:1 ratio is considerably larger

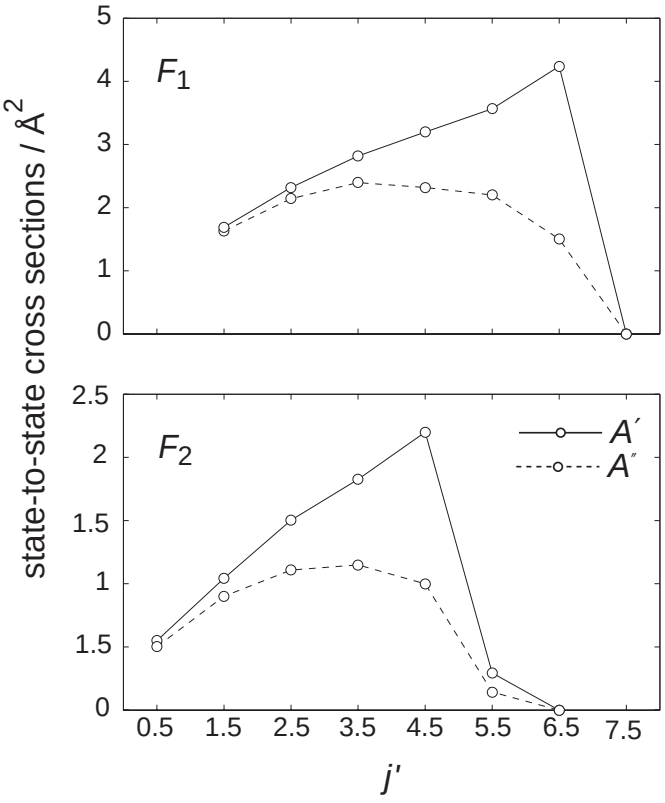

Figure 4.8: Cross sections for production of the energetically accessible OD rotational fine structure levels in the reaction D + OH $(j = 3/2, F_1) \rightarrow$ OD (j', F_i, ϵ) + H at a collision energy of 6.7 K.

than would be predicted by the ratio of the square root of the available translational energy, as would be given by Eq. (4.16).

We also observe a marked propensity toward formation of OD in the A' Λ-doublet level. This is identical to what was found in our earlier [94] statistical model calculations on the $O(^1D)+H_2 \rightarrow OH+H$ reaction and also to what had been reported in earlier experimental investigations [124, 125]. Although the exoergicity of the $O(^1D)+H_2$ reaction ($\Delta E = -1.89$ eV $= -15,200$ cm^{-1}) is much greater than that of the title reaction ($\Delta E = -0.06$ eV $= 499$ cm^{-1}), nonetheless the same

Λ-doublet propensity is observed.

As discussed in the earlier publication of Alexander *et al.*, [94] and suggested by Wiesenfeld, Butler and co-workers [124] in the interpretation of their experiments, the A' reflection symmetry of the H_2O electronic wavefunction is conserved as the complex breaks apart into OH+H. During this breakup there is a strong dynamical preference for the plane of rotation of the OH fragment to be roughly parallel to the plane of rotation of the complex. Consequently, the electronic wavefunction of the nascent OH fragment will be preferentially symmetric with respect to reflection in the plane of rotation of the OH fragment, which corresponds to the A' Λ-doublet [108]. An identical Λ-doublet propensity is predicted here for formation of OD by the OH+D exchange reaction at much lower translational energies.

We observe also in Fig. 4.8 that the dependence on rotational quantum number of the cross sections for formation of OD products in the A'' Λ-doublet level are less well charaterized by the statistical prior distribution of Eq. 4.16. Since the deep H_2O well corresponds to a state of A' symmetry, for preferential decomposition of the complex in which the plane of rotation of the nascent OD products corresponds to the plane of the H_2O complex, the A'' Λ-doublet state can be formed only by a curve-crossing at longer range with a repulsive potential energy corresponding to a state of A'' electronic symmetry [94]. Thus, one might anticipate a less "statistical" j' dependence for the OH[$\Pi(A'')$] products, since they are not formed directly by decomposition of the H_2O complex.

Figure 4.9 plots the cross sections for several initial rotational levels of OH. The reactive cross sections decrease with increasing rotational excitation of the di-

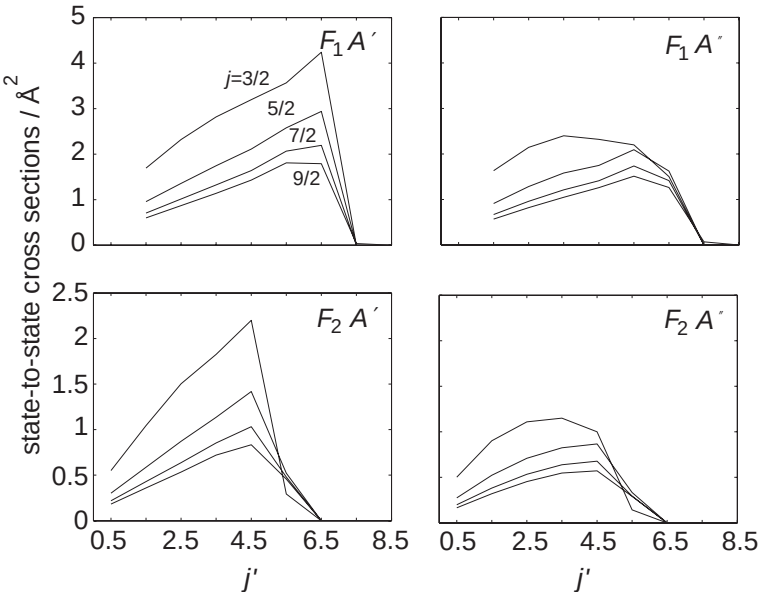

Figure 4.9: OD rotational populations for each Λ-doublet separately in both the F_1 (upper panels) and F_2 (lower panels) spin-orbit manifolds for the reaction D+OH(j, F_1)→OD(j', F_i', ϵ')+H for initial rotational levels $j = 3/2 - 9/2$ at a collision energy of 6.7 K.

atomic reactant, similarly to what has been observed previously in ion-molecule [96] reactions and the neutral insertion reactions [92, 120, 126]. We also observe in Fig. 4.9 that with increasing OH rotational excitation the product OD rotational distribution encompasses higher values of j'. This occurs because, for a given collision energy, an increase in reactant rotational energy increases the total energy of the system, and, hence, the total energy available to OD rotation.

4.3.3 Rate Constants

Having state-to-state cross sections at our disposal, we can calculate the thermally averaged rate constants by assuming a Maxwellian distribution of translational energy at temperature T. The corresponding state-to-state thermally averaged rate constants are given by [127]

$$k_{i\to f}(T) =< v\sigma_{i\to f} >= \left[\frac{8}{\pi\mu(kT)^3}\right]^{1/2} \int_0^\infty E_{tr}\ \sigma_{i\to f}(E_{tr})\ exp(-\frac{E_{tr}}{kT})\, dE_{tr}\,, \quad (4.17)$$

where v is the initial relative velocity, and E_{tr} the initial translational energy, for the OH reactant in initial state i. The overall thermal rate constant, for the OH reactant in initial state i, is obtained by summing over all energetically accessible product states, namely

$$k_i(T) = \sum_f k_{i\to f}(T)\ . \quad (4.18)$$

The overall thermal rate constant for the title reaction is then obtained by averaging over an assumed Boltzmann distribution of OH rotational levels in both the F_1 and F_2 spin-orbit manifolds. We have

$$k(T) = \frac{\sum\limits_i g_i \exp(-\varepsilon_i/kT) k_i(T)}{Q} \quad (4.19)$$

Here $Q(T)$ is the partition function and g_i and ε_i designate, respectively, the degeneracy and internal energy of the i^{th} state of the OH reactant. Here, the index i designates the full set of initial quantum numbers $\{jF_i\epsilon\}$. The rate constants [Eq. (4.18)] corresponding to successively higher degrees of initial rotational excitation of the OH molecule are shown in the Fig. 4.10 (for rotational levels in the F_1 spin-orbit manifold) and Fig. 4.11 (for rotational levels in the F_2 spin-orbit man-

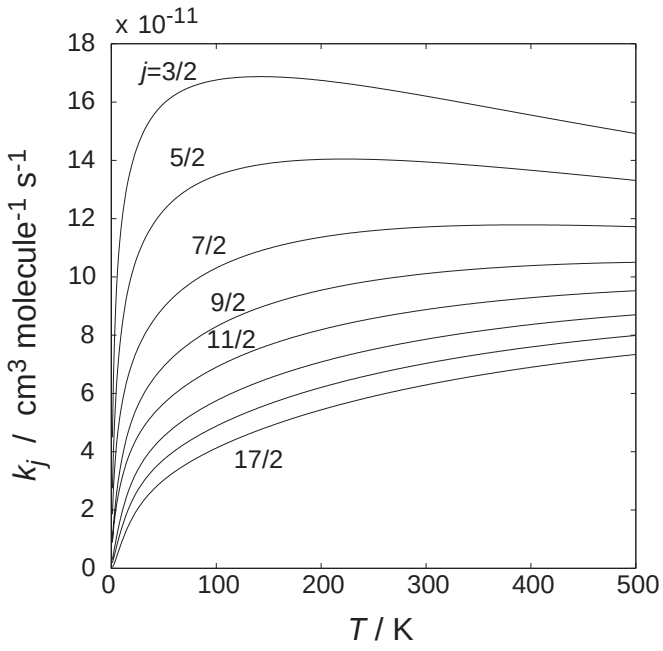

Figure 4.10: The temperature dependence of the rate constant for D + OH ($j = 3/2 - 17/2$, F_1)→ OD+H. The rate constants decrease for an increasing degree of rotational excitation of the OH reactant.

ifold). As seen for the cross sections, the rate constants decrease with increasing initial rotational excitation. Because the spin-orbit splitting in OH ($\Delta E = 139$ cm^{-1} = 200 K) is much larger than typical interstellar temperatures, the most important contribution to the overall rate for the title reaction will be from rotational levels in the ground spin-orbit state of OH. As seen in Fig. 4.5, these have the largest reactive cross sections.

The rate constants are large, as would be expected for a barrierless reaction. Although we observe a slight negative temperature dependence for the lowest two states, namely $F_1, j = 3/2$ and $j = 5/2$ (see Fig. 4.10), the initial state selected rates

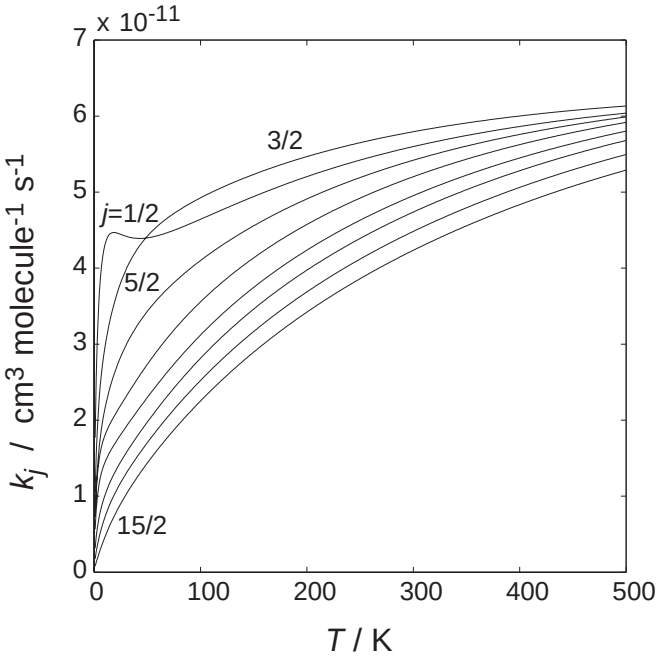

Figure 4.11: The temperature dependence of the rate constant for OH ($j = 1/2 - 15/2, F_2$) + D$\rightarrow$ OD+H.

are generally increase with temperature in contrast to the thermally averaged rate, $k(T)$ [114], shown in Fig. 4.12. Thus we conclude, confirming the earlier observations of Clary and coworkers [120, 126], that the negative temperature dependence of the thermally averaged rate for barierless reactions controlled by long-range forces is mostly due to thermal averaging over the rotationally accessible states. Since rotational excitation reduces the cross sections, the thermally averaged rate constant will decrease at higher temperature as higher rotational levels make a greater contribution to Eq. (4.19).

A similar behavior has been reported for several radical-radical reactions [10]. This behavior is interpreted as a fingerprint of complex formation [114]. As the

collision energy increases, the possibility of the breakup back towards reactants become more probable as the density of accessible states for the products and the reactants becomes similar.

The most recent and detailed experimental information on the rate constant for the title reaction are the measurements of Howard and Smith, which were fitted over the temperature range 300 K$< T <$ 500 K [114]. The fitting function used is

$$k(T) = (1.9 \pm 0.3) \times 10^{-9}\ T^{-(0.63\pm0.05)}\ \mathrm{cm^3 molecule^{-1}\ s^{-1}}. \qquad (4.20)$$

The thermally averaged rate constant predicted by our calculations is shown in Fig. 4.12 and compared to the experimental fit of Howard and Smith [114] together with the earlier theoretical and experimental values. The calculated rate constant lies between the earlier experimental result of Margitan and the fit by Howard and Smith, and it confirms the earlier theoretical estimates. Consequently, our results suggest that Howard and Smith might have underestimated the rate constant for the title reaction.

4.4 Summary

In this paper, we have reported state-to-state cross sections and thermal rate constants for the D+OH($X^2\Pi$)→OD($X^2\Pi$)+H isotope exchange reaction, determined with the statistical, coupled-states method of Rackham *et al.* [89, 90] extended to open-shell systems [94].

The comparison of the thermally averaged cross sections calculated in this work with the cross section determined by QCT calculations on an earlier potential

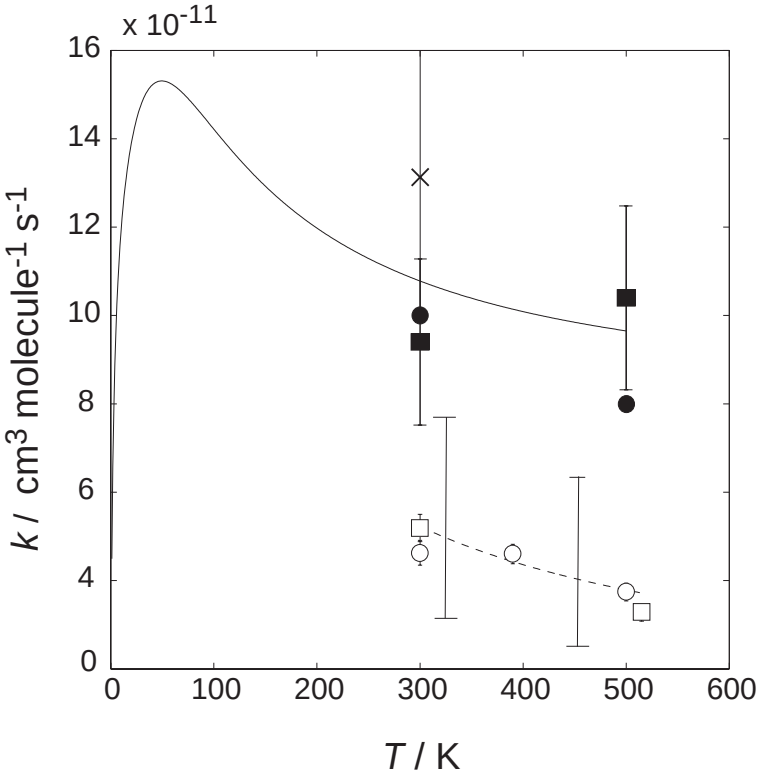

Figure 4.12: Thermally averaged rate constant for the isotope exchange reaction D+OH → OD+H (solid curve). The experimental fit indicated by the dashed curve is taken from Ref. [114] [see Eq. (4.20)]. The extended error bars designate the precision of this empirical fit. The open circles and open squares represent data obtained using H_2O or HNO_3, respectively, as the OH precursor. The "X" designates the experimental rate constant from Ref. [116]. The filled data points represent the earlier theoretical predictions, circles from Ref. [114] and squares from Ref. [115].

energy surface shows this method fails to predict correctly the low energy behavior of the cross sections. The cross sections from the statistical capture method are significantly higher in the low energy range that is important in the interstellar medium.

We observe a negative temperature dependence of the thermally averaged rate. The state selected rate constants reveal that this behaviour is due primarily to the thermal averaging over the rotationally accessible states. Rotation of the OH radical reduces the cross sections due to the anisotropy in the lowest (the only reactive) potential energy surface, $^1A'$. This potential energy surface is attractive, leading to the HOD complex, in T-shaped geometry ($\theta = 90^o$; see Fig. 3 of Ref. [94]), but repulsive for colinear approach. Correspondingly, if the rotation of the diatom is fast on the time scale of the collision, the effective potential will be less attractive, leading to a lower probability of capture into the HOD complex.

On the basis of their experimental results, Howard and Smith [114] inferred a similar negative energy dependence of the cross sections, however they attribute this behavior to a tendency for the complexes to decompose preferentially to reactants rather than products as the temperature increases. It would be interesting to compare the results of statistical model calculations on a single potential energy surface, similar to those described in Refs. [89, 90] with the results of the present calculations, in which all four of the OH+H potential energy surfaces were included.

We also predict a marked, nonstatistical propensity for production of OD in the A' Λ-doublet level. A similar propensity towards the formation of the symmetric Λ-doublet has been observed in the production of OD in the reaction O(^1D) +

D_2 [128]. This insertion reaction proceeds *via* the water complex. Because of the large exoergicity of the $O(^1D) + D_2 \rightarrow$OD+D reaction, the OD products are formed with far greater internal energy than in the case of the title reaction.

We predict rate constants for D+OH isotopic exchange which confirm the earlier theoretical and experimental results. At 300 K we predict $k(T) = 10.78 \times 10^{-11}$ cm^{3}molecule^{-1}s^{-1}. At lower temperature $T \leq 50K$, the value rises to $k(T) = 15 \times 10^{-11}$ cm^{3}molecule^{-1}s^{-1}, comparable to the value assumed by Croswell and Dalgarno in their modelling investigation of the abundance of interstellar OD [34]. Our calculations predict that OD from the title reaction will be produced in the energetically lower Λ-doublet level, except, however, for the $j = 1/2 - 7/2$ levels of the upper (F_2) spin-orbit manifold. Thus OD masing, for OD producted by the title reaction, might occur for these latter levels. Although the OD molecule has not yet been detected in interstellar clouds, [129] we do encourage further searches, particularly for the five lowest rotational levels of the upper spin-orbit manifold.

Chapter 5

Coupled-States Statistical Investigation of Vibrational and Rotational Relaxation of OH($^2\Pi$) by Collisions with Atomic Hydrogen

5.1 Introduction

The hydroxyl radical is an important species in combustion, astrophysics and atmospheric chemistry. In the Earth's atmosphere, vibrationally activated OH is produced by the following reactions [130, 131] :

$$H + O_3 \rightarrow OH(\nu \leq 9) + O_2 \text{ (mesopause)} \tag{5.1}$$

$$O(^1D) + H_2O \rightarrow 2OH(\nu \leq 3) \text{ (stratosphere and troposphere)} \tag{5.2}$$

To model the chemistry of the OH radical, subsequent to formation, it is essential to understand the rates of OH vibrational relaxation [132]. The collisional relaxation of OH in its ground ($X^2\Pi$) electronic state with a number of atomic [133, 134] as well as diatomic molecules [133–143], has been subject of many, mostly experimental, studies.

Vibrational relaxation of free radicals has been less well studied than that of closed-shell systems. Smith has argued [136] that the rates of vibrational relaxation in potentially reactive encounters are much higher than for non-reactive encounters. In particular, for radical-radical collisions, there is often a barrierless access to a

deep well. Within this complex, the statistical scrambling of the various degrees of freedom should allow access to all energetically-allowed rovibrational states [136, 144]. The adiabatic channel model [145–147] can be used to simulate this statistical scrambling of energy. In addition, collisions of open-shell species are often governed by multiple potential energy surfaces, which are degenerate asymptotically [148, 149]. In this case crossing between attractive and repulsive adiabats corresponding to multiple potential energy surfaces should facilitate vibrational relaxation [148].

Smith has argued [136] that the formation of the collision complex is the rate determining step so that the rate of relaxation will not depend significantly on the degree of vibrational excitation of the reactants. On the other hand, since the topology of the attractive potential energy surface will depend on the bond distance of the diatomic moiety, it may well be that access to the complex does depend on the degree of vibrational excitation.

Recent developments in statistical theories of reaction dynamics by Manolopoulos and co-workers [89, 90, 94] now allow one to go beyond earlier adiabatic channel [145–147] methods by carrying out fully-quantum scattering calculations which include all couplings prior to capture into the complex. A time-dependent version of this method was subsequently developed by Guo and co-workers [91, 92]. These quantum capture calculations have been successfully applied to insertion reactions [89–92] which traverse a deep well. More recently, Alexander, Rackham and Manolopoulos [94] modified and extended the theory to include nonadiabatic couplings between asymptotically degenerate electronic states.

In this paper, we use the same quantum capture method to investigate the in-

elastic scattering dynamics of the OH radicals in collision with H. Although collision of OH with H is not an important process in the mesosphere, this simple system can serve as a prototype for the study of the effect of complex formation on vibrational relaxation. One particular goal of the present study will be the investigation of the relative efficiency of vibrational relaxation during collisions which do not penetrate the complex as compared to vibrational relaxation by redistribution of energy within the complex.

To the best of our knowledge, there have appeared only two reports of measurements of vibrational relaxation rates of OH due to collisions with H atoms. In a study of the reaction of NO_2 with atomic hydrogen, Spencer and Glass [144] reported the relaxation rates of OH in $v = 2$ and $v = 1$ with collisions with H (see Table 5.1). More recent measurements have been reported by Smith *et al.* [55] These authors determined the rate of reaction and relaxation of H_2O by collisions with H and H_2O, and report the relaxation rate of OH ($\nu = 1 \rightarrow 0$) to be $\approx 1.5 \times 10^{-10}$ $cm^3 molecule^{-1} s^{-1}$ (see Table 5.1), which corresponds to a thermally averaged cross-section of ≈ 5.5 Å^2. The only theoretical determination of OH(v)+H relaxation rates is an early study by Quack and Troe [145].

In addition to its importance in atmospheric chemistry, the OH radical has drawn considerable attention because of the importance of the OH maser as a tool for acquiring insights into the physical processes occurring within interstellar clouds [150–152]. The presence of the OH molecule in interstellar clouds is identified by its four radio emission lines at frequencies of 1612, 1665, 1667 and 1720 MHz [153]. These are attributed to maser emission from inverted populations in

Table 5.1: Summary of calculated and measured rate constants for the vibrational relaxation of OH($v = 1, 2$).

	$k_{v\to v'}$ / 10^{-10} cm^3 molecule^{-1} s^{-1}			
T / K	$2 \to 0$	$2 \to 1$	$2 \to 1 + 0$	$1 \to 0$
50	1.259[a]	0.842[a]	2.099[a]	2.013[a]
100	1.209[a]	0.788[a]	1.996[a]	1.915[a]
300	1.043[a]	0.654[a]	1.697[a]	1.600[a]
	1.43 [b]	0.753[b]	2.18 [b]	2.1[b]
			3.3[c]	2.7[c]
				1.5 ± 0.4[d]
				1.4 ± 0.12[e]

[a]This work.

[b]Theoretical; Ref. [145].

[c]Experimental; Ref. [144].

[d]Experimental; Ref. [55], derived from an experiment in which H_2O was excited to the $|13>$ vibrational level.

[e]Experimental; Ref. [55], derived from an experiment in which H_2O was excited to the $|12>$ vibrational level.

the Λ-doublet levels of the OH molecule. Fig. 5.1 shows a diagram of the lowest Λ-doublet with the hyperfine-structure responsible for the indicated emissions.

There have been numerous suggestions about the possible pump mechanisms responsible for the Λ-doublet level population inversion. One possible cause involves inelastic collisions of OH with H and H_2, followed by radiative decay [35–38]. Suppose that collisional excitation to higher rotational levels were to favor, preferentially, the upper Λ-doublet. Subsequent radiative transitions to the ground rotational level will change the parity but conserve the Λ-doublet label. As a consequence, the upper Λ-doublet of the ground rotational level will be preferentially populated.

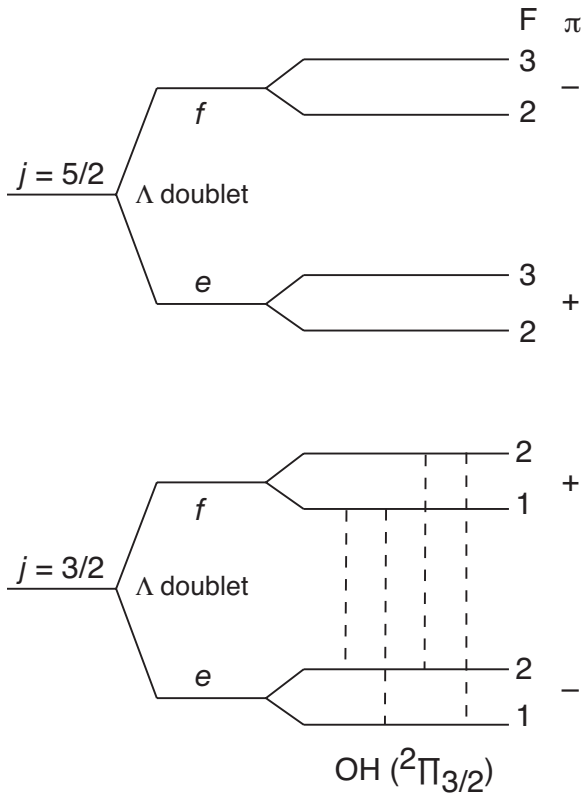

Figure 5.1: Schematic diagram of the lowest two rotational levels in the lower F_1 ($^2\Pi_{3/2}$) spin-orbit manifold of OH. The levels are labeled with the total angular momentum exclusive of the nuclear spin, j, the e/f symmetry (Λ-doublet) labels (Refs. [154] and [108]), the total angular momentum including the nuclear spin, F, and the parity π. This figure is adapted from Fig. 1 of Ref. [155]. The Λ-doublet and hyperfine splittings are greatly exaggerated for clarity. The four OH maser transitions at 1612, 1665, 1667 and 1720 MHz are shown by the dashed vertical lines.

There have appeared a number of sophisticated studies of rotationally inelastic collisions of OH with H_2 [155–160]. The theoretical simulation of collisions of OH with H atoms is further complicated by the presence of the deep H_2O well, as well as by the necessity of dealing with the open-shell character of both OH($^2\Pi$) and H(^2S), with non-zero electronic orbital angular momentum, electronic spin, and nuclear spin. An early, approximate study by Bertojo and coworkers [37] supported the pumping mechanism discussed in the previous paragraph.

To the best of our knowledge, the first rigorous theoretical treatment which retained the open-shell character of both the OH radical and the H atom was presented by Shapiro and Kaplan [161]. These authors calculated state-to-state rate constants for transitions between and within the $j = 3/2$ and $j = 5/2$ rotational levels in the (lower) $^2\Pi_{3/2}$ spin-orbit manifold. They predicted steady-state level distributions by means of a simple cloud model which included their rate constants, stimulated and spontaneous emission probabilities and the 2.7 K background radiation. Their model predicted that OH + H inelastic collisions could play an important role in producing the observed Λ-doublet inversions.

As shown schematically in Fig. 5.2, a complete description of the interaction of OH($X^2\Pi$) with H(^2S) requires four potential energy surfaces ($^{1,3}A'$ and $^{1,3}A''$) [94]. Of these, three are repulsive, while one ($^1A'$) correlates with the deep H_2O (X^1A') well. Consequently, rotational and ro-vibrational relaxation of OH in collisions with H can occur either by scattering on the repulsive PESs, in a manner similar to the inelastic scattering of OH by noble gas atoms, or by collisions which enter the H_2O well and then re-emerge (the O+H_2 channel is energetically closed at collision

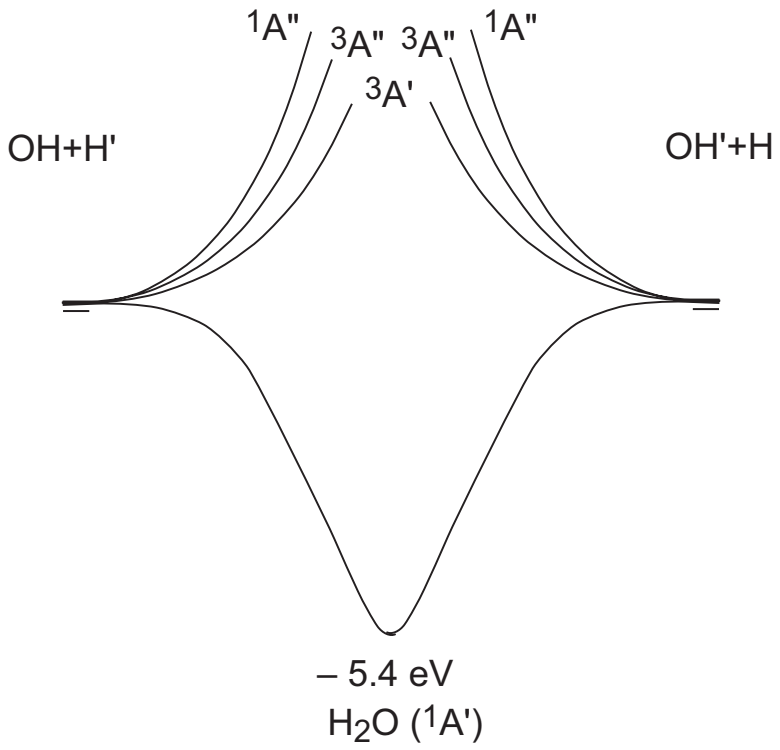

Figure 5.2: Schematic illustration of the OH + H′ ↔ OH′+H potential energy surfaces. The O(^1D)+H_2 arrangement (not shown) lies 1.89 eV higher than the OH+H asymptotes.

energies below 1.8 eV).

The goal of this chapter will be to use the coupled-states statistical method, [89, 90] as extended by Alexander, [94] in the determination of cross sections for rotational and ro-vibrational relaxation of OH($X^2\Pi$) in collisions with H. Section 5.2 summarizes the relevant details of the method, the Hamiltonian, PESs and the calculations. In Sec. 5.3, we present cross sections and thermal rate constants for $v = 1, 2 \rightarrow v = 0$ rovibrational relaxation and for rotationally inelastic collisions within the $v = 0$ level. A brief summary concludes the chapter.

5.2 Theory and Computational Methods

Even at energies below the O(^1D)+H_2 channel, the title reaction samples the product valley of the O(^1D)+H_2 →OH+H insertion reaction. Here we apply the close-coupled statistical method to the inelastic scattering of OH in collisions with H. The Coupled-channel statistical model and the relevant PESs are introduced earlier in Chapter 3, therefore we present briefly the specifics of the calculations pertaining to the relaxation of OH in collisions with hydrogen atom.

The probability of collisional transfer from state n to state n', due to capture and then subsequent decay of the metastable complex is:

$$P_{nn'}^{complex} = \frac{P_n P_{n'}}{\sum_{n''} P_{n''}}. \tag{5.3}$$

Here P_n and $P_{n'}$ are the respective capture probabilities for states n and n'. In the studies of chemical reactions, which were the object of the earlier articles [89, 90, 94], P_n and $P_{n'}$ refer to separate arrangements. Here, as will be discussed in more detail below, these two capture probabilities can refer either to the same, or different, arrangements. The sum in the denominator runs over all energetically accessible states in any arrangement.

Experimentally it would be difficult (if not impossible) to distinguish the separate contribution to inelastic scattering from collisions which are absorbed into the complex ($P_{n'n}^{complex}$, Eq. 5.3) from the contribution to relaxation which occurs by scattering on the repulsive potential energy surfaces ($P_{n'n}^{direct}$), in a manner similar to the inelastic scattering of OH in collisions with noble gas atoms. As will be discussed in more detail below, the latter probability is calculated from the S-matrix,

just as in conventional inelastic scattering calculations.

In fact, vibrational relaxation can occur by this direct (non-capture) scattering in the initial arrangement

$$\mathrm{OH}(v,j) + \mathrm{H}' \rightarrow \mathrm{OH}(v',j') + \mathrm{H}' \,, \tag{5.4}$$

by decay of the complex back to the initial arrangement

$$\mathrm{OH}(v,j) + \mathrm{H}' \rightarrow \mathrm{HOH}'^{\dagger} \rightarrow \mathrm{OH}(v',j') + \mathrm{H}' \,, \tag{5.5}$$

or by decay of the complex accompanied by hydrogen atom exchange

$$\mathrm{OH}(v,j) + \mathrm{H}' \rightarrow \mathrm{HOH}'^{\dagger} \rightarrow \mathrm{OH}'(v',j') + \mathrm{H}. \tag{5.6}$$

Let us designate by $P^a_{n'}$ and $P^b_{n'}$ the capture probabilities for the the $\mathrm{OH}(v',j')$+H$'$ and $\mathrm{OH}'(v',j')$+H arrangements, where the single index n' stands for v',j'. The total vibrational deactivation probability for processes (5.4)–(5.6) is given by the sum of the probabilities for complex-mediated $\mathrm{OH}(v,j) \rightarrow \mathrm{OH}(v',j')$ and $\mathrm{OH}(v,j) \rightarrow \mathrm{OH}'(v',j')$ relaxation, plus the probability for direct $\mathrm{OH}(v,j) \rightarrow \mathrm{OH}(v',j')$ relaxation through collisions which do not enter the complex. In other words

$$P^{tot}_{nn'} = \frac{P^a_n P^a_{n'} + P^a_n P^b_{n'}}{\sum\limits_{n''} P^a_{n''} + P^b_{n''}} + P^{direct}_{nn'} = \frac{P^a_n P^a_{n'}}{\sum\limits_{n''} P^a_{n''}} + P^{direct}_{nn'} \,. \tag{5.7}$$

The simplification made in Eq. (5.7) exploits the fact that the $\mathrm{OH}(v',j')$ + H$'$ and $\mathrm{OH}'(v',j')$+H capture probabilities, $P^a_{n'}$ and $P^b_{n'}$, are identical.

5.2.1 Hamiltonian and Basis

The capture probabilities are determined according to the Hamiltonian,

$$\mathbf{H}_{\mathrm{OH+H}}(\vec{R},\vec{r},\vec{q}) = \mathbf{T}_n(\vec{R}) + \mathbf{V}_{el}(\vec{q};\vec{R},\vec{r}) + \mathbf{H}_{mol,\mathrm{OH}}(\vec{q};\vec{r}). \tag{5.8}$$

Here $\vec{R}$ and $\vec{r}$ are the Jacobi coordinates for a particular arrangement, and $\vec{q}$ represents the electronic coordinates. The first term $\mathbf{T}_n$ represents the kinetic energy of the relative atom-diatom motion:

$$\mathbf{T}_n = -\frac{\hbar^2}{2\mu R^2}\frac{\partial}{\partial R}R^2\frac{\partial}{\partial R} + \frac{L_{op}^2}{2\mu R^2}. \tag{5.9}$$

The second term $\mathbf{V}_{el}$ is the electrostatic interaction, while the third term $\mathbf{H}_{mol}$ is the OH molecular hamiltonian.

The overall wavefunction for the OH–H system is expanded in the basis

$$\langle\hat{R},\vec{r}|JMKvjk\lambda\sigma\sigma_h\rangle = \frac{1}{r}\hat{D}^{J*}_{MK}(\Omega)\hat{d}^{j}_{k\omega}(\gamma)\chi_{vj}(r)|\lambda\sigma\rangle|\sigma_h\rangle. \tag{5.10}$$

Here, J is the total angular momentum with projection K along OH-H vector $\vec{R}$ and M along the space-frame z-axis. The quantum number j designates the rotational angular momentum of OH diatom, with projection k along $\vec{R}$ and with projection w along $\vec{r}$. $\hat{D}^{J*}_{MK}(\Omega) = ([2j+1]/8\pi^2)^{1/2}D^{J*}_{MK}(\Omega)$ is the normalized Wigner rotation matrix element, where Ω designate the three euler angles that relate the space-fixed and body-fixed axis frames. χ is the OH vibrational wavefunction. The ket $|\lambda\sigma\rangle$ designates the electronic wavefunction of the OH molecule, where λ and σ are the projections of the electronic orbital and spin angular momenta along $\vec{r}$ and $\omega = \lambda+\sigma$. The second ket $|\sigma_h\rangle$ designates the electronic wavefunction of the H atom, where σ_h is the projection of the H-atom spin along $\vec{R}$. The total projection of the total angular momenta J along $\vec{R}$ is $K = k + \sigma_h$.

The determination of the matrix elements of $\mathbf{V}_{el}$ and $\mathbf{H}_{mol}$ in the basis defined by Eq. (5.10) is presented in detail in Ref. [94]. As discussed in Ref. [94], the matrix elements of $\mathbf{V}_{el}$ can be evaluated in terms of the four OHH potential energy surfaces, shown schematically in Fig. 5.2.

The vibration-rotation-fine-structure levels of the free OH radical are obtained by diagonalizing $\mathbf{H}_{mol}$ in a parity-adapted, Hund's case (a) basis. The matrix elements of $\mathbf{H}_{mol}$ are given in Eq. (B.33) of Appendix. The pertinent spectroscopic constants can be found in the Table B.1

As illustrated schematically in Fig. 5.3, there exist two rotational ladders, F_1 and F_2, separated by the spin-orbit splitting. In addition, for each value of the OH rotational angular momentum, there exist two Λ-doublet levels, separated only by a fraction of a wavenumber. In intermediate and case (b) Hund's coupling, the two Λ-doublet levels can be distinguished by the reflection symmetry of the spatial part of the electronic wavefunction in the plane of rotation of the diatomic [108]. In the lower (F_1) spin-orbit manifold, the e-labelled Λ-doublet levels [154] have, in the high-j limit, nominal A' reflection symmetry, while the f-labelled levels have nominal A'' reflection symmetry [108, 109]. The association of reflection symmetry with the e/f label is reversed in the upper (F_2) spin-orbit manifold. Note that the A' Λ-doublet levels are lower in energy in the F_1 spin-orbit manifold, but higher in energy in the F_2 spin-orbit manifold. This situation is reversed in the F_2 spin-orbit manifold for levels with $j \geq 9/2$. Thus, except for the F_2 levels with $1/2 \leq j \leq 7/2$, the lower of the two Λ-doublet levels always corresponds to nominal A' reflection symmetry.

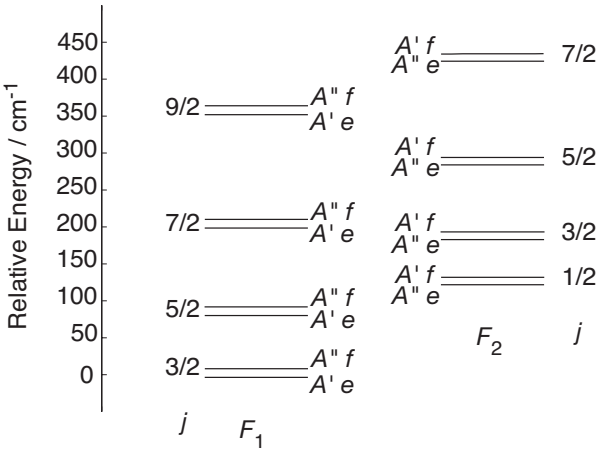

Figure 5.3: Positions of the lower spin-rotation levels of OH($X^2\Pi$). For clarity, the magnitude of the Λ-doublet splitting has been greatly exaggerated in the figure.

5.2.2 Scattering Calculations

The wave function is expanded in the basis of Eq. (5.10). Premultiplication by individual members of the basis, integration over all the electronic and nuclear coordinates except R and evaluation of the resulting matrix elements following the preceding subsection gives rise to the set of close-coupled equations familiar in inelastic scattering. These equations are solved subject to modified boundary conditions which allow for a nonvanishing incoming wave for each adiabatic state which is not energetically closed at the capture radius R_c [89, 90]. The resulting S-matrix is obtained by outward propagation, similar to the procedure in the conventional treatment of inelastic scattering [101–103]. The S-matrix, although symmetric, is, however, no longer unitary since the capture boundary condition acts like a sink.

As discussed earlier, [89, 90] the computationally more efficient coupled-states approximation can be used, wherein both the total angular momentum J and its

projection K along $\vec{R}$ are conserved. At a given value of the total energy E and the quantum numbers J and K, the probability of capture for an OH+H$'$ collision in which the diatomic moiety is in initial state n is

$$P_n^{JK}(E) = 1 - \sum_{n'} \left| S_{nn'}^{JK}(E) \right|^2 = 1 - \sum_{n'} P_{nn'}^{JK,direct}. \tag{5.11}$$

Here the sum is over all energetically accessible states. In reality the single index n designates the set of quantum numbers $\{v, j, k, F_i, \varepsilon, \sigma_h\}$. The transition probability for an inelastic $n \rightarrow n'$ transition, due to coupling before capture, which appears in Eq. (5.7), is given by

$$P_{nn'}^{JK,direct} = \left| S_{nn'}^{JK}(E) \right|^2. \tag{5.12}$$

If we insert, explicitly, all the relevant quantum numbers, then Eq. (5.7) becomes

$$P^J_{vjF_i\varepsilon\sigma_h \rightarrow v'j'F_i'\varepsilon'\sigma_h'}(E) = \sum_{KK'} \frac{P^{JK}_{vjF_i\varepsilon\sigma_h}(E) P^{JK'}_{v'j'F_i'\varepsilon'\sigma_h'}(E)}{\sum\limits_{K''v''j''F_i''\varepsilon''\sigma_h''} P^{JK''}_{v''j''F_i''\varepsilon''\sigma_h''}(E)} + \sum_K \left| S^{JK}_{vjF_i\varepsilon\sigma_h \rightarrow v'j'F_i'\varepsilon'\sigma_h'}(E) \right|^2. \tag{5.13}$$

Within the coupled-states approximation the projection K of the total angular momentum along in the Jacobi vector of relative motion is conserved within each arrangement, and is thus is a good quantum number. However, presumably, this is scrambled within the complex, so that there appear $K \rightarrow K'$ contributions in Eq. (5.13). Since only the initial arrangement is responsible for the direct contribution, K is conserved in the second summation on the right-hand-side of Eq. (5.13)

The corresponding integral state-to-state cross sections are given by

$$\sigma_{vjF_i\varepsilon\sigma_h \rightarrow v'j'F_i'\varepsilon'\sigma_h'}(E) = \frac{\pi\hbar^2}{2\mu(E - E_{vjF_i\varepsilon})} \frac{1}{2j+1} \sum_J (2J+1) P^J_{vjF_i\varepsilon\sigma_h \rightarrow v'j'F_i'\varepsilon'\sigma_h'}(E)\,, \tag{5.14}$$

Table 5.2: Values of the parameters used in the OH+H calculations

	R_c/a.u.	j_{max}	E_{max}/eV[a]
OH($v = 1, 2$)+H	3	30	1.6
OH($v = 0$)+H	3	25	0.9

[a]The zero of energy corresponds to OH ($r = r_e$)+H.

where μ is the collision reduced mass. Because of the separation in Eq. (5.13) of the overall transition probability into a contribution from direct scattering and a complex-mediated contribution, we can similarly partition the contribution to the cross sections.

Scattering calculations were carried out at nearly 350 values of the total energy ranging from 0.2248 eV to 1.5 eV (1800 cm^{-1}–13,000 cm^{-1}). The zero of energy is taken to be H+OH($r = r_e$), so that this range of total energies corresponds roughly to collision energies ranging from $\approx$ 5–11,000 cm^{-1} in $v = 0$. The parameters which control the accuracy of the computed coupled-states statistical-model cross sections are the capture radius, R_c and the size of the channel basis. The latter is controlled by two parameters E_{max} and j_{max}, so that all OH channels with $j > j_{max}$ or with internal energies $\varepsilon_{vjF_i\varepsilon} > E_{max}$ are excluded. The three parameters R_c, E_{max}, and j_{max} were adjusted to ensure the convergence of the capture probabilities P_c to within 0.5%; the adopted values are listed in Table 5.2. In particular, j_{max} was adjusted so that, at the highest value of the total energy, all open rotational levels as well as the lowest four energetically closed levels were included in the channel basis.

5.3 Results and Discussion

In our investigation of rovibrational relaxation, we shall assume that the initial Λ-doublet levels, which differ in energy by a mere fraction of a wavenumber, are equally populated. In this case the integral cross sections for production of a particular j', F_i' OH final state are obtained from Eq. (5.14) by summing over both final-state Λ-doublet levels and both H-atom spin-projection states, and averaging over the comparable initial states, to obtain:

$$\sigma_{vF_ij\rightarrow v'F_i'j'} = \frac{1}{4}\sum_{\varepsilon\varepsilon'\sigma_h\sigma_h'} \sigma_{vF_ij\varepsilon\sigma_h\rightarrow v'F_i'j'\varepsilon'\sigma_h'}. \tag{5.15}$$

By summing over all final states, we obtain the initially-state-selected, total vibrational relaxation cross sections

$$\sigma_{vF_ij} = \sum_{v'<v,F_i',j'} \sigma_{vF_ij\rightarrow v'F_i'j'}. \tag{5.16}$$

5.3.1 Comparison of Multi-PES and Single-PES Calculations

To understand the effect of the inclusion of the three repulsive PESs, we have performed single-PES calculations for two initial states, $v = 1, j = 0$ and $v = 2, j = 0$ to compare them with the open shell calculations on the multi-PESs with $v = 1, j = 3/2, F_1$, $v = 1, j = 1/2, F_2$, $v = 2, j = 3/2, F_1$ and $v = 2, j = 1/2, F_2$. The single PES cross sections are devided by a factor of 8 in order to account for the electronic degeneracy in comparison to the open shell system:

$$\sigma_{v\rightarrow v'}^{single-PES} = \frac{1}{8}\sum_{j'} \sigma_{v,j=0\rightarrow v',j'}. \tag{5.17}$$

To obtain the cross section for the lowest rotational level on the multi-PESs, we average the initial state specific cross sections from the lowest rotational level of the each spin-orbit manifold as follows

$$\sigma_{v\to v'}^{multi-PES} = \frac{1}{2}\left(\sum_{j'}\sigma_{v,F_1,j=3/2\to v',j'} + \sum_{j'}\sigma_{v,F_2,j=1/2\to v',j'}\right). \tag{5.18}$$

The cross sections calculated in this manner are plotted and compared in Fig. 5.4 and Fig. 5.5. The conclusion we draw is that the inclusion of the multi-PESs are very important at low energy. At higher collision energies ($E_{coll} > 500$ cm^{-1}) cross sections from the multi and single surface simulations behave similarly, with a small difference ($< 10\%$). In the low energy range ($E_{coll} < 200$ cm^{-1}), however, the difference rises to 50%, multi-PES cross sections being bigger. This indicates that the nonadibatic couplings allow more of the incoming partners sample the complex and hence relax. Thus, this effect will gain more and more importance as the collision energy decreases.

5.3.2 Direct as compared to Complex-Mediated relaxation

One of the primary goals of this investigation is to explore the relative importance of direct as compared to complex-mediated mechanisms for vibrational relaxation. Figure 5.6 shows the dependence on collision energy of the initially-state-selected, total vibrational relaxation cross section [Eq. (5.16)] for OH($v = 1, F_1, j = 3/2$). Here, as well as for the $v = 2 \to 0$ and $v = 2 \to 1$ processes (not shown), we found that vibrational relaxation is due overwhelmingly to collisions which enter the HOH$'$ complex and then reemerge. The very small contribution of

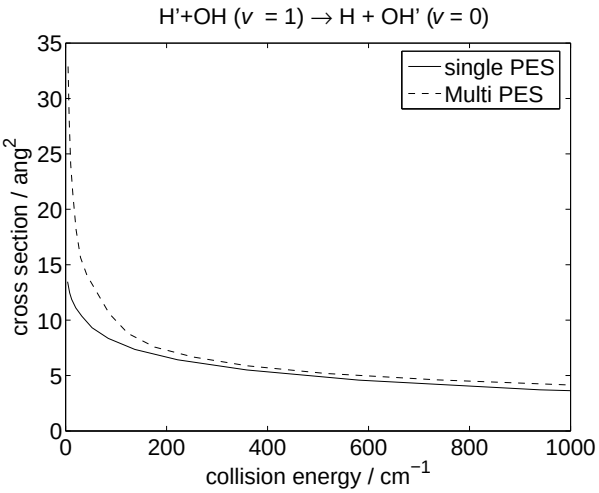

Figure 5.4: Comparison of the relaxation total cross sections with multi and single PESs for $v = 1$ level. The cross sections from the single and multi PES are compared according to the Eq.(5.17) and Eq.(5.18)

direct scattering is even more insignificant at lower energy. (The magnitude of the small rise in the direct cross sections that appears at very low energies is within (or less than) our estimate of the precision of the scattering calculations.)

Figure 5.7 plots the percentage of the direct contribution for the lowest rotational level in both spin-orbit manifolds. The relative importance of direct scattering increases as a function of increasing collision energy, but remains modest even at hyperthermal energies. For vibrational relaxation governed by a repulsive potential energy surface, simple SSH theory [47, 50] predicts that the $v = 2 \rightarrow 1$ cross section will be roughly two times larger than the $1 \rightarrow 0$ cross section. This prediction applies well to the direct relaxation cross sections in Fig. 5.7

Recently, Krems, Nordholm and co-workers have described [162, 163] exact close-coupled calculations of vibrational relaxation cross sections for collisions of

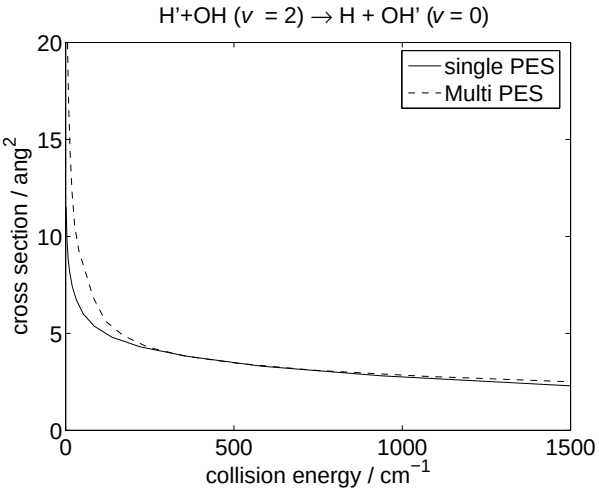

(a)

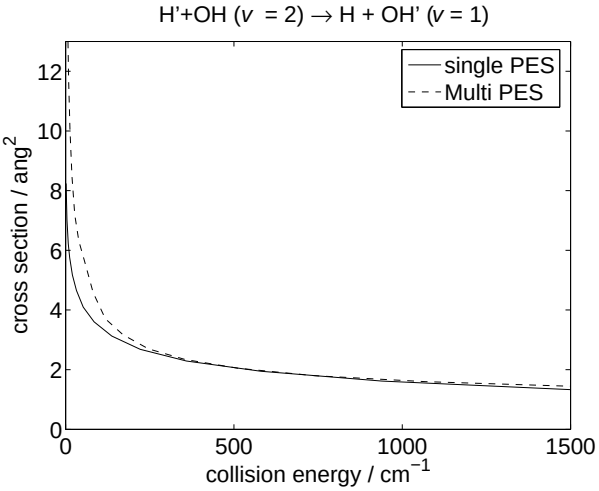

(b)

Figure 5.5: Comparison of the relaxation total cross sections with multi and single PESs for $v = 2$ level (panel a: $v = 2 \rightarrow 0$ and panel b: $v = 2 \rightarrow 1$). The cross sections from the single and multi PES are compared according to the Eq.(5.17) and Eq.(5.18)

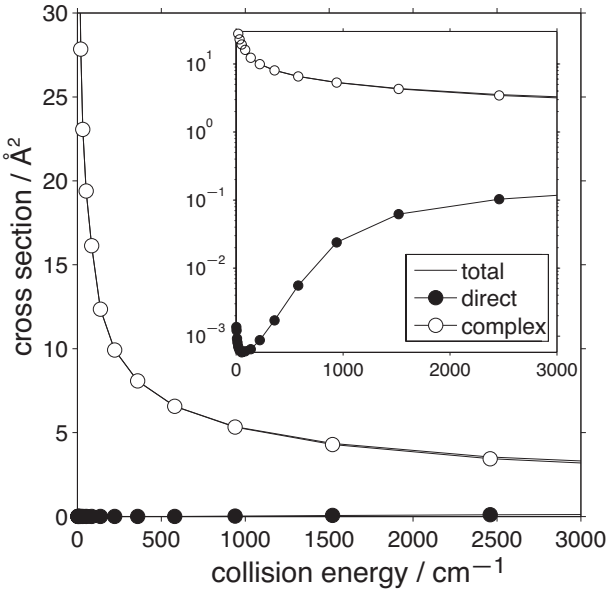

Figure 5.6: Direct and complex-mediated contributions to the initially-state-selected total vibrational relaxation cross section for OH($v = 1, F_1, j = 3/2$) + H $\rightarrow$ OH($v = 0$) + H vibrational relaxation. The inset panel is a semilog plot to demonstrate the negligibly small size of the cross section for direct relaxation.

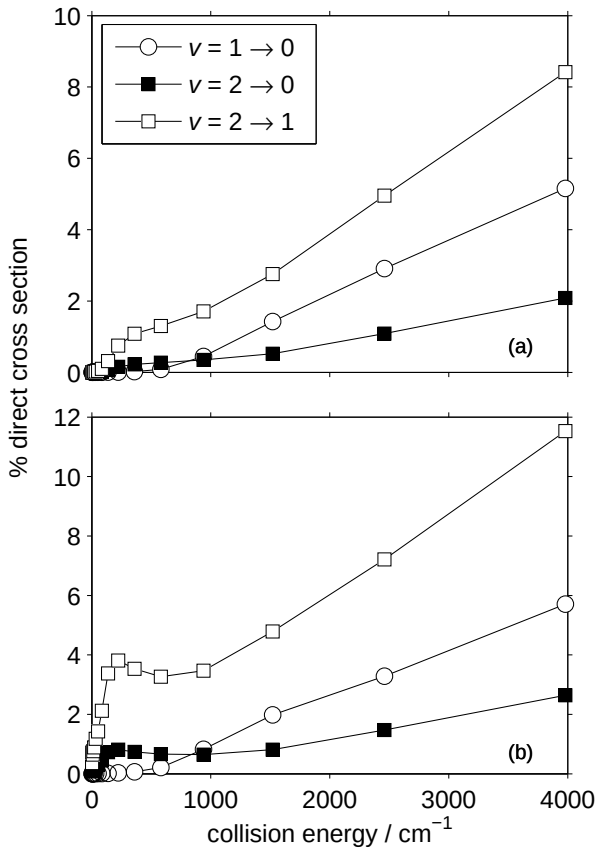

Figure 5.7: The relative percentage contribution of direct scattering to the vibrational relaxation cross sections as a function of collision energy for the lowest rotational levels of OH (panel a: $j = 3/2$, F_1 and panel b: $j = 1/2$, F_2.)

the closed-shell HF–Ar system. Their computed cross sections are on the order of $10^{-4} - 10^{-3}$Å^2 at collision energies below several thousand cm^{-1}. As might be expected, these values are very comparable to the direct vibrational relaxation cross sections shown in Fig. 5.6.

5.3.3 Initial state selected relaxation cross sections

Figure 5.8 shows the initial state specific total cross sections calculated as described in Eq. 5.16 for relaxation of OH($v = 1$). As reported previously, [92, 126, 164] initial OH rotational excitation decreases the capture cross sections. The topology of the $^1A'$ OH–H potential energy surface – strongly attractive only in bent geometries, but quite repulsive for both collinear geometries [94] – is responsible for this effect. The rotational motion averages out the OH–H potential, so that the incoming collision partners "see" less of the collision complex. Hence, the magnitude of the cross sections as well as the magnitude of the enhancement at low-energy decreases with increasing j. At higher energy, this effect disappears, because the collision occurs too quickly for the rotational averaging to occur.

We observe a smaller relaxation cross section for the spin-orbit excited OH. However, the decrease in the vibrational relaxation cross section with increasing initial rotational angular momentum, discussed in the preceding paragraph, is apparent also in the upper spin-orbit manifold. Both these conclusions apply also to $v = 2 \rightarrow 1$, 0 relaxation.

Figure 5.9 compares the overall vibrational relaxation cross sections for the

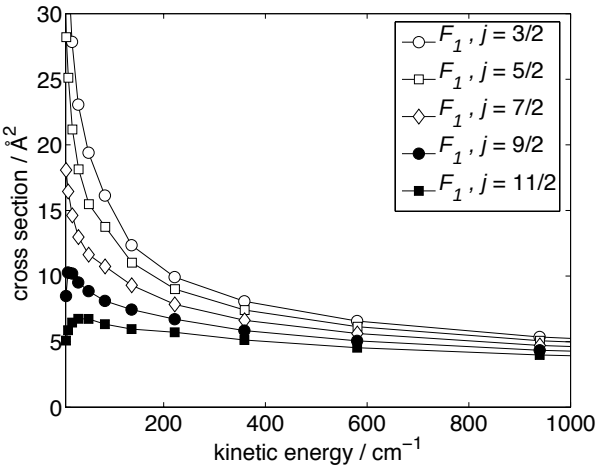

(a) OH($v = 1, F_1, j$)+H→OH($v = 0$)+H

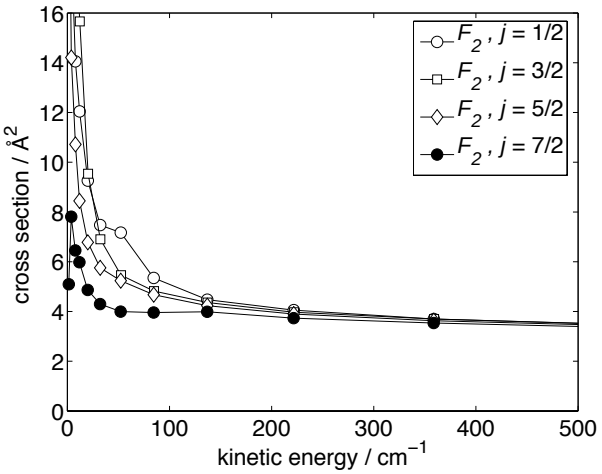

(b) OH($v = 1, F_2, j$)+H→OH($v = 0$)+H

Figure 5.8: Initial rotational and spin-orbit resolved cross sections for OH ($v = 1, F_1/F_2, j$) + H → OH ($v = 0$) + H. Cross sections are calculated as described in Eq. 5.16.

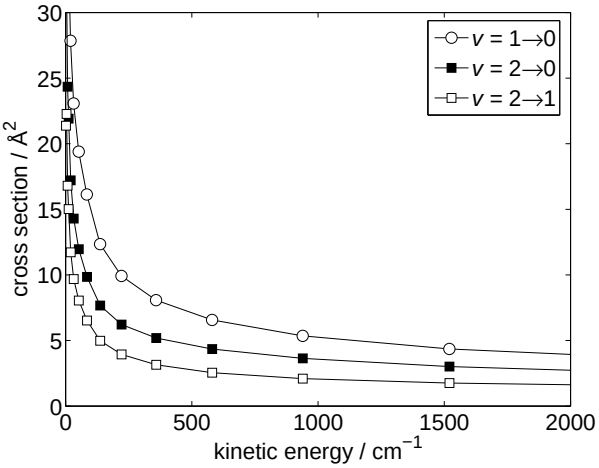

Figure 5.9: Initial state selected relaxation total cross sections for OH($v, F_1, j = 3/2$) + H $\rightarrow$ OH(v')+H, for $v = 2 \rightarrow 1$, $2 \rightarrow 0$, and $1 \rightarrow 0$.

$v = 2 \rightarrow 1$, $2 \rightarrow 0$, and $1 \rightarrow 0$ transitions, as a function of energy. We observe that the $v = 1 \rightarrow 0$ process has the largest cross section. If we neglect the small direct contribution to the relaxation in Eq. (5.13), then, we see that the probabilities for the $v = 2 \rightarrow 1$, $2 \rightarrow 0$, and $1 \rightarrow 0$ transitions are given by

$$P_{\mathrm{v=1\rightarrow 0}} = \frac{P_{\mathrm{v=1}} P_{\mathrm{v=0}}}{\sum P_{\mathrm{v=1}} + \sum P_{\mathrm{v=0}}} \,, \tag{5.19}$$

$$P_{\mathrm{v=2\rightarrow 0}} = \frac{P_{\mathrm{v=2}} P_{\mathrm{v=0}}}{\sum P_{\mathrm{v=2}} + \sum P_{\mathrm{v=1}} + \sum P_{\mathrm{v=0}}} \,, \tag{5.20}$$

and

$$P_{\mathrm{v=2\rightarrow 1}} = \frac{P_{\mathrm{v=2}} P_{\mathrm{v=1}}}{\sum P_{\mathrm{v=2}} + \sum P_{\mathrm{v=1}} + \sum P_{\mathrm{v=0}}} \,. \tag{5.21}$$

Because the total energy is higher for collisions with OH initially in $v = 2$, the denominator is larger in the expressions for relaxation out of $v = 2$ [Eqs. (5.20) and (5.21)]. If we assume that the capture cross sections are roughly equal for $v = 2$, 1, and 0, then the $v = 1 \rightarrow 0$ relaxation probabilities will be larger.

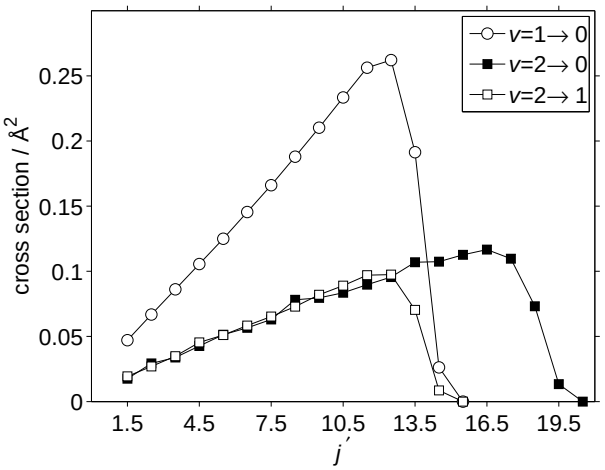

Figure 5.10: Comparison of the state-to-state cross sections for OH($v, F_1, j = 3/2$) + H $\rightarrow$ OH(v', F_1, j')+H for a collision energy of 580.3 cm^{-1}.

Figure 5.10 shows the dependence on final rotational quantum number at a collision energy of 580.3 cm^{-1} for the $v = 2 \rightarrow 1$, $2 \rightarrow 0$, and $1 \rightarrow 0$ transitions. The $v = 2 \rightarrow 1$ and $v = 2 \rightarrow 0$ cross sections are virtually identical, except at high j', where only rotational levels in $v = 0$ are energetically accessible. Consequently, when summed over all final rotational levels, the $v = 2 \rightarrow 0$ cross sections will be larger than the $v = 2 \rightarrow 1$ cross sections at an identical collision energy, as seen in Fig. 5.9.

Consequently, it is clear that complex-mediated vibrational relaxation results in very different propensity rules than direct relaxation. As discussed earlier, and seen in Fig. 5.7, for direct processes, simple SSH theory [47, 50] predicts much larger cross sections for $v \rightarrow v-1$ as compared to $v \rightarrow v-2$ transitions, and, furthermore, that the cross sections for $v \rightarrow v-1$ transitions will increase as a function of the initial vibrational quantum number.

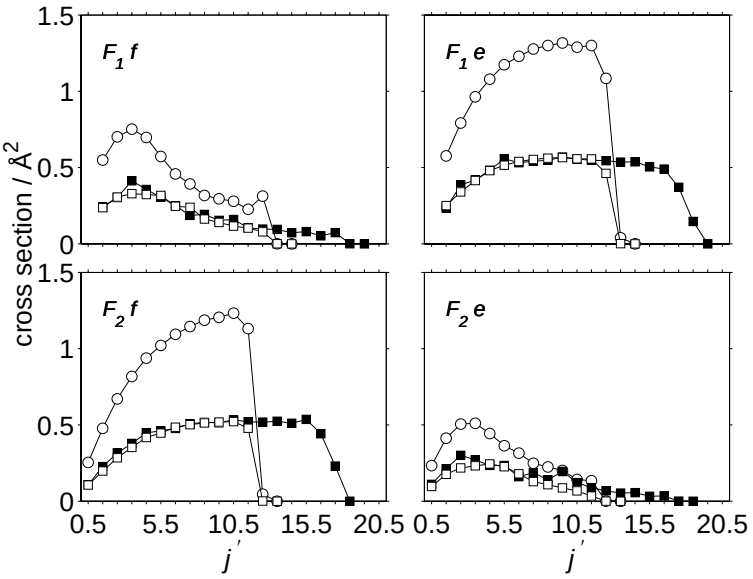

Figure 5.11: State-to-state OH($v, F_1, j = 3/2$)+H→OH($v', F_i', j', \varepsilon'$)+H cross sections at a collision energy of 12 cm^{-1}. As in Fig. 5.10 the open cirles, filled squares, and open squares designate, respectively $v = 1 \rightarrow 0$, $v = 2 \rightarrow 0$ and $v = 2 \rightarrow 1$ processes.

5.3.4 Final State Populations

Figures 5.11 and 5.12 show the dependence on the final rotational, spin-orbit, and Λ-doublet state of the cross sections for $v = 2 \rightarrow 1$, 0 and $v = 1 \rightarrow 0$ relaxation at both very low and high collision energies (E_c = 12 cm^{-1} and 1520 cm^{-1}). We observe that relaxation to the $\Pi(A')$ levels exhibits the "prior" like dependence on the final rotational quantum number,[89, 94, 121, 164] expected for a statistical mechanism. However, at E_c = 12 cm^{-1} (and, in fact, at all collision energies below $\approx$ 800 cm^{-1}) the cross section for production of OH products in the $\Pi(A'')$ rotational levels are smaller in magnitude and do not display a similar "prior"-like shape. As

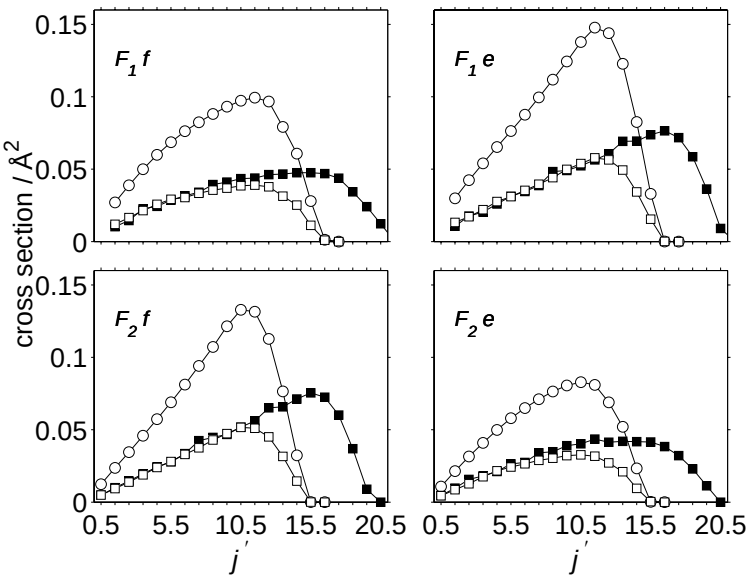

Figure 5.12: State-to-state OH$(v, F_1, j = 3/2)$+H$\rightarrow$OH$(v', F_i', j', \varepsilon')$+H cross sections at a collision energy of 1520.3 cm^{-1}. As in Fig. 5.10 the open cirles, filled squares, and open squares designate, respectively $v = 1 \rightarrow 0$, $v = 2 \rightarrow 0$ and $v = 2 \rightarrow 1$ processes.

discussed in our earlier paper on the $O(^1D)+H_2 \rightarrow OH+H$ reaction, [94] decay of the HOH complex leads preferentially to OH products in the $\Pi(A')$ Λ-doublet levels. Production of the $\Pi(A'')$ Λ-doublet levels are a result of curve crossing as the OH–H fragments recede.

Further, in our earlier study [94] of the $O+H_2 \rightarrow OH+H$ reaction we observed that the OH products in $\Pi(A')$ Λ-doublet levels were produced with a significantly larger degree of rotational excitation than the products in the $\Pi(A'')$ Λ-doublet levels. This is exactly what is seen here. As we might have anticipated, the rotational and Λ-doublet distributions are very similar for OH produced from reaction or by vibrational relaxation. Within a statistical model, at a given total energy the decay of the HOH complex will give identical product distributions, regardless of whether the complex is formed by the $O(^1D)+H_2$ reaction or by collision of vibrationally excited OH with H.

We observe in Fig. 5.12 that at higher initial collision energy the propensity toward production of products in the $\Pi(A')$ Λ-doublet levels is still present, although less pronounced. In addition, at this higher energy the product rotational distributions associated with both Λ-doublet levels show a "prior"-like shape.

5.3.5 Vibrational Relaxation Rate Constants

If we assume a Maxwellian distribution of translational energy at temperature T, the thermal rate constant is given by [127]

$$k_{i\rightarrow f}(T) =< v\sigma_{i\rightarrow f} >= \left[\frac{8}{\pi\mu(kT)^3}\right]^{1/2} \int_0^\infty E_c \; \sigma_{i\rightarrow f}(E_c) \; exp(-\frac{E_c}{kT}) \, dE_c \,, \qquad (5.22)$$

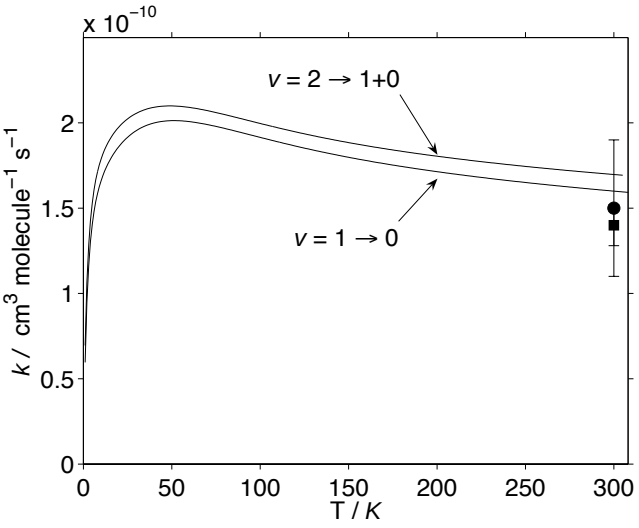

Figure 5.13: Comparison of thermally averaged vibrational removal rate constants for OH($v = 1, 2$)+H. The experimental $v = 1$ room temperature value is from Reference [55]. The filled circle and filled square designate rate constants derived from experiments in which H_2O was excited, respectively, to the $|13>$ or $|12>$ vibrational level before photolysis.

where v is the initial relative velocity, and E_c the initial translational energy (collision energy), for the OH reactant in initial state i. Here, the indices i and f designate the full set of initial and final quantum numbers $\{vjF_i\varepsilon\}$. The overall thermal rate constant, for the OH reactant in initial state i, is obtained by summing over all energetically accessible product states, namely

$$k_i(T) = \sum_f k_{i\to f}(T) \ . \tag{5.23}$$

The overall thermally-averaged rate constant for the title reaction is then obtained by averaging over an assumed Boltzmann distribution of OH rotational levels,

$$k(T) = \frac{\sum_i g_i \exp(-\varepsilon_i/kT) k_i(T)}{Q}. \tag{5.24}$$

Here $Q(T)$ is the partition function and g_i and ε_i designate, respectively, the degeneracy and internal energy of the i^{th} state of the OH reactant. The sum in Eq. (5.24) runs over both spin-orbit manifolds.

Figure 5.13 shows the temperature dependence of the thermally-averaged $v = 1 \to 0$ vibrational relaxation rate constant. The experimental values [55] of the room temperature $v = 1 \to 0$ rate constant are also shown. In the experiment, vibrationally excited OH is produced by photolysis of water, itself initially vibrationally excited. We assume that rotational relaxation of the nascent OH photolysis products will be rapid compared to vibrational relaxation, so that a comparison can be made with our thermally-averaged rate constants. The agreement between our calculated $v = 1 \to 0$ rate constant and the earlier experimental values [55] is excellent. We see from Table 5.1 that the earlier calculations of Quack and Troe [145]

predict room temperature vibrational relaxation rate constants which are somewhat higher.

Figure 5.13 also compares the temperature dependence of the thermally averaged rate constants for vibrational removal (deactivation) of the $v = 1$ and $v = 2$ vibrational levels. The latter includes both the $v = 2 \rightarrow 1$ and $v = 2 \rightarrow 0$ processes. In atmospheric modelling, this vibrational removal rate constant is an important parameter [142]. We observe that the total vibrational removal rate for the $v = 2$ manifold is slightly larger than for $v = 1$. The temperature dependence of the two vibrational removal rates is, however, very similar. In answer, then, to the question raised in the Introduction, we predict, at least for the $v = 1$ and $v = 2$ levels, that the overall vibrational removal rate will depend but little on the initial vibrational quantum number.

5.3.6 Rotational Excitation and Λ-doublet Inversion

As mentioned in the Introduction, the importance of the OH astronomical maser has stimulated considerable discussion about the role of rotationally inelastic collisions in either producing or destroying the population inversion that is responsible for maser emission [35–38]. In an attempt to investigate collisional pumping mechanisms, some 25 years ago Shapiro and Kaplan (SK) presented theoretical calculations of rotational excitation rate constants for the OH+H systems [161]. These calculations were based on earlier *ab initio* potential energy surfaces for the $^1A'$ and $^3A''$ states. Shapiro and Kaplan made additional approximations for the po-

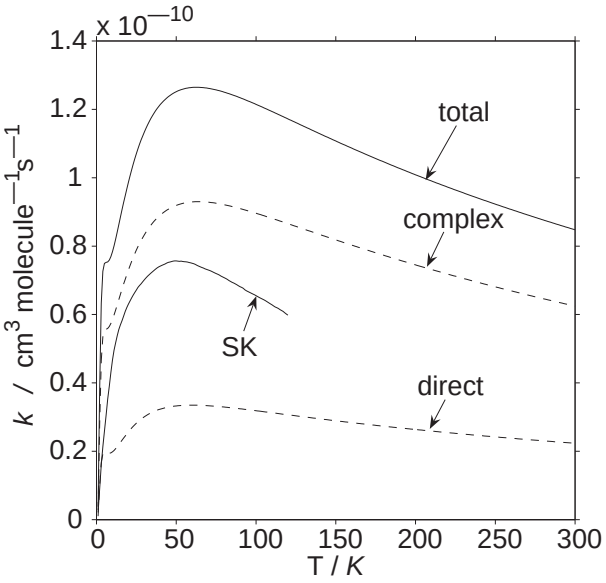

Figure 5.14: State-to-state thermal rate constant for the transition between the two Λ-doublet levels of the ground rotational level (j=3/2, F_1).

tential surfaces for the $^3A'$ and $^1A''$ states, which were not then available. Cross sections were obtained within the exponential Born approximation. These limitations, both in the treatment of the dynamics and the description of the potential energy surfaces, can now be overcome. With the availability of high-quality *ab initio* potential energy surfaces for all four OHH states, [94] we present here the results of coupled-states statistical calculations for rotational excitation of OH($v = 0$) for 1.5 $\text{cm}^{-1} < E_c < 795$ cm^{-1}.

Our formulation of the OH+H system does not include the nuclear spin quantum number, $\mathcal{F}$. For comparison,then, we sum and average the hyperfine-resolved rate constants reported by Shapiro and Kaplan over the nuclear spin quantum num-

ber:

$$k_{jF_1\varepsilon\to j'F'\varepsilon'} = \frac{1}{2}\sum_{\mathcal{F}\mathcal{F}'} k_{jF_1\varepsilon\mathcal{F}\to j'F'\varepsilon'\mathcal{F}'}. \tag{5.25}$$

We then compare these rate constants with those from the present calculations, summed and averaged over the H-atom spin-states, namely

$$k_{jF_1\varepsilon\to j'F'\varepsilon'} = \frac{1}{2}\sum_{\sigma_h\sigma_h'} k_{jF_1\varepsilon\sigma_h\to j'F'\varepsilon'\sigma_h'}. \tag{5.26}$$

At low temperature, the largest relaxation rate constant is associated with Λ-doublet changing transitions within a given rotational level. It is this processes which lead to thermalization of a non-equilibrium Λ-doublet population. The temperature dependence of the rate constant for the Λ-doublet changing transition within the lowest ($j = 3/2$, F_1) level is shown in Figure 5.14. In contrast to the case of vibrational relaxation, discussed earlier in this paper, the direct and capture processes make a roughly equal contribution here.

Despite the approximations made by Shapiro and Kaplan to both the OH+H potential energy surfaces and in their treatment of the scattering dynamics, we observe that the magnitude and temperature dependence of their calculated rate constant agrees reasonably well with our present calculation. Within the interstellar cloud model they adopted, Shapiro and Kaplan concluded that for most reasonable H-atom densities even a collisional rate on the order of 10^{-10} cm^3 molelcule^{-1} sec^{-1} is not large enough to thermalize effectively a non-equilibrium Λ-doublet population in the $j = 3/2$, F_1 level.

Figure 5.15 shows the temperature dependence of the four possible $\varepsilon \to \varepsilon'$ transitions corresponding to $j = 3/2 \to 5/2$ rotational excitation in the lower (F_1)

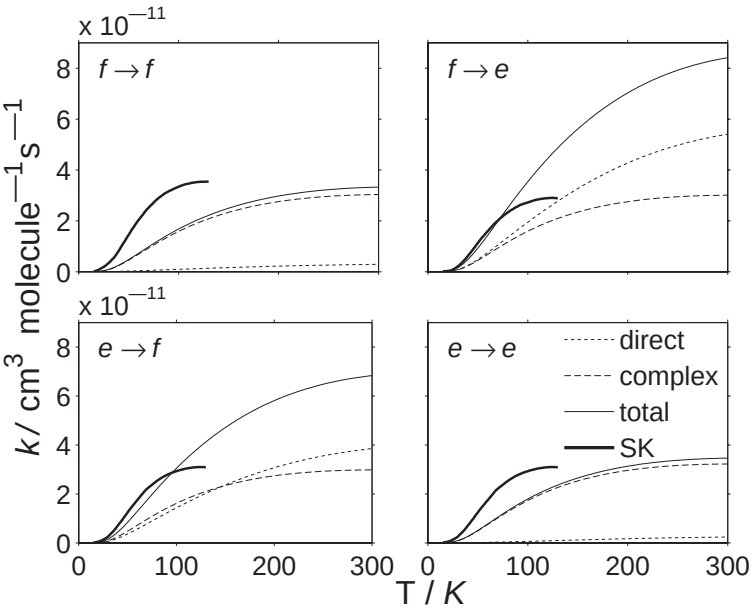

Figure 5.15: State-to-state direct, complex-mediated and total rate constants for the OH($j = 3/2, F_1, \varepsilon$)+H→OH($j' = 5/2, F_1, \varepsilon'$) transition within the $v = 0$ manifold. The heavy solid curves depict the results of Shapiro and Kaplan (Ref. [161]).

spin-orbit manifold. We observe a large difference between the rate constants for the ε-changing as compared to ε-conserving transitions. As seen in the figure, the much larger contribution of direct scattering to the ε-changing transitions results in a larger total rate constant. This ε, ε' propensity seen in the rate constants – and in the underlying cross sections (not shown) – is entirely similar to the propensities seen earlier in collisions of molecules in $^2\Pi$ electronic states with closed-shell atomic collision partners [165–167]. These propensities are a reflection of the contribution of different components in the anisotropy in the potential energy surface to the coupling between two levels of the same ($e \rightarrow e$ or $f \rightarrow f$) as opposed to opposite ($e/f \rightarrow f/e$) symmetry index.

We also observe in Fig. 5.15 that the degree of variation of the rotational excitation cross section with the e/f index predicted by the present calculations is much larger than predicted by the earlier calculations of Shapiro and Kaplan.[161] In addition, the rate constants determined by Shapiro and Kaplan predict, in direct contrast to the present calculations, that the e/f conserving transitions will be more efficient than the e/f changing transitions.

In comparison with the direct contributions, the complex-mediated contributions to the cross sections (not shown) and rate constants (Fig. 5.15) are virtually insensitive to the initial and final Λ-doublet indices. The capture cross sections are largely determined by the overall topology of the attractive $^1A'$ potential energy surface. Any variation with ε of the capture cross sections for a particular jF_i will reflect the differing degree to which the e and f Λ-doublet states will access the $^1A'$ potential energy surface. This difference is likely to be small. Figure 5.16 plots the

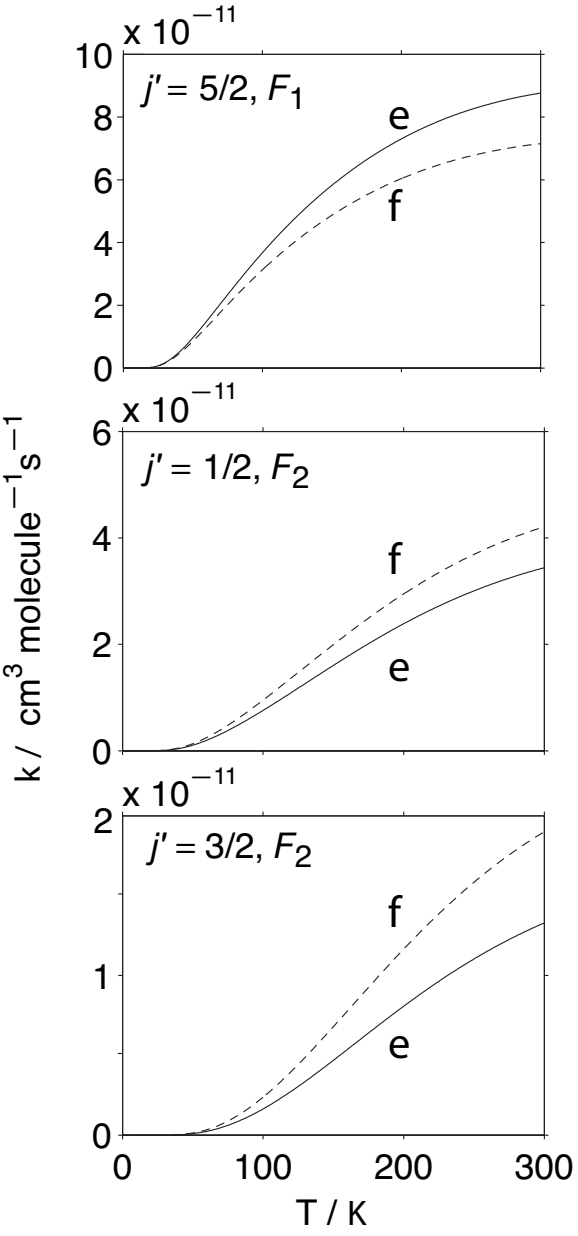

Figure 5.16: Initial e/f-averaged rate constants for transitions out of the OH($v = 0, F_1, j = 3/2$) level into both Λ-doublet levels for $j' = 5/2, F_1$, $j' = 1/2, F_2$ and $j' = 3/2, F_2$.

rate constants for collisional excitation from the $j = 3/2, F_1$ level (with an assumed equal population in the two $\Lambda-$doublets), to the next rotational level ($j = 5/2$) in the lower (F_1) spin-orbit manifold as well as into the $j = 1/2$ and $j = 3/2$ levels of the higher (F_2) spin-orbit manifold. We observe, referring back to Fig. 5.3, that collisional excitation will not lead to population inversion in the former case, but will lead to population inversion in the spin-orbit changing processes. The calculated e/f collisional propensity supports the proposed maser-pumping mechanism mentioned in the Introduction, [35–38, 157, 168] whereby if collisional excitation populates preferentially the upper Λ-doublet, then subsequent radiative transitions to the ground rotational level, which by necessity change the parity but conserve the Λ-doublet label, will provide a pump mechanism for the maser. However, for collisions of OH with molecular hydrogen (H_2) the most recent, [159] as well as earlier, [157] calculations predict, in contrast to the present calculations (OH+H), that collisions out of the $j = 3/2$, F_1 level, averaged over both initial Λ-doublets, will not result in a population inversion in the lower rotational levels of the F_2 spin-orbit manifold.

5.4 Summary

We have performed a close-coupled, statistical study of vibrational and rotational relaxation of OH($^2\Pi$) in collisions with H atoms. The method and Hamiltonian include all couplings exactly in the long-range part of the potential, but treats formation and decay of the HOH complex region statistically. Our calculations al-

low us to separate the contributions to vibrational and rotational relaxation due to inelastic scattering involving both the repulsive regions of the $^1A'$ potential energy surface as well as coupling between the $^1A'$ potential energy surface and the repulsive $^1A''$, $^3A'$, and $^3A''$ potential energy surfaces from processes which enter the HOH complex and then re-emerge into different internal states of the OH moiety. We found that the direct and complex-mediated mechanisms make comparable contributions to rotationally inelastic processes. However, for vibrationally-inelastic processes, where the direct contribution is extremely small, the complex-mediated contribution remains large. Thus, as Smith has suggested, [136] vibrational relaxation in radical-radical encounters by means of complex-forming collisions can be a far more efficient process than in the case of closed-shell collision partners.

At 300 K, the total rate constant for removal from OH($v = 2$) (1.697×10^{-11} cm^3 molecule^{-1} s^{-1}) is slightly higher than for removal from OH($v = 1$) (1.600 in the same units). The $v = 1$ calculated removal rate constant agrees extremely well with earlier experimental measurements from the Smith group, [55] but is somewhat smaller than the earlier predictions of Quack and Troe [145].

Because the complex-mediated mechanism dominates, our calculations also predict that vibrational relaxation will lead to rotationally hot OH products. In addition, and entirely similar to our earlier study of OH produced by the O(^1D)+H_2 reaction, [94]we predict that the relaxed OH will be found preferentially in the $\Pi(A')$ Λ-doublet level. Observations of atmospheric OH, produced in reactions (5.1) and (5.2), show a markedly larger population in the $\Pi(A')$ Λ-doublet levels [142]. Although collisions with H may not play a major role in the vibrational relax-

ation of OH in the mesosphere, the results of the present study certainly suggest that complex-mediated vibrational relaxation, through collisions with other radicals (possibly O atoms), could well result in the observed inequalities in the Λ-doublet populations.

Our calculations also predict that, at least for relaxation of OH due to collisions with H, the vibrational removal rate will be insensitive to the initial vibrational quantum number, in contrast to the predictions of SSH theory.

We also investigated rotationally inelastic collisions in the $v = 0$ manifold as a possible contributor to population inversion within the Λ-doublet of the lowest ($j = 3/2$, F_1) rotational level of OH in interstellar gas clouds. Our calculations, which are free of the approximations which limited the much earlier work of Shapiro and Kaplan, [161] suggest that collisional excitation to the upper spin-orbit manifold, F_2, followed by radiative relaxation to the ground rotational level in the F_1 manifold, will lead to this population inversion. Along with the considerable body of theoretical work on rotationally-inelastic collisions of OH with H_2, [155–157, 159, 160] the present calculations on collisions of OH with H should provide insight and input into modelling of the pump mechanism of the OH maser in astronomical environments, where both OH and H are both abundant. This can occur, for example, in dense molecular clouds that are subject to fast interstellar shock waves [169].

Chapter 6

Conclusions

This thesis has reported the *ab initio* study of the $O(^3P)-H_2$ system as well as statistical, close-coupled reaction dynamics studies of $OH(^2\Pi)$+D and $OH(^2\Pi)$+H collisions.

In Chapter 2 we reported PESs for the $O(^3P)-H_2$ system determined using RCCSD(T) and MRCI methodology. The accuracy of the MRCI+Q results extrapolated to the CBS limit were assessed in comparison to RCCSD(T) calculation with an aug-cc-pVQZ basis with additional bond functions. The results showed very good agreement. Based on these results, we predict the overall van der Waals minimum to be in perpendicular geometry, and located at a closer distance than a secondary well in collinear geometry. Our calculation corroborates the earlier results of Alexander [23], but disagrees with an earlier report of Li [22] as well as with recently refitted surfaces of Brandão and coworkers. [21] Our RCCSD(T) calculations with an aug-cc-pVQZ basis including a set of bond functions are expected to recover the major fraction of the dispersion energy which is responsible for the van der Waals minima. Therefore, we have confidence in the geometries and well depths predicted.

One shortcoming of the PESs presented here is the lack of angular dependence since we looked only at collinear and perpendicular orientations. Klos sug-

gested [170] that one could exploit the symmetry of the H_2 molecule to attain the interaction energies in C_s geometries from the C_{2v} and $C_{\infty v}$ values. Hence, based on the data presented in this dissertation, it should be possible to derive the angular dependence in this way.

The spin-orbit coupling terms for the $O(^3P)-H_2$ system are calculated by an *ab initio* implementation of the Breit-Pauli Hamiltonian. The geometry dependence of the spin-orbit terms in the van der Waals region is very weak. However, an accurate description of the barrier of the surfaces requires the calculation of spin-orbit coupling terms if one wants to obtain a very accurate description of the barrier.

The major portion of section in this dissertation is focused on the application of the recently proposed statistical, coupled-states method of Rackham *et al.* [89, 90, 94] to the electronically identical, complex forming reactions: OH + D $\rightarrow$ OD + H and $OH(v, j)$ + H $\rightarrow$ $OH(v', j')$ + H.

In Chapter 4, we have reported state-to-state cross sections and thermal rate constants for the D+$OH(X^2\Pi)$$\rightarrow$$OD(X^2\Pi)$+H isotope exchange reaction. We observed a negative temperature dependence of the thermally averaged rate. The state selected rate constants reveal that this behavior is due primarily to the thermal averaging over the rotationally accessible states. At 300 K we predict $k(T) = 10.78 \times 10^{-11}$ $cm^3molecule^{-1}s^{-1}$. At lower temperature ($T \leq 50K$) the value rises to $k(T) = 15 \times 10^{-11}$ $cm^3molecule^{-1}s^{-1}$, comparable to the value assumed by Croswell and Dalgarno in their modelling investigation of the abundance of interstellar OD. [34]

Our calculations predict that OD from the isotope exchange reaction will be

produced in the energetically lower Λ-doublet level, except, however, for the $j = 1/2 - 7/2$ levels of the upper (F_2) spin-orbit manifold. Thus, OD masing for OD produced by the OH + D $\rightarrow$ OD +H reaction, might occur for these latter levels. Although the OD molecule has not yet been detected in interstellar clouds, [129] we do encourage further searches, particularly for the five lowest rotational levels of the upper spin-orbit manifold.

Chapter 5 is a close-coupled, statistical study of vibrational and rotational relaxation of OH($^2\Pi$) in collisions with H atoms. Our calculations allow us to separate out the contributions to vibrational and rotational relaxation due to direct inelastic scattering. This process involves, both the repulsive regions of the $^1A'$ PES as well as coupling between the attractive regions of $^1A'$ PES and the repulsive $^1A''$, $^3A'$, and $^3A''$ PESs. We also determine the contribution due to processes which enter the HOH complex and then re-emerge into different internal states of the OH moiety. We found that direct and complex-mediated mechanisms make comparable contributions to rotationally inelastic processes. However, for vibrationally-inelastic processes, where the direct contribution is extremely small, the complex-mediated contribution remains large. Thus, as Smith has suggested, [136] vibrational relaxation in radical-radical encounters by means of complex-forming collisions can be a far more efficient process than in the case of closed-shell collision partners. The $v = 1$ calculated removal rate constant agrees extremely well with earlier experimental measurements from the Smith group [55].

The SSH theory [50] predicts that vibrational relaxation rates will be dependent on the initial vibrational level, such that relaxation rate increases as the initial

vibrational level quantum number, v, increases. In contrast, in complex-mediated vibrational relaxation, we observed that the overall relaxation rate is almost independent of initial vibrational level. For OH + H collisions we observed that the relaxation rate from the $v = 2$ level is only slightly higher than from the $v = 1$ level. The other significant difference of complex-mediated relaxation from the predictions of the SSH theory is the dependence of relaxation rate on the amount of vibrational quantum transfered, Δv. According to SSH theory $\Delta v = \pm 1$ processes have the highest relaxation rate. Here, at least for OH + H collisions, we observed that $v = 2 \rightarrow 0$ relaxation is faster than the $v = 2 \rightarrow 1$ relaxation. This indicates that the relaxation rate in collisions where a long-lived complex is formed is not proportional to a coupling matrix element between the initial and final vibrational wave functions of OH, as used in SSH theory. Rather, relaxation happens by the scrambling of motion in the complex region.

However, we should take caution that the generalizations we made in the previous paragraph are based on an analysis including only the three lowest vibrational levels of the OH molecule. In order to establish and generalize these differences from regular inelastic collisions leading to vibrational relaxation, it will be necessary to include higher vibrational levels in the simulation. In this case, the $O(^1D)$+H_2 channel as well as higher electronic levels might be involved leading to a more complicated picture, with the possibility of electronic quenching, $OH(^2\Pi, v > 11) + H \rightarrow OH(A^2\Sigma^+) + H$ or reaction, $OH(^2\Pi, v > 1) + H \rightarrow O(^3P) + H_2$ or $OH(^2\Pi, v > 3) + H \rightarrow O(^1D,^3P) + H_2$. The product channel $O(^3P) + H_2$, although open for $v \geq 1$, is not included in our simulations. Because of the high reaction barrier in

the $O(^3P)$ + H_2 interaction, it is not possible to employ the statistical methods for this channel. A future study including higher vibrational as well as the accessible electronic states, we believe, would help to clarify the dependence of relaxation rate on the initial vibrational level.

Because complex-mediated mechanism dominates, our calculations also predict that vibrational relaxation will lead to rotationally hot OH products. In addition, we predict that the relaxed OH will be found preferentially in the $\Pi(A')$ Λ-doublet level. This result is similar to our predictions for the isotope exchange reaction presented in Chapter 4. Although collisions with H may not play a major role in the vibrational relaxation of OH in the mesosphere, the results of the present study certainly suggest that complex-mediated vibrational relaxation, through collisions with other radicals (possibly O atoms), could well result in the observed [142] inequalities in the OH Λ-doublet populations.

We also investigated rotationally inelastic collisions in the $v = 0$ manifold as a possible contributor to population inversion within the Λ-doublet of the lowest ($j = 3/2$, F_1) rotational level of OH in interstellar gas clouds. Our calculations suggest that collisional excitation to the upper spin-orbit manifold, F_2, followed by radiative relaxation to the ground rotational level in the F_1 manifold, will lead to this population inversion, as suggested by Andresen [38] The calculations can be extended to the determination of state-to-state rate constants for all these vibrational and rotational states which are important in the modeling of the pump mechanism of OH maser in the interstellar medium.

We also analyzed the effect of multiple PESs on the relaxation cross sections

in comparison to single PES calculation. Our analysis showed that an accurate description of the low energy collisions requires the inclusion of multiple PESs. On the other hand, in the energy averaging which is included in the calculation of single as compared to multiple PES cross sections, the difference at low energy may not make a large contribution to thermal rate constants at room temperature.

In conclusion, the most important contributions of this thesis are three fold. Firstly, the application of the statistical method to rotational and vibrational relaxation in complex-mediated collisions provided a quantitative assessment of the role of the direct scattering in comparison to the complex-mediated relaxation processes. We have found that complex-mediated vibrational relaxation is much more facile than the direct vibrational relaxation especially at low energy. The importance of direct scattering increases at higher energy where the repulsive wall of the PESs become more important. Our results show that the lowest $v = 1$ and $v = 2$ vibrational levels have similar total removal cross sections and that the prediction of SSH theory concerning the dependence on the vibrational quantum number does not apply to complex-mediated collisions.

The second contribution is related to the accurate calculation of rate constants. We have used the statistical model to obtain thermal rate constants so that we can directly compare with the available experimental data. By conventional scattering methods, calculation of thermal rate constants for complex-mediated reactions is a formidable task. The calculated thermal relaxation rates for OH + H system showed a negative temperature dependence due to the thermal averaging over the initial rotational levels. The studies in this thesis have shown that the statistical

close-coupled method which includes nonadiabatic effects can be extended to study rotational and vibrational relaxation processes in other complex-mediated collisions successfully, for ultimate use in modeling relaxation processes in atmospheric and interstallar chemistry.

Appendix A

$O+H_2$ Entrance Channel Data

A.1 RCCSD(T) Data

Table A.1: RCCSD(T) interaction energies for the $O(^3P)-H_2$ system as a function of the Jacobi coordinate R ($\theta = 0^o$ and $r = 1.402$ a.u.).

R/ a.u.	$^3\Sigma$/ cm^{-1}	$^3\Pi$/ cm^{-1}
11.00	−0.18	−5.93
10.00	−0.76	−10.17
9.00	−2.29	−18.40
8.50	−3.82	−25.18
8.00	−6.20	−34.57
7.50	−9.70	−47.00
7.00	−14.23	−61.60
6.50	−17.95	−73.10
6.40	−18.14	−73.84
6.30	−17.95	−73.60
6.25	−17.67	−73.02
6.10	−15.88	−68.92
6.00	−13.65	−63.67
5.75	−2.52	−37.61
5.50	21.30	17.20
5.25	66.84	119.87
5.00	148.34	300.43
4.50	515.15	1106.08
4.25	874.99	1909.86
4.00	1420.78	3177.32
3.75	2210.08	5145.41
3.50	3286.04	8158.12
3.00	6374.68	19496.11

Table A.2: RCCSD(T) interaction energies for the O(^3P)−H_2 system as a function of the Jacobi coordinate R ($\theta = 90^o$ and $r = 1.402$ a.u.).

$R/a.u.$	$^3B_1$/ cm^{-1}	$^3B_2$/ cm^{-1}	$^3A_2$/ cm^{-1}
11.00	−3.02	−2.11	−0.17
10.00	−5.22	−3.78	−0.75
9.00	−9.64	−7.20	−2.20
8.50	−13.42	−10.18	−3.42
8.00	−18.99	−14.59	−4.95
7.50	−27.15	−21.08	−6.20
7.00	−38.89	−30.29	−4.96
6.50	−54.75	−42.18	5.35
6.25	−63.83	−48.43	18.77
6.00	−72.79	−53.72	42.90
5.75	−80.07	−56.15	84.61
5.50	−82.76	−52.37	154.80
5.25	−75.81	−36.55	270.54
5.00	−50.76	0.88	458.34
4.80	−8.73	56.47	687.35
4.50	116.14	211.17	1235.75
4.25	311.97	445.70	1983.39
4.00	641.46	834.75	3145.78
3.75	1171.97	1459.53	4937.40
3.50	1993.94	2434.61	7674.91
3.00	4999.61	6120.21	18021.43

A.2 Spin-Orbit Coupling Data

Table A.3: Spin-orbit coupling terms A and B as a function of the Jacobi coordinate R for $\theta = 0^o$ and $r = 1.402$ a.u.

R/ a.u.	A/ cm^{-1}	B/ cm^{-1}
20.00	76.79	76.79
18.00	76.79	76.79
16.00	76.79	76.79
14.00	76.79	76.79
12.00	76.79	76.79
10.00	76.79	76.80
9.50	76.79	76.80
9.00	76.79	76.80
8.25	76.79	76.80
7.50	76.78	76.80
6.75	76.78	76.80
6.00	76.78	76.79
5.35	76.76	76.76
5.00	76.74	76.73
4.91	76.72	76.71
4.85	76.72	76.70
4.79	76.71	76.69
4.73	76.69	76.68
4.65	76.68	76.65
4.50	76.62	76.61
4.25	76.48	76.50
4.00	76.18	76.32
3.75	75.58	76.04
3.50	74.39	75.58
3.25	72.05	74.81
3.00	67.90	73.64

Table A.4: Spin-orbit coupling terms A and B as a function of the Jacobi coordinate r for $\theta = 0.0^o$ and $r = 3.0$ a.u.

r/ a.u.	A / cm^{-1}	B / cm^{-1}
1.050	73.48	74.68
1.200	71.63	74.33
1.300	69.98	74.02
1.402	67.90	73.64
1.500	65.45	73.19
1.722	58.42	71.99
1.888	52.30	71.08
2.300	37.97	69.54

Appendix B
The Theory of the Free OH/OD Diatomic Molecule

The electronic configuration of the ground state of OH molecule is $1\sigma^2 2\sigma^2 3\sigma^2 2\pi^3$. In the united atom limit, OH is identical to the open-shell fluorine atom, ^2P. The ground electronic state of OH is designated by the molecular term symbol $^2\Pi$.

The nonrelativistic Hamiltonian for the diatomic molecule, after the separation of the center-of-mass motion, is

$$\mathbf{H} = \mathbf{T}_n(r, \theta, \phi) + \mathbf{T}_e(\vec{q}) + \mathbf{V}(\vec{q}, r). \tag{B.1}$$

Here, $\mathbf{T}_n(r, \theta, \phi)$ is the kinetic energy of the nuclei, and the angles θ and ϕ specify the orientation of the internuclear axis with respect to the laboratory frame of reference as illustrated in Fig. B.1. The kinetic energy of the electrons are represented by $\mathbf{T}_e(\vec{q})$, and $\mathbf{V}(\vec{q}, r)$ is the electrostatic potential energy including *electron-electron*, *nuclei-nuclei* and *electron-nuclei* interactions. Then, within the Born-Oppenheimer approximation, as explained earlier in chapter 1.1, assuming that the electronic and

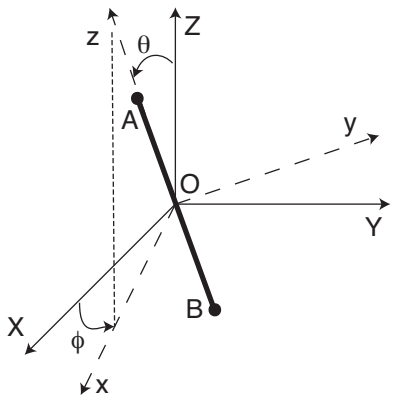

Figure B.1: Relationships between the molecule-fixed (xyz) and space-fixed (XYZ) axis systems.

nuclear motions are separable, we can obtain the electronic part of the wavefunction by solving the Schrodinger equation

$$\mathbf{H}_{el}\Phi_{el}(\vec{q};r) = \epsilon_{el}\Phi_{el}(\vec{q};r), \tag{B.2}$$

where

$$\begin{aligned}\mathbf{H}_{el} &= \mathbf{T}_e(\vec{q}) + \mathbf{V}(\vec{q},r) \\ &= -\frac{1}{2}\sum_{i=1}^{n}\nabla^2_{\vec{q}_i} - \sum_{i=1}^{n}\sum_{A=1}^{2}\frac{Z_A}{q_{iA}} + \sum_{i}^{n}\sum_{j<i}^{n}\frac{1}{q_{ij}}.\end{aligned} \tag{B.3}$$

The electronic wavefunction, Φ_{el}, for an open-shell system is designated not only by its energy eigenvalues but also by the values of the electronic spin and orbital angular momenta. If we neglect the spin of the nuclei, then we have in addition the nuclear rotational angular momentum $\mathbf{R}$, and the total angular momentum, $\mathbf{j} = \mathbf{l} + \mathbf{s} + \mathbf{R}$. In order to label the electronic levels, one needs to treat carefully the couplings among these angular momenta.

Since a diatomic molecule has only cylindrical, not spherical symmetry, only the projection, λ, of the orbital angular momentum around the bond axis is a good

quantum number. The spin angular momentum, **s**, can also be quantized along the internuclear axis. The spin projection quantum number is called σ. In this choice of quantization, called Hund's case (a), spin-orbit splitting is assumed large compared to the rotational energy level splittings.

Since, in the case (a) basis, the electronic wave functions correspond to those we would obtain in an *ab initio* calculation, we prefer this coupling case. The Hund's case (a) electronic function, Φ_{el}, is labeled as

$$|ns\lambda\sigma> . \tag{B.4}$$

Here n is the label for the electronic state.

In case (a), the projection of total angular momentum onto the internuclear axis is $\omega = \lambda + \sigma$. (Note that the rotational angular momentum, **R** is perpendicular to this axis, so its projection is null.) This quantum number, ω takes on the values:

$$|\omega| = |\lambda| - |\sigma|, \cdots, |\lambda| + |\sigma| \tag{B.5}$$

For OH, in a $^2\Pi$ electronic state, $\lambda = \pm 1$ and $\sigma = \pm\frac{1}{2}$, and so $\omega = \pm\frac{3}{3}, \pm\frac{1}{2}$. The molecular term symbol for the ground state of OH is $^2\Pi_{\frac{3}{2}}$, (the standard nomenclature: $^{2S+1}\lambda_\omega$) since OH has a more than half-filled shell. (Remember that for atoms with a more than a half-filled shell, the level with the highest value of j lies lowest in energy. [171])

If the differences between the rotational levels are larger than the splitting due to spin-orbit coupling, (which occurs as **R** increases) then the spin is decoupled from the internuclear axis and coupled to the rotational angular momentum, **R** to form a resultant angular momentum called **N**. This second coupling scheme is called

Hund's case (b). [121]. In reality, OH is described as an intermediate coupling case between (a) and (b). [172]

Equation (B.2) is solved in the basis of B.4 and nuclear repulsion is added to obtain the potential energy for the motion of the nuclei

$$v(r) = \epsilon_{el}(r) + V_{nn}(r). \tag{B.6}$$

Thus, the diatomic Hamiltonian is reduced into:

$$\mathbf{H} = \mathbf{T}_n(r, \theta, \phi) + v(r) \tag{B.7}$$

The angular part of the kinetic energy can be separated as

$$\mathbf{T}_n(r, \theta, \phi) = -\frac{\hbar^2}{2\mu_{\mathrm{OH}} r} \frac{\partial^2}{\partial r^2} r + \frac{\mathbf{R}^2}{2\mu_{\mathrm{OH}} r^2}. \tag{B.8}$$

where μ_{OH} is the reduced mass of the molecule. Thus the Hamiltonian becomes

$$\mathbf{H} = -\frac{\hbar^2}{2\mu_{\mathrm{OH}} r} \frac{\partial^2}{\partial r^2} r + \frac{\mathbf{R}_{op}^2}{2\mu_{\mathrm{OH}} r^2} + v(r). \tag{B.9}$$

Now we need a set of basis functions with a proper description of the nuclear motion to expand the Hamiltonian. The rotational wave function is the Wigner rotation matrix element[173]:

$$|j\omega m\rangle = \left(\frac{2j+1}{4\pi}\right)^{\frac{1}{2}} D^{j*}_{m\omega}(\phi, \theta, 0), \tag{B.10}$$

where, θ and ϕ are the Euler angles and j is the total angular quantum number with projection quantum numbers m along the space-frame Z-axis and ω along the internuclear axis. The vibrational wave functions are obtained from the solution of the radial part of the Hamiltonian in Eq. (B.9) with potential energy $v(r)$.

Consequently, the total wavefunction can be expanded in the product basis with elements[173]:

$$|v\rangle|j\omega m\rangle|ns\lambda\sigma\rangle. \tag{B.11}$$

The parity operator, which defines the behavior of the wave function under the inversion of all spatial coordinates through the origin, commutes with the Hamiltonian. By convention the wave function has even parity if it does not changes sign, odd if it does. Thus we can define wave functions of definite parity as [173]

$$|n\ ^2\Pi_\omega\ vjm\epsilon\rangle = \frac{1}{\sqrt{2}}|v\rangle\left[|j\ |\omega|\ m\rangle|ns\lambda\sigma\rangle + \epsilon|j, -|\omega|\ m\rangle|ns, -|\lambda|\ , -|\sigma|\rangle\right] \tag{B.12}$$

where $\epsilon = \pm$. The parity of this wave function is

$$p = \epsilon(-1)^{j-s}. \tag{B.13}$$

To evaluate the rotational part of the kinetic energy for nuclear motion, since the rotational angular momentum is not a good quantum number in the case (a) basis, we use the relation

$$\mathbf{R} = \mathbf{j} - \mathbf{l} - \mathbf{s}, \tag{B.14}$$

so that

$$\begin{aligned}
\mathbf{H}_{rot} &= (1/2\mu R^2)\ \mathbf{R}^2 \\
&= (1/2\mu r^2)\ \left[\mathbf{j} - \mathbf{l} - \mathbf{s}\right]^2 \\
&= (1/2\mu r^2)\ \left[\mathbf{j}^2 + \mathbf{l}^2 + \mathbf{s}^2 + 2l_z s_z - 2j_z l_z - 2j_z s_z\right] \\
&\quad +(1/2\mu r^2)\ \left[(l_+ s_- + l_- s_+) - (j_- l_- + j_+ l_+) - (j_- s_- + j_+ s_+)\right].
\end{aligned} \tag{B.15}$$

Here we follow the conventions for the molecule-fixed raising and lowering operators. Note that the angular momentum operators which refer to different frames (j: space-

fixed, l and s: body-fixed) obey anomalous commutation rules, [121] in which A_+ and A_- are interchanged. Except for the $\mathbf{l}^2$ term, the first line of Eq. (B.15) is diagonal in the case (a) basis. The angular momentum l is not a good quantum number. However, the expectation value of $\mathbf{l}^2$ is only weakly dependent on r. One assumes that $\langle \mathbf{l}^2 \rangle$ will lead only to an overall shift in the electronic energy.[107] Hence, the diagonal part of the Hamiltonian in the $|n\ ^2\Pi_\omega\ vjm\epsilon\rangle$ basis would be:

$$\langle \mathbf{H}_{rot}^{diag} \rangle = \left[j(j+1) + s(s+1) + \lambda^2 + 2\lambda\sigma - 2\omega^2 \right] \langle v|(1/2\mu r^2)|v\rangle \quad \text{(B.16)}$$

$$= \left[j(j+1) + s(s+1) + \lambda^2 + 2\lambda\sigma - 2\omega^2 \right] B_v \quad \text{(B.17)}$$

Since the parity operator commutes with the Hamiltonian, the diagonal part of the Hamiltonian is independent of parity. The Hamiltonian in Eq. (B.1) is nonrelativistic. The spin-orbit contribution can then be added:

$$\mathbf{H}_{so} = A(r)\ \mathbf{l} \cdot \mathbf{s}, \quad \text{(B.18)}$$

so the total Hamiltonian becomes

$$\mathbf{H} = -\frac{\hbar^2}{2\mu_{\mathrm{OH}} r} \frac{\partial^2}{\partial r^2} r + \frac{\mathbf{R}_{op}^2}{2\mu_{\mathrm{OH}} r^2} + v(r) + \mathbf{H}_{so}. \quad \text{(B.19)}$$

The off-diagonal terms in Eq. (B.15) lead to mixings between the $\omega = 3/2$ and $\omega = 1/2$ spin orbit states as well as between the $^2\Pi$ and higher electronic states. The first term, $l_+ s_- + l_- s_+$, leads to a coupling of spin to electronic motion, in a similar manner to the spin-orbit Hamiltonian. The second term, $j_+ l_- + j_- l_+$ couples rotational motion and electronic motion; however it does not couple the various components of the $^2\Pi_\omega$ states to each other. All of these off-diagonal terms

will couple only the same parity states. The last term couples the spin to the total angular momentum. This term $(j_+s_- + j_-s_+)$ couples $^2\Pi_{1/2}$ to $^2\Pi_{3/2}$ states.

$$\left\langle n^2\Pi_{\Omega=\frac{1}{2}} vjm\epsilon \left| (1/2\mu r^2)(j_+s_- + j_-s_+) \right| n^2\Pi_{\omega=\frac{3}{2}} vjm\epsilon' \right\rangle = -\delta_{\epsilon\epsilon'} B_v \left[j(j+1) - \frac{3}{4} \right]^{\frac{1}{2}}. \tag{B.20}$$

The matrix elements are roughly linearly dependent on j, so that, as j gets higher, this term can become comparable to the magnitude of the spin-orbit coupling.

The spin-orbit Hamiltonian in Eq. (B.18)

$$\mathbf{H}_{so} = A(r)\ \mathbf{l}\cdot\mathbf{s} \quad = \quad A(r)\ [l_z s_z + \frac{1}{2}\left(l_- s_+ + l_+ s_-\right)]. \tag{B.21}$$

Only the first term leads to the coupling within the $^2\Pi$ states. Taking into account the terms that lead to coupling within the $^2\Pi$ state, the Hamiltonian is evaluated in a basis consisting of $\{\left|^2\Pi_{3/2}\right\rangle, \left|^2\Pi_{1/2}\right\rangle\}$ of a given parity:

$$\mathbf{H}_{rot} + \mathbf{H}_{so} = \begin{pmatrix} B_v\left[(j+\frac{1}{2})^2 - 2\right] + A(r)\frac{1}{2} & -B_v\left[(j+\frac{1}{2})^2 - 1\right]^{\frac{1}{2}} \\ -B_v\left[(j+\frac{1}{2})^2 - 1\right]^{\frac{1}{2}} & B_v(j+\frac{1}{2})^2 - A(r)\frac{1}{2} \end{pmatrix} \tag{B.22}$$

Diagonalization leads to the eigenvalues:

$$E_\pm \quad = \quad B_v\left[j(j+1) - \frac{3}{4} \pm \frac{1}{2}\left(4j(j+1) + \frac{(B_v - 2A)^2}{B_v^2} \right)^{\frac{1}{2}} \right], \tag{B.23}$$

$$\quad = \quad B_v\left[j(j+1) - \frac{3}{4} \pm \frac{1}{2}\sqrt{X} \right], \tag{B.24}$$

where

$$X = \sqrt{4\left(j+\frac{1}{2}\right)^2 + \frac{A}{B_v}\left(\frac{A}{B} - 4\right)}. \tag{B.25}$$

The corresponding eigenvectors are[173]

$$|F_1\rangle \quad = \quad b_j|^2\Pi_{\frac{3}{2}} vj\rangle + a_j|^2\Pi_{\frac{1}{2}} vj\rangle, \tag{B.26}$$

$$|F_2\rangle \quad = \quad a_j|^2\Pi_{\frac{3}{2}} vj\rangle - b_j|^2\Pi_{\frac{1}{2}} vj\rangle, \tag{B.27}$$

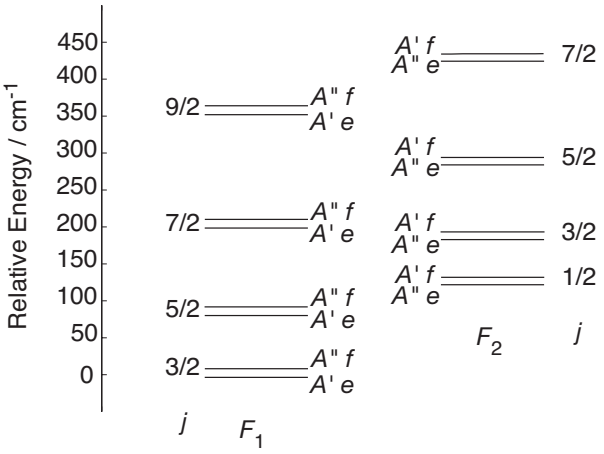

Figure B.2: Positions of the lower spin-rotation levels of OH($X^2\Pi$). For clarity, the magnitude of the Λ-doublet splitting has been greatly exaggerated in the figure.

with coefficients

$$a_j = \left[\frac{X + A/B_v - 2}{2X}\right]^{\frac{1}{2}}, \tag{B.28}$$

$$b_j = \left[\frac{X - A/B_v + 2}{2X}\right]^{\frac{1}{2}}. \tag{B.29}$$

The eigenvalues forms two rotational ladders, F_1 and F_2, (see Fig. B.2) separated by the spin-orbit coupling energy. Figure B.3 plots the change in the coupling coefficients a_j and b_j as a function of increasing total angular momentum. It reveals the intermediate coupling nature of OH. For low j's, two rotational ladders are separated by the spin-orbit coupling. In high j-limit, we can no longer assign the F_1 and F_2 levels as corresponding to separate $^2\Pi_{3/2}$ and $^2\Pi_{1/2}$ states. Each rotational level is doubly degenerate without the effect of the $(j_+l_+ + j_-l_-)$ term. It is this term which is responsible from the so called $\lambda - doubling$. It couples electronic angular momentum to the rotational motion of the nuclei, and become more important as j increases.

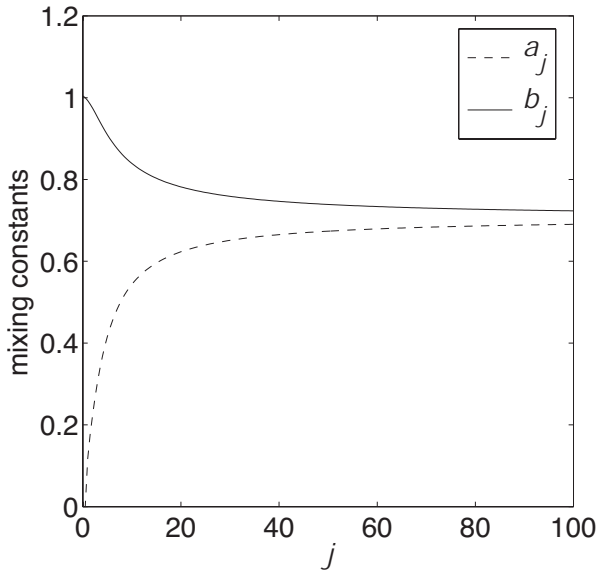

Figure B.3: Coupling coefficients a_j and b_j as a function of total angular quantum number j.

The λ-doubling Hamiltonian including the off-diagonal part of the spin-orbit and rotational coupling terms of Eq. (B.15) and (B.21), which were omitted previously, is [173]

$$H' = -B(r)(j_+ l_+ + j_- l_-) + [B(r) + A(r)/2](l_+ s_- + l_- s_+). \tag{B.30}$$

Based on the Van Vleck transformation, the λ-doubling Hamiltonian can be written in terms of two coupling constants, p_v and q_v [173]

$$p_v = 4 \sum_{n'v'} \frac{\langle {}^2\Pi_v | \frac{1}{2} A(r) L_+ | n'^2\Sigma^{\pm} v' \rangle \langle n^2\Pi v | B(r) L_+ | n'^2\Sigma^{\pm} v' \rangle}{E_{\Pi v} - E_{n'v'}}, \tag{B.31}$$

$$q_v = 2 \sum_{n'v'} \frac{|\langle {}^2\Pi_v | B(r) L_+ | n'^2\Sigma^{\pm} v' \rangle|^2}{E_{\Pi v} - E_{n'v'}}. \tag{B.32}$$

After the addition of the λ-doubling Hamiltonian, the matrix elements of H_{mol} can be written in terms of several spectroscopic constants as [174]:

$$\langle \omega = \frac{1}{2}\varepsilon \, | H_{mol} | \, \omega = \frac{1}{2}\varepsilon \rangle \quad = \quad E_v - A_v/2 + (j + 1/2)^2 B_v$$

Table B.1: Pertinent spectroscopic constants (cm^{-1}) for OH and OD.

	OH	OD
p_v	$0.235 - 0.006v$ [a]	$0.1266 - 0.005v$ [b]
q_v	$-0.0391 + 0.0018v$ [a]	$-0.01093 + 0.0004v$ [b]
A_v	$-139.21 - 0.275v$ [a]	$-139.23 - 0.205v$ [b]
B_v	$18.910 - 0.7242(v+1/2)^a$	$10.0209 - 0.2757(v+1/2)^a$

[a] Ref. [112]

[b] Linear fit in the vibrational quantum number of the data from Ref. [175] for $v \leq 2$.

$$
\begin{aligned}
& & & + \left[1 - \varepsilon\left(j+1/2\right)\right] p_v/2 + \left[1 - \varepsilon(j+1/2)\right]^2 q_v/2 \\
\langle \omega = \frac{1}{2}\varepsilon \left| H_{mol} \right| \omega = \frac{3}{2}\varepsilon \rangle & = & & -\frac{1}{4}\left[(j+1/2)^2 - 1\right]^{1/2} \\
& & & \{4B_v + p_v + 2\left[1 - \varepsilon(j+1/2)\right] q_v\} \\
\langle \omega = \frac{3}{2}\varepsilon \left| H_{mol} \right| \omega = \frac{3}{2}\varepsilon \rangle & = & & E_v + A_v/2 + [(j+1/2)^2 - 2] B_v \\
& & & + \left[(j+1/2)^2 - 1\right] q_v/2. \qquad \text{(B.33)}
\end{aligned}
$$

If we compare the above matrix elements with the matrix elements in Eq. (B.22), we see that the λ-doubling Hamiltonian slightly splits each rotational level depending on the parity. The pertinent spectroscopic constants for OH and OD are given in Table B.1. They are very small in magnitude. However, as will be discussed in Chapters 4 and 5, investigating the λ-doublet occupations of products is useful to derive information about the dynamics of the reaction.

BIBLIOGRAPHY

[1] P. W. Atkins, *Physical Chemistry* (Oxford University Press, Oxford, UK, 1994), 5th ed.

[2] A. A. Westenberg and N. J. deHaas, J. Chem. Phys. **47**, 4241 (1967).

[3] A. A. Westenberg and N. J. deHaas, J. Chem. Phys. **50**, 2512 (1969).

[4] R. N. Dubinsky and D. J. McKenny, Can. J. Chem. **63**, 3531 (1975).

[5] G. Dixon-Lewis and D. J. Williams, Comput. Chem. Kinet. **17**, 1 (1977).

[6] S. P. Walch, A. F. Wagner, T. H. J. Dunning, and G. C. Schatz, J. Chem. Phys. **72**, 2894 (1980).

[7] G. C. Schatz, A. F. Wagner, S. P. Walch, and J. M. Bowman, J. Chem. Phys. **74**, 4984 (1981).

[8] K. T. Lee, J. M. Bowman, A. F. Wagner, and G. C. Schatz, J. Chem. Phys. **76**, 3563 (1982).

[9] B. C. Garrett, D. G. Truhlar, J. M. Bowman, and A. F. Wagner, J. Phys. Chem. **90**, 4305 (1986).

[10] D. Baulch, C. Cobos, R. Cox, C. Esser, P. Frank, T. Just, J. Kerr, M. Pilling, J. Troe, R. Walker, and J. Warnatz, J. Phys. Chem. Ref. Data **21**, 411 (1992).

[11] H.-X. Yang, K. S. Shin, and W. Gardiner, Chem. Phys. Lett. **207**, 69 (1993).

[12] S. Javoy, V. Naudet, S. Abid, and C. E. Paillard, Exp. Therm. Fluid Sci. **27**, 371 (2003).

[13] D. C. Chatfield, S. F. Ronald, G. C. Lynch, D. G. Truhlar, and D. W. Schwenke, J. Chem. Phys. **98**, 342 (1993).

[14] B. R. Johnson and N. W. Winter, J. Chem. Phys. **66**, 4116 (1977).

[15] R. E. Howard, A. D. McLean, and W. A. J. Lester, J. Chem. Phys. **71**, 2412 (1979).

[16] R. Jaquet and V. Staemmler, Chem. Phys. **59**, 373 (1981).

[17] A. F. Wagner, G. C. Schatz, and J. M. Bowman, J. Chem. Phys. **74**, 4960 (1981).

[18] V. Aquilanti, S. Cavalli, V. Pelizzari, M. Rosi, A. Sgamellotti, and F. Tarantelli, Chem. Phys. Lett. **162**, 179 (1989).

[19] K. A. Peterson and T. H. J. Dunning, J. Phys. Chem. **101**, 6280 (1997).

[20] S. Rogers, D. Wang, A. Kuppermann, and S. Walch, J. Phys. Chem. **104**, 2308 (2000).

[21] J. Brandão, C. Mogo, and B. C. Silva, J. Chem. Phys. **121**, 8861 (2004).

[22] Z. Li, V. A. Apkarian, and L. B. Harding, J. Chem. Phys. **106**, 942 (1997).

[23] M. H. Alexander, J. Chem. Phys. **108**, 4467 (1998).

[24] D. J. Donaldson and J. S. Wright, J. Chem. Phys. **80**, 221 (1984).

[25] M. R. Hoffmann and G. C. Schatz, J. Chem. Phys. **113**, 9456 (2000).

[26] D. J. Garton, T. K. Minton, M. Biswajit, D. Troya, and G. C. Schatz, J. Chem. Phys. **118**, 1585 (2003).

[27] M. Braunstein, S. Adler-Golden, B. Maiti, and G. C. Schatz, J. Chem. Phys. **120**, 4316 (2004).

[28] N. Balakrishnan, J. Chem. Phys. **119**, 195 (2003).

[29] R. A. Sultanov and N. Balakrishnan, J. Chem. Phys. **121**, 11038 (2004).

[30] N. Balakrishnan, J. Chem. Phys. **121**, 6346 (2004).

[31] V. Aquilanti, R. Candori, L. Mariani, F. Pirani, and G. Liuti, J. Phys. Chem. **93**, 130 (1989).

[32] B. Maiti and G. C. Schatz, J. Chem. Phys. **119**, 12360 (2003).

[33] T.-S. Chu, X. Zhang, and K.-L. Han, J. Chem. Phys. **122**, 214301 (2005).

[34] K. Croswell and A. Dalgarno, Astrophys. J. **289**, 618 (1985).

[35] M. M. Litvak, Science **165**, 855 (1969).

[36] W. D. Gwinn, B. E. Turner, W. M. Goss, and G. L. Blackman, Astrophys. J. **179**, 789 (1973).

[37] M. Bertojo, A. C. Cheung, and C. H. Townes, Astrophys. J. **208**, 914 (1976).

[38] P. W. Andresen, Astron. Astrophys. **154**, 42 (1986).

[39] M. Born and J. R. Oppenheimer, Ann. Physik **84**, 457 (1927).

[40] A. Szabo and N. S. Ostlund, *Modern Quantum Chemistry* (Dover Publications, Inc., New York, 1989), 2nd ed.

[41] R. T. Pack and J. O. Hirschfelder, J. Chem. Phys. **49**, 4009 (1968).

[42] H.-J. Werner, P. J. Knowles, R. Lindh, M. Schütz, P. Celani, T. Korona, F. R. Manby, G. Rauhut, R. D. Amos, A. Bernhardsson, A. Berning, D. L. Cooper, M. J. O. Deegan, A. J. Dobbyn, F. Eckert, C. Hampel, G. Hetzer, A. W. Lloyd, S. J. McNicholas, W. Meyer, M. E. Mura, A. Nicklass, P. Palmieri, R. Pitzer, U. Schumann, H. Stoll, A. J. Stone, R. Tarroni, and T. Thorsteinsson, *Molpro, version 2002.6, a package of ab initio programs* (2003), see http://www.molpro.net.

[43] P. G. Mezey, *Potential Energy Hypersurfaces*, Studies in physical and theoretical chemistry (Elsevier Science Publishing Company Inc., New York, 1987).

[44] J. N. Murrell, S. Carter, S. C. Farantos, P. Huxley, and A. J. C. Varandas, *Molecular Potential Energy Functions* (Wiley, Chichester, 1984).

[45] J. Z. H. Zhang, *Theory and Application of Quantum Molecular Dynamics* (World Scientific, New York, 1999).

[46] R. D. Levine and R. B. Bernstein, *Molecular Reaction Dynamics and Chemical Reactivity* (Oxford, Oxford, 1987), 2nd ed.

[47] J. D. Lambert, *Vibrational and Rotational Relaxation In Gases* (Clarendon Press, Oxford, 1977).

[48] H. K. Shin, in *Dynamics of Molecular Collisions, Part A*, edited by W. Miller (Plenum, New York, 1976), p. 1.

[49] P. Ehrenfest, Koninkl. Ned. Akad. Wetenschap. Proc. **16**, 591 (1914).

[50] K. H. R. N. Schwartz, Z. I. Slawsky, J. Chem. Phys. **20**, 1591 (1952).

[51] H. K. Shin, J. Am. Chem. Soc. **90**, 3025 (1968).

[52] H. K. Shin, J. Am. Chem. Soc. **90**, 3030 (1968).

[53] I. W. M. Smith, J. Chem. Soc.-Faraday Trans. **93**, 3741 (1997).

[54] I. W. M. Smith, Abstr. Pap. Am. Chem. Soc. **188**, 17 (1984).

[55] P. W. Barnes, P. Sharkey, I. R. Sims, and I. W. M. Smith, Faraday Discuss. **113**, 167 (1999).

[56] M. M. Graff and A. Dalgarno, Astrophys. J. **317**, 432 (1987).

[57] M. J. McEwan, *Chemistry of the Atmosphere* (Halsted Press, New York, 1975), 1st ed.

[58] G. C. Schatz, J. Chem. Phys. **83**, 5677 (1985).

[59] J. M. Bowman and A. F. Wagner, J. Chem. Phys. **84**, 1967 (1987).

[60] A. F. Wagner and J. M. Bowman, J. Chem. Phys. **86**, 1976 (1987).

[61] M. Nakamura, J. Chem. Phys. **96**, 2724 (1992).

[62] J. Han, X. Chen, and B. R. Weiner, Chem. Phys. Lett. **332**, 243 (2000).

[63] R. Schinke and W. A. J. Lester, J. Chem. Phys. **70**, 4893 (1979).

[64] R. A. Gangi and R. F. W. Bader, J. Chem. Phys. **55**, 5369 (1971).

[65] P. A. Whitlock, J. T. Muckerman, and E. P. Fisher, Tech. Rep., Research Institute for Engineering Sciences, Wayne State University, Detroit, 1976 (1976).

[66] S. P. Walch, T. H. J. Dunning, F. W. Bobrowicz, and R. C. Raffenetti, J. Chem. Phys. **72**, 406 (1980).

[67] P. F. Weck and N. Balakrishnan, J. Chem. Phys. **123**, art. no. 144308 (2005).

[68] M. H. Alexander, D. E. Manolopoulos, and H. J. Werner, J. Chem. Phys. **113**, 11084 (2000).

[69] B. Pullman, ed., *Intermolecular Interactions: From Diatomics to Biopolymers* (John Wiley and Sons, New York, 1978), first edition ed.

[70] D. Skouteris, D. E. Manolopoulos, W. Bian, H.-J. Werner, L.-H. Lai, and K. Liu, Science **286**, 1713 (1999).

[71] P. J. Knowles, C. Hampel, and H.-J. Werner, J. Chem. Phys. **99**, 5219 (1993).

[72] M. Deegan and P. J. Knowles, Chem. Phys. Lett. **227**, 321 (1994).

[73] J. Klos, G. Chalasinski, M. M. Szczesniak, and H.-J. Werner, J. Chem. Phys. **115**, 3085 (2001).

[74] S. F. Boys and F. Bernardi, Mol. Phys. **19**, 553 (1970).

[75] F.-M. Tao and Y.-K. Pan, J. Chem. Phys. **97**, 4989 (1992).

[76] T. H. J. Dunning, J. Chem. Phys. **90**, 1007 (1989).

[77] R. A. Kendall, T. H. J. Dunning, and R. J. Harrison, J. Chem. Phys. **96**, 6796 (1992).

[78] E. R. Davidson and D. W. Silver, Chem. Phys. Lett. **53**, 403 (1977).

[79] E. R. Davidson and D. W. Silver, Chem. Phys. Lett. **52**, 403 (1978).

[80] K. Stark and H.-J. Werner, J. Chem. Phys. **104**, 6515 (1996).

[81] M.-L. Dubernet and J. M. Hutson, J. Chem. Phys. **101**, 1939 (1994).

[82] H.-J. Werner and W. Meyer, J. Chem. Phys. **74**, 5802 (1981).

[83] H.-J. Werner, B. Follmeg, and M. H. Alexander, J. Chem. Phys. **89**, 3139 (1988).

[84] H. A. Bethe and E. E. Salpeter, *Quantum Mechanics of One- and Two-Electron Atoms* (Springer-Verlag, Berlin, 1957).

[85] A. Berning, M. Schweizer, H.-J. Werner, P. J. Knowles, and P. Palmieri, Mol. Phys. **98**, 1823 (2000).

[86] A. Nicklass, K. A. Peterson, A. Berning, H.-J. Werner, and P. J. Knowles, J. Chem. Phys. **112**, 5624 (2000).

[87] C. E. Moore, *Atomic Energy Levels As Derived From the Analysis of Optical Spectra*, vol. 1 (National Bureau of Standards, Washington, D. C., 1971), second edition ed.

[88] A. J. Dobbyn and P. J. Knowles, Mol. Phys. **91**, 1107 (1997).

[89] E. J. Rackham, F. Huarte-Larrañaga, and D. E. Manolopoulos, Chem. Phys. Lett. **343**, 356 (2001).

[90] E. J. Rackham, T. Gonzalez-Lezaña, and D. E. Manolopoulos, J. Chem. Phys. **119**, 12895 (2003).

[91] S. Y. Lin and H. Guo, J. Chem. Phys. **120**, 9907 (2004).

[92] S. Y. Lin and H. Guo, J. Phys. Chem. A **108**, 10066 (2004).

[93] P. Honvault and J.-M. Launay, J. Chem. Phys. **114**, 1057 (2001).

[94] M. H. Alexander, E. J. Rackham, and D. E. Manolopoulos, J. Chem. Phys. **121**, 5221 (2004).

[95] P. Pechukas and J. C. Light, J. Chem. Phys. **42**, 3281 (1965).

[96] D. C. Clary and J. P. Henshaw, Faraday Disc. Chem. Soc. **84**, 333 (1987).

[97] P. McGuire and D. J. Kouri, J. Chem. Phys. **60**, 2488 (1974).

[98] R. T. Pack, J. Chem. Phys. **60**, 633 (1974).

[99] P. Pechukas, in *Dynamics of Molecular Collisions, Part B*, edited by W. Miller (Plenum, New York, 1976), p. 269.

[100] P. Pechukas, J. C. Light, and C. Rankin, J. Chem. Phys. **44**, 794 (1966).

[101] D. Secrest, in *Atom-Molecule Collision Theory: A Guide for the Experimentalist*, edited by R. Bernstein (Plenum, New York, 1979), p. 265.

[102] D. C. Manolopoulos, J. Chem. Phys. **85**, 6425 (1986).

[103] M. H. Alexander and D. E. Manolopoulos, J. Chem. Phys. **86**, 2044 (1987).

[104] E. J. Rackham, D. phil., Jesus College, University of Oxford (2004).

[105] H.-J. Werner and P. J. Knowles, J. Chem. Phys. **89**, 5803 (1988).

[106] P. J. Knowles and H.-J. Werner, Chem. Phys. Lett. **145**, 514 (1988).

[107] H. Lefebvre-Brion and R. Field, *Perturbations in the Spectra of Diatomic Molecules* (Academic, New York, 1986).

[108] M. H. Alexander, P. Andresen, R. Bacis, R. Bersohn, F. J. Comes, P. J. Dagdigian, R. N. Dixon, R. W. Field, G. W. Flynn, K.-H. Gericke, E. R. Grant, B. J. Howard, J. R. Huber, D. S. King, J. L. Kinsey, K. Kleinermanns, K. Kuchitsu, A. C. Luntz, A. J. MacCaffery, B. Pouilly, H. Reisler, S. Rosenwaks, E. Rothe, M. Shapiro, J. P. Simons, R. Vasudev, J. R. Wiesenfeld, C. Wittig, and R. N. Zare, J. Chem. Phys. **89**, 1749 (1988).

[109] E. E. Nikitin and R. N. Zare, Mol. Phys. **82**, 85 (1994).

[110] B. R. Johnson, J. Comp. Phys. **13**, 445 (1973).

[111] S. D. Rodgers and S. B. Charnley, Planet Space Sci. **50**, 1125 (2002).

[112] K. P. Huber and G. Herzberg, *Molecular Spectra and Molecular Structure. IV. Constants of Diatomic Molecules* (Van Nostrand Reinhold, New York, 1979).

[113] F. J. Aoiz, L. Bañares, J. F. Castillo, M. Brouard, W. Denzer, C. Vallance, P. Honvault, J.-M. Launay, A. J. Dobbyn, and P. J. Knowles, Phys. Rev. Lett. **86**, 1729 (2001).

[114] M. J. Howard and I. W. M. Smith, J. Chem. Soc., Faraday. Trans. II. **78**, 1403 (1982).

[115] L. J. Dunne and J. N. Murrell, Mol. Phys. **50**, 635 (1983).

[116] J. J. Margitan, F. Kaufman, and J. G. Anderson, Chem. Phys. Lett. **34**, 485 (1975).

[117] J. Troe, J. Chem. Phys. **66**, 4745 (1977).

[118] M. Quack and J. Troe, Ber. Bunsen. Phys. Chem. **81**, 329 (1977).

[119] P. Day and D. Truhlar, J. Chem. Phys. **95**, 5097 (1991).

[120] D. C. Clary, Mol. Phys. **53**, 3 (1984).

[121] R. D. Levine and R. B. Bernstein, *Molecular Reaction Dynamics* (Oxford, Oxford, 1974), 1st ed.

[122] J. N. Murrell, S. Carter, I. M. Mills, and M. F. Guest, Mol. Phys. **42**, 605 (1981).

[123] R. N. Porter and L. M. Raff, in *Dynamics of Molecular Collisions, Part B*, edited by W. Miller (Plenum, New York, 1976), p. 1.

[124] J. E. Butler, G. M. Jursich, I. A. Watson, and J. R. Wiesenfeld, J. Chem. Phys. **84**, 5365 (1986).

[125] K. Mikulecky and K.-H. Gericke, J. Chem. Phys. **96**, 7490 (1992).

[126] D. C. Clary and H.-J. Werner, Chem. Phys. Lett. **112**, 346 (1984).

[127] I. W. M. Smith, *Kinetics and dynamics of elementary gas reactions* (Butterworths, London, 1980).

[128] T. J. Sears, G. E. Hall, and J. J. F. McAndrew, J. Chem. Phys. **91**, 5201 (1989).

[129] K. Menten (2005), private communication.

[130] J. W. Meriwether, J. Geophys. Res. **94**, 14629 (1989).

[131] H. Berresheim, C. Plass-Dulmer, T. Elste, N. Mihalopoulos, and F. Rohrer, Atmos. Chem. Phys. **3**, 639 (2003).

[132] J. A. Dodd, S. J. Lipson, J. R. Lowell, P. S. Armstrong, W. A. M. Blumberg, R. M. Nadile, S. M. Adler-Golden, W. J. Marinelli, K. W. Holtzclaw, and B. D. Green, J. Geophys. Res.-Atmos. **99**, 3559 (1994).

[133] B. R. Chalamala and R. A. Copeland, J. Chem. Phys. **99**, 5807 (1993).

[134] A. D. Sappey and R. A. Copeland, J. Chem. Phys. **93**, 5741 (1990).

[135] G. P. Glass, H. Endo, and B. K. Chaturvedi, J. Chem. Phys. **77**, 5450 (1982).

[136] I. W. M. Smith and M. D. Williams, J. Chem. Soc. Faraday. Trans. 2. **81**, 1849 (1985).

[137] J. Brunning, D. W. Derbyshire, I. W. M. Smith, and M. D. Williams, J. Chem. Soc. Faraday. Trans. 2. **84**, 105 (1988).

[138] K. J. Rensberger, J. B. Jeffries, and D. R. Crosley, J. Chem. Phys. **90**, 2174 (1989).

[139] J. A. Dodd, S. J. Lipson, and W. A. M. Blumberg, J. Chem. Phys. **95**, 5752 (1991).

[140] K. Knutsen, M. J. Dyer, and R. A. Copeland, J. Chem. Phys. **104**, 5798 (1996).

[141] M. J. Dyer, K. Knutsen, and R. A. Copeland, J. Chem. Phys. **107**, 7809 (1997).

[142] K. W. Holtzclaw, B. L. Upschulte, G. E. Caledonia, J. F. Cronin, B. D. Green, S. J. Lipson, W. A. M. Blumberg, and J. A. Dodd, J. Geophys. Res-Space Phys. **102**, 4521 (1997).

[143] J. Lacoursiere, M. J. Dyer, and R. A. Copeland, J. Chem. Phys. **118**, 1661 (2003).

[144] J. E. Spencer and G. P. Glass, Chem. Phys. **15**, 35 (1976).

[145] M. Quack and J. Troe, Ber. Bunsen. Phys. Chem. **81**, 160 (1977).

[146] M. Quack and J. Troe, Ber. Bunsen. Phys. Chem. **79**, 170 (1975).

[147] M. Quack and J. Troe, in *Encyclopedia of Computational Chemistry*, edited by P. von Rague Schleyer, N. Allinger, T. Clark, J. Gasteiger, P. A. Kollmann, and H. F. Schaefer (Wiley, New York, 1998), vol. 4, pp. 2708 – 2726.

[148] E. E. Nikitin and S. Y. Umanski, Faraday Disc. Chem. Soc. **53**, 7 (1972).

[149] M. H. Alexander, Chem. Phys. **92**, 337 (1985).

[150] K. Pavlakis and N. Kylafis, Astrophys. J. **467**, 300 (1996).

[151] A. L. Argon, M. J. Reid, and K. M. Menten, Astrophys. J. Suppl. S. **129**, 159 (2000).

[152] M. Wardle and F. Yusef-Zadeh, Science **296**, 2350 (2002).

[153] G. C. Dousmanis and T. M. Sanders, Phys. Rev. **100**, 1735 (1955).

[154] J. M. Brown, J. T. Hougen, K.-P. Huber, J. W. C. Johns, I. Kopp, H. Lefebvre-Brion, A. J. Merer, D. A. Ramsay, J. Rostas, and R. N. Zare, J. Mol. Spectrosc. **55**, 500 (1975).

[155] G. C. Corey and M. H. Alexander, J. Chem. Phys. **88**, 6931 (1988).

[156] D. Dewangan and D. Flower, J. Phys. B.: At. Mol. Phys **14**, L425 (1981).

[157] R. Schinke and P. Andresen, J. Chem. Phys. **81**, 5644 (1984).

[158] S. M. Miller, D. C. Clary, A. Kliesch, and H.-J. Werner, Mol. Phys. **83**, 405 (1994).

[159] A. R. Offer, M. C. van Hemert, and E. F. van Dishoeck, J. Chem. Phys. **100**, 362 (1994).

[160] K. Schreel and J. J. ter Meulen, J. Chem. Phys. **105**, 4522 (1996).

[161] M. Shapiro and H. Kaplan, J. Chem. Phys. **71**, 2182 (1979).

[162] R. V. Krems and S. Nordholm, J. Chem. Phys. **115**, 10581 (2001).

[163] N. M. R. V. Krems, A. A. Buchachenko and S. Nordholm, J. Chem. Phys. **117**, 166 (2002).

[164] S. Atahan, M. H. Alexander, and D. E. Rackham, J. Chem. Phys. **123**, art. no. 204306 (2005).

[165] P. J. Dagdigian, M. H. Alexander, and K. Liu, J. Chem. Phys. **91**, 839 (1989).

[166] M. H. Alexander and P. J. Dagdigian, J. Chem. Phys. **101**, 7468 (1994).

[167] P. J. Dagdigian, Annu. Rev. Phys. Chem. **48**, 123 (1997).

[168] P. Andresen, D. Häusler, H. Lülf, and W. Kegel, Astron. Astrophys. **138**, L17 (1984).

[169] D. Neufeld and A. Dalgarno, Astrophys. J. **340**, 869 (1989).

[170] J. Klos, G. Chalasinski, and M. M. Szczesniak, Int. J. Quant. Chem. **90**, 1038 (2002).

[171] G. Herzberg, *Atomic Spectra and Atomic Structure* (Dover, New York, 1944), 2nd ed.

[172] D. Dewangan and D. Flower, J. Phys. B.: At. Mol. Phys **16**, 2157 (1983).

[173] R. N. Zare, *Angular Momentum* (Wiley, New York, 1988).

[174] A. J. Kotlar, R. W. Field, J. I. Steinfeld, and J. A. Coxon, J. Mol. Spectrosc. **80**, 86 (1980).

[175] J. A. Coxon and R. E. Hammersley, J. Mol. Spectrosc. **58**, 29 (1975).